Spring 2022

An Abundance of Quenching: Comparing Observations and Simulations of Low Mass Galaxies

Claire Dickey
Yale University Graduate School of Arts and Sciences, claire.mackay.dickey@gmail.com

ABSTRACT

An Abundance of Quenching:
Comparing Observations and Simulations of Low Mass Galaxies

Claire Mackay Dickey

2022

This thesis focuses on low mass, quiescent galaxies in the local universe, with the goal of providing meaningful constraints on the feedback mechanisms that drive quenching in low mass galaxies. We present an in-depth exploration of what may be the lowest mass galaxies still able to self-quench on galaxy-wide scales, using Keck/ESI long-slit spectroscopy. Despite their overall passive appearances, nearly all low-mass quiescent galaxies host AGN, in contrast to denser environments, where we observe significant numbers of quiescent galaxies lacking AGN signatures. These results suggest that the presence of hard ionizing radiation (AGN-like line ratios) is tied to the quenching of what may be the lowest-mass self-quenched galaxies. Complementary to these findings, this thesis also explores the quiescent fraction of low mass galaxies in isolation produced by large volume (L $\geq$ 100 Mpc) comsological and hydrodynamical simulations and how they compare to wide-field galaxy surveys. To make these comparisons meaningful, we create synthetic spectroscopic and photometric observations that replicate the characteristics of a particular galaxy survey, including noise and incompleteness. All the simulations included in the study fail to reproduce the observed absence of quiescent field galaxies below $M_* = 10^9 M_\odot$, suggesting that additional or alternate feedback mechanisms are required to quench low mass, isolated galaxies. This thesis also explores the simulated low mass galaxy population in Local Group-like environments. By producing synthetic observations, we show that the simulations produce a population of faint, red satellites that have extremely old ages and represent either a population that has thus far been missed by observations or artifacts of unphysical processes in the simulations. This thesis

demonstrates on the necessity of “apples to apples” comparisons as the basis of any meaningful measurement. By acknowledging and actively folding in observational biases to analyses of galaxy simulations, we highlight the significant discrepancy between current models of low mass galaxy quenching and observations of the galaxies themselves.

An Abundance of Quenching:

Comparing Observations and Simulations of Low Mass Galaxies

A Dissertation
Presented to the Faculty of the Graduate School
of
Yale University
in Candidacy for the Degree of
Doctor of Philosophy

By
Claire Mackay Dickey

Dissertation Director: Prof. Marla Geha

May 2022

For Alfred Kwok, who taught me quantum mechanics, thermodynamics, and how best to pack a watermelon for a fourteen mile hike. The universe is less joyfully, unpredictably weird without you in it.

This thesis was written in the lands stewarded by the Quinnipiac, Paugussett, and Wappinger tribes for generations. It is built upon data taken with the Keck telescopes, which are themselves built on unceded and sacred Kanaka ʻŌiwi ancestral land.

With thanks and love

What follows in this thesis is the product of the love and support of so many people, who have shepherded it and me through so much.

That this body of works exists at all is because of my advisor, Marla Geha. It's an old joke that students inevitably turn into their advisors over the course of their PhDs — if in the future I can be half as thoughtful a mentor and half as a fierce an advocate for those in need of support, I will consider these last five years a rousing success. This thesis grew into something neither of us ever anticipated at the outset. I never would have felt comfortable working on simulations or publishing code without your constant, steady belief in my abilities. And thank you for trusting me to be a small part of the Warrior Scholar Project, which has enriched my world in countless ways.

I am so grateful to the Astronomy department community in all its many forms. Kim, Teena, Susan, Craig — you made sure that I stayed enrolled, was able to get reimbursed for travel, had an office, could observe remotely, and so much more. Thank you so much for keeping an eye all the wayward graduate students, year after year. This thesis also owes a great deal to my qualifying committee - Frank, Nikhil, and Pieter - whose invaluable feedback in those early days helped all my scattered ideas coalesce into a coherent whole. Thank you so much to the graduate students and postdocs who have been friends and mentors throughout this journey.

Every PhD is guaranteed to have its rough patches, but I never imagined that one of mine would take the form of a spectacularly shattered jaw. I am forever grateful to Dr Lowlicht and Dr Alexander, who ensured that something I once thought

would forever dominate my life is now just a good (if gruesome) story. Universal healthcare is a human right.

I've been living in New Haven for nearly seven years, the longest I have ever spent in one place. This thesis was written in countless places around the city, in its parks and coffee shops and bars. Thank you to Dave at ERC, Dave at Fussy, and Dave at Ordinary for the three meals I'll miss the most when I'm gone. Thank you to Gabi, Kayla, and Crystal, always ready with a supportive word and tea or a beer when I needed them most.

To the CLAW house - Lucas, Allen, William, Ryan - I cannot imagine having made it through all of this without you. First year will forever be distilled in my memory to problem sets around the Bishop St table and late summer nights at the firepit. Stardew Crew, you have been such a solace during this last brutal year and I cannot wait to see you all finish your own PhDs and go on to do amazing things. Lily, thank you for being my one and only writing partner and shoulder to lean on. Kaitlyn, Kim, Phil, Elise, Caroline, Erin — I don't think my teenage self could have conceived of the joy I'd feel in still being known and loved by the same group of people fifteen years down the line. I am always counting down the days until we are together again.

To my grandmother Page, thank you so much for opening your home to me and all my friends these past few summers. Church House has been such a place of respite for us all. And thank you for teaching me about the strength of growing things.

Last but never, ever least, thank you to my parents, Keith and Ali. I grew up surrounded by your love, I grew curious with your stories and questions, I grew brave with your belief in who I could become. Dad, thank you for opening doors for me, for building bridges between your world and mine, for teaching me to do the same. Mom, thank you for sharing with me your grace and strength and love,

for always picking up the phone, for driving through blizzards when I needed you most. Thank you both so much for supporting me through this chapter of my life and helping me begin the next.

Contents

1 Introduction

> *If science is a "commitment to truth" shall we [cite] all the historical non-truths perpetuated by scientists ? Of course not. It's not science vs Philosophy ... It's Science + Philosophy. Elevate your Thinking and Consciousness. When you measure include the measurer.*
>
> **— Stanley Kirk Burrell**
> *@MCHammer, February 21, 2021*

1.1 The Evolution of Galaxy Evolution

Human beings have practiced astronomy since time immemorial, with every civilization and culture in recorded history expanding and building upon our understanding of the night sky. Some of the earliest traces of our astronomer ancestors can be found in the stone circles of Nabta Playa in modern-day Egypt, where a nomadic people tracked the summer solstice as early as 4800 B.C.E (McK Mahille et al., 2007).

By contrast, the field of extragalactic astronomy could be said to have been born on New Year's Day 1925 with the announcement of Edwin Hubble's discovery of Cepheid variable stars in spiral nebulae (Hubble, 1925). Building on the pioneering work of Henrietta Swan Leavitt, Hubble then conclusively demonstrated that these objects lie far outside the edges of the Milky Way and could thus be considered "island universe" distinct from our own. This discovery laid to rest the "Great Debate" on the nature of the nebulae and opened the door for a new astronomical quest: to understand the nature of the universe beyond the confines of the Milky Way.

1.1.1 The bimodal universe

The widespread acceptance of this new paradigm of "island universes" triggered the first wave of galaxy surveys. One of the major results from this flurry of observations was the classification scheme produced by Hubble. In its simplest form, this separated galaxies into elliptical and spiral morphologies (Hubble, 1926). The division of the population into two distinct classes remains an enduring aspect of descriptions of galaxy populations, though the axes along which galaxies are separated have evolved and expanded with time.

Even in the original paper laying out this observed bimodality of galaxies, Hubble was quick to note that this "classification is descriptive and entirely independent of any theory". The search for physically-motivated models that explain the formation and evolution of these two populations is one of the major animating forces of modern extragalactic astronomy.

Thankfully, modern astronomy has advanced significantly since the $\mathrm{N} \sim 400$ object surveys that produced the first assessments of galaxy bimodality. Like the galaxies they seek to observe, modern galaxy observations can also be split into two categories, this case wide-field surveys of statistically large samples versus targeted, in-depth investigations of a small number of individual objects.

The archetypal wide-field galaxy survey of the modern era is the Sloan Digital Sky Survey (SDSS; York et al., 2000). In its first data release, it produced photometry for objects over 2,099 square degrees and spectroscopy for 186,250 objects (Abazajian et al., 2003). The most recent release (DR16) covers 14,555 square degrees with imaging and includes more than 5,000,000 (Jönsson et al., 2020). Complementary to SDSS are the Galaxy Evolution Explorer (GALEX, covering the near and far ultraviolet wavelength; Martin et al., 2005), the Two-Micron All Sky Survey (2MASS, in the near infrared; Skrutskie et al., 2006), and ALFALFA (21cm; Giovanelli et al., 2005), which collectively provide photometry across an

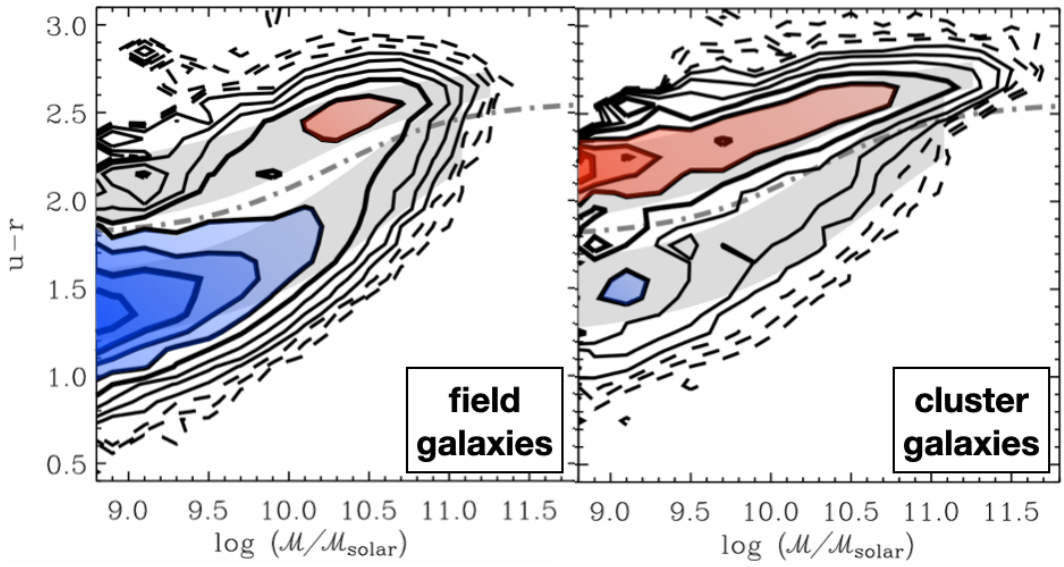

Fig. 1.1: The number density of galaxies in the local universe from SDSS ($z < 0.01$) as a function of galaxy color and stellar mass, split by local environment. Large $u - r$ indicates a redder color and a more quiescent galaxy. Quiescent galaxies can be seen at all stellar masses in high density environments like clusters, but quiescent galaxies are only common at high stellar mass in the field.
Adapted from Baldry et al. (2006).

unprecedentedly wide wavelength regime for objects in a massive swath of the sky. In combination with the spectroscopic redshifts derived from SDSS, the 2MASS Redshift Survey (Crook et al., 2007), and the Two-Degree and Six-Degree Field Galaxy Redshift Surveys (2dFGRS and 6dFGRS; Colless et al., 2001; Jones et al., 2004), modern astronomers effectively have access to the 3d positions and spectral energy distributions (SEDs) for millions of galaxies in the nearby universe. This allows for the consistent measurement of galaxy luminosities, sizes, colors, stellar masses, and more.

Thanks to this wealth of data, the demographics of the local universe have been extremely well characterized, with a few notable exceptions like the extremely low surface brightness regime. These population studies are now so numerous that it would be impossible to discuss them all. Instead, I will focus on one key observation: the distribution of galaxy colors as a function of galaxy stellar mass and local environment, shown in Figure 1.1 (Baldry et al., 2006).

Figure 1.1 highlights one of the major advances extragalactic astronomers have made in the last century: the galaxy bimodality depicted here is no longer detached from correlations with other galaxy properties, as it was in Hubble's morphological classification. The population is still clearly bimodal, with galaxies mostly observed as either red (large $u-r$) or blue (small $u-r$). However, there are also clear dependencies on physical quantities (stellar mass and local galaxy number density).

Moreover, color can also be directly connected to the evolutionary history of a galaxy. The modelling of simple stellar populations has shown that redder galaxies are dominated by older stellar populations and lack significant amounts of recent or on-going star formation (Kauffmann et al., 2003a; Brinchmann et al., 2004; Salim et al., 2007). This population is often referred to as "quiescent", in contrast to "star-forming" galaxies, which are bluer, dominated by young stellar populations, and experiencing on-going formation of stars.

The distribution of galaxies shown in Figure 1.1 indicates that a galaxy's environment and mass are good predictors of whether that galaxy will be actively forming stars or not. Quiescent galaxies are found at all stellar masses in dense environments like galaxy clusters, suggesting that the cluster environment may inhibit star formation. Meanwhile, in uncrowded and sparse field environments, only massive galaxies are frequently observed as quiescent.

Most galaxies that Hubble defined as ellipticals are quiescent, and most spiral galaxies are star-forming, but it is worth noting that not all star forming galaxies are spirals and not all quiescent galaxies are ellipticals. This is especially true for low mass galaxies, and in the high redshift universe. Understanding the forces that shape galaxy morphology is remains an active and fruitful area of investigation that has provided many insights into galaxy formation (Conselice et al., 2014), but these studies lie beyond the purview of this thesis.

1.1.2 The evolving universe

Figure 1.1 shows the color-based bimodality of galaxies in the local universe ($z < 0.08$), as they exist 13.7 billion years after the Big Bang. We cannot observe the evolution of individual galaxies in real time, but the finite speed of light allows for the characterization of the galaxy population at earlier times through the observations of galaxies at increasingly large distances.

One major undertaking has been the measurement of the cosmic star formation density, which informs our picture of when and how galaxies formed. Star formation in the universe as a whole peaked at $z \sim 1.9$ and has been declining exponentially ever since. Half of all stars observable today formed in the first ~ 4 Gyr after the Big Bang (Madau & Dickinson, 2014).

The bimodality of galaxies remains a consistent feature of the universe looking back to at least $z \sim 2-3$. However, studies have shown that the relative number and mass densities of star forming and quiescent galaxies have actually been changing over cosmic time. Since $z \sim 2$, the mass density of massive quiescent galaxies has increased by a factor of 10. Approximately half of this increase is due to the mass growth of individual galaxies (primarily through mergers) but the remainder can only be explained by the transition of some galaxies from star-forming into quiescence (Brammer et al., 2011).

Quiescent galaxies are therefore not a totally separate class of galaxy with a formation mechanism independent of star-forming galaxies. Rather, they are an evolution of star-forming galaxies into a second stage of life.

This transition from star forming into quiescence ("quenching") is not a monolithic processes. There appear to be many mechanisms that can disrupt star formation. Some of these processes are permanent and some only quench galaxies on a temporary basis. A large number of quenching mechanisms are linked to dense

environments and interactions between galaxy, but there are also processes internal to galaxies which are capable of quenching galaxies, and there is a subset of galaxies which may have been quenched by reionization in the very early universe.

1.2 Quenching and Feedback Mechanisms

An extremely diverse set of processes can contribute to galaxy quenching. To quench a galaxy means to prevent the formation of new stars and quenching processes usually achieve this by either heating gas such that it cannot collapse into new stars or removing the gas from the galaxy entirely. Additionally, for star formation to be permanently shut off, the gas needs to be either unable to cool or be re-accreted onto the galaxy, depending on how quenching originally occurred (Kerês et al., 2005).

These processes can originate external to the galaxy being quenched (e.g., outflows from nearby massive galaxies, ram pressure stripping in a cluster) or internal to the galaxy (e.g., shock heating from supernovae, radiation pressure from active galactic nuclei). External processes (particularly the extreme effects of the cluster environment) can quench galaxies at all stellar masses, while internal processes appear to act in two distinct mass regimes, as shown in Figure 1.2. A brief overview of some of the most common and impactful processes is given below.

1.2.1 Environmental quenching

We saw in Figure 1.1 that environment appears to be extremely effective at quenching galaxies, producing quiescent galaxies at all stellar masses in dense cluster environments (Smith et al., 2012). There exist a wide range of galaxy environments, from massive clusters in $\mathrm{M_h} = 10^{15}\ \mathrm{M_\odot}$ halos to sparse groups with just a handful of galaxies, that can influence galaxy evolution.

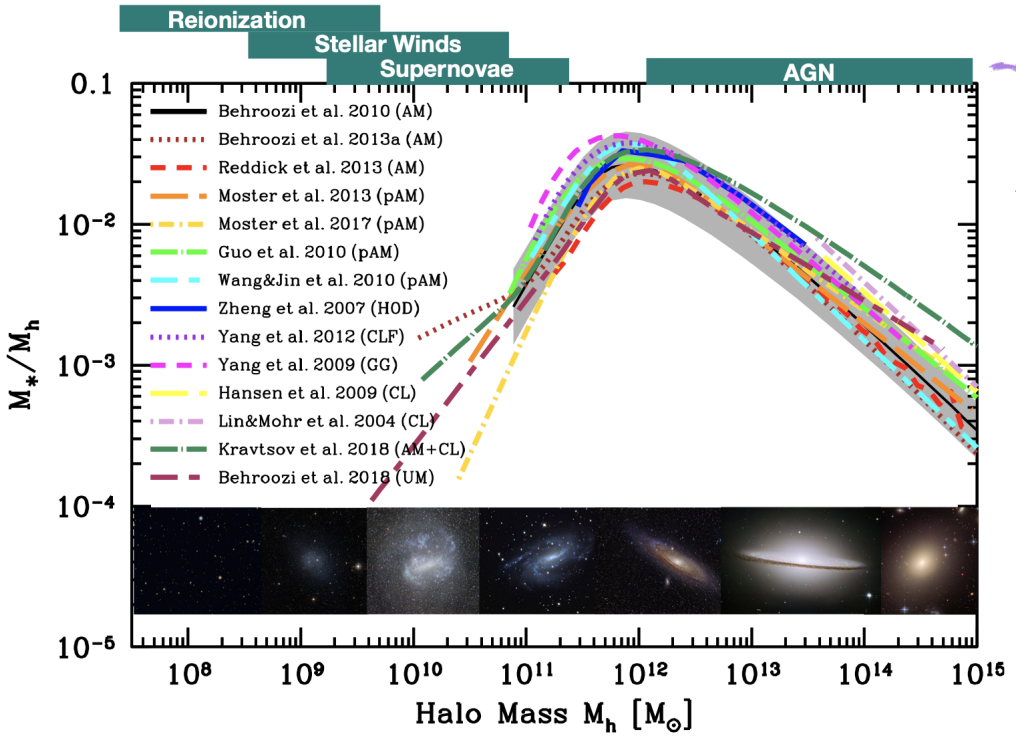

Fig. 1.2: The stellar mass to halo mass ratio as a function of halo mass for isolated galaxies. A lower stellar mass to halo mass ratio means that fewer baryons have been converted to stars, suggesting either star formation is less efficient or more easily disrupted. The suppression of the stellar mass to halo mass ratio towards both low and high halo masses suggests that there are two regimes for internal quenching, operating in galaxies more and less massive than the Milky Way, respectively. Adapted from Wechsler and Tinker (2018).

In addition to the large scale environment, small scale environment also plays a significant role. Satellites of a more massive undergo very different evolutionary paths compared to isolated galaxies of similar masses (Pasquali et al., 2010). The presence of a more massive halo around a satellite galaxy prevents the accretion of new gas onto the galaxy due to the continual removal of the gas reservoir through a combination of tidal interactions and ram-pressure stripping.

1.2.2 Stars and supernovae

The energy produced by supernovae (SNe) has long been considered a potential method for heating gas and even removing it from galaxies entirely (Dekel & Silk, 1986; White & Rees, 1978; White & Frenk, 1991). Star clusters and massive stars also contribute through radiation pressure, stellar winds, and photo-ionization (Hopkins et al. 2012). Critically, these effects in combination have been shown to be extremely effective at heating gas and disrupting star formation in low mass galaxies, and may be the drivers of the patchy and irregular star formation seen in many isolated dwarf galaxies.

1.2.3 Active galactic nuclei

Since their initial discovery, supermassive black holes (SMBHs) have gone from rare and mysterious to very nearly quotidian, an expected feature of almost all galaxies. A large number of formerly puzzling observations (e.g., QSOs, Seyfert galaxies) can now be chalked up to the accretion of gas onto a central black hole, with the diversity of observed phenomena explained by viewing angles and the extremely short (astronomically-speaking) timescales involved.

Active galactic nuclei (AGN) remain a fascinating topic to study in their own right, but they have increasingly become a centerpiece of theories of galaxy evolution

(Heckman & Best 2014; Kormendy & Ho 2013). Observations have shown that the growth rate of SMBHs tracks the cosmic star formation rate to a striking degree. The synchronicity of these two quantities over nearly 11 Gyr strongly suggests a connection between the two.

AGN are widely considered to have two main modes: radiative (Silk & Rees 1998) and kinetic (Fabian 1994). Through these two modes, AGN entrain and heat gas, produce high velocity gas outflows, and may contribute to the build up of stellar bulges. These effects are most prominent in massive galaxies (Croton et al., 2006), especially those in groups and clusters, where the AGN appears necessary for the maintenance of quiescence after star formation has ceased (Gaspari et al., 2013).

1.3 Challenges to Studying Galaxy Quenching

Directly identifying quenching mechanisms at work from observations of galaxies remains a difficult task, as it is impossible the watch the cause and effect of a feedback process(es) turning on and triggering quenching of individual galaxy in real time. Simulations of galaxies can be a highly information way to study feedback processes and galaxy evolution, as it is possible to trace the evolution of a single galaxy across cosmic time and to track the positions and properties of stars, gas, and dust throughout. Additionally, it is possible to vary the strength of various feedback processes and rerun identical volumes to explore the effects of different schema (Pontzen et al., 2017).

While galaxy simulations have incredible potential for understanding the mechanics of feedback and quenching, the massive range of physical scales that must be modelled remains computationally prohibitive. Extremely small-scale simulations (zoom-ins) have been able to explore phenomena like black hole accretion disks

in extreme detail and high fidelity, but cannot encompass entire galaxies, let alone volumes large enough to contain statistically meaningful galaxy populations.

Hydrodynamical simulations of cosmological volumes large enough to have statistically significant numbers of galaxies, but the wide range in relevant physical scales involved require approximations of the underlying physics in order to remain computationally tractable. These "subgrid models" include approximations for the mechanics of star formation, the heating and cooling of gas, the formation and growth of black holes, and the ejecta from active galactic nuclei and evolving stars (Somerville & Davé, 2015). The exact balance and interplay of these processes remain uncertain and an area of ongoing study. As such, it is necessary to "tune" the feedback models by hand to a selection of observations of galaxy populations.

Furthermore, the quantities that are directly output from simulations are very different from those measured from observations. The three-dimensional distributions of gas and star particles are far removed from the radial profile of a galaxy's light in optical imaging, for instance. Any derivation of physical quantities from observations requires a host of intermediary assumptions, and will be effected by noise and errors intrinsic to the measurements themselves. Surveys that aim to catalog populations of galaxies are further effected by incompleteness.

Plenty of work has gone into the creation of more robust derivations of physical quantities from observations (e.g., SED fitting, Conroy & Gunn, 2010) and more realistic mock observations of simulations (e.g., accounting for radiative transfer). But there remains a persistent gap, such that studies that utilize both observations and simulations almost always make "apples to oranges" comparisons between the two.

1.4 Boundary Conditions in Galaxy Evolution

This thesis focuses on low mass, quiescent galaxies in the local universe, with the goal of providing meaningful constraints on the feedback mechanisms that drive quenching in low mass galaxies.

In particular, this body of work is originally motivated by a single measurement: the quiescent fraction of isolated galaxies in SDSS DR8 (Figure 1.3). As shown in Geha et al. (2012), the quiescent fraction begins to drop off sharply below $M_* = 10^{10}$ $M_\odot$, so much so that below $M_* = 10^9$ $M_\odot$, no isolated and quiescent galaxies are observed in the SDSS volume. The black arrows at left in Figure 1.3 indicate the 3σ upper limits on the number of quiescent galaxies given the SDSS volume and survey sensitivity.

This sharp drop off in the quiescent fraction at $M_* = 10^9$ $M_\odot$ suggests that galaxies can self-quench only when above this mass threshold. This presents a strong constraint on the internal feedback mechanisms that quench low mass galaxies. Supernovae, stellar winds, and AGN are all possible sources for driving feedback in galaxies just above this quenching threshold, but their relative impact on the evolution of low-mass galaxies remains uncertain. Whatever process(es) regulate or disrupt star formation in low mass galaxies must obey this boundary condition by only quenching galaxies above the mass threshold.

1.4.1 AGN are ubiquitous in low mass, quiescent galaxies in isolation

The low mass quenching threshold identified in SDSS provides a unique opportunity to explore how galaxies are effected by feedback processes. However, these galaxies

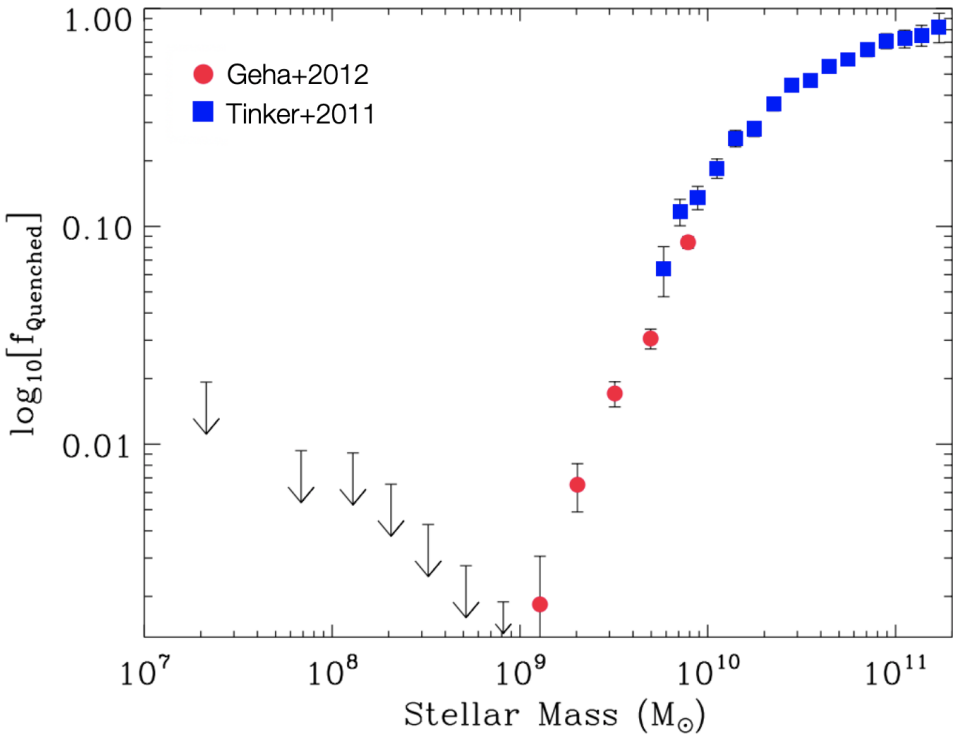

Fig. 1.3: The quiescent fraction of isolated galaxies in SDSS, adapted from Geha et al. (2012). Black arrows represent the 3σ upper limits on the quiescent fraction based on the SDSS volume and survey sensitivity.

were identified with SDSS fiber spectroscopy, which has limited spectral resolution and lacks spatial resolution entirely.

To build a comprehensive portrait of the quiescent galaxies just above the SDSS quenching threshold, Keck/ESI long-slit spectroscopy was acquired for all quiescent galaxies in isolation with $\mathrm{M}_* = 10^{9.0-9.5}\ \mathrm{M}_\odot$ from SDSS. In Chapter 2, I present an in-depth exploration of what may be the lowest mass galaxies that are able to self-quench on galaxy-wide scales. The high-resolution, spatially-resolved spectroscopy proved critical for in-depth studies of the emission line properties of these galaxies.

Intriguingly, I identified emission in the majority of the quiescent galaxies, even though our definition of quiescence is based on $\mathrm{H}\alpha$ EW. Using the Baldwin Phillips Terlevich (BPT) diagram, I confirmed that 16 of the 20 quiescent galaxies in our sample host central AGN-like line ratios. We also found that many of the quiescent galaxies in our sample have spatially-extended emission across the non-SF regions of BPT-space.

Despite their overall passive appearances, nearly all low-mass quiescent galaxies host AGN, in contrast to denser environments, where we observe significant numbers of quiescent galaxies lacking AGN signatures. These results suggest that the presence of hard ionizing radiation (AGN-like line ratios) is tied to the quenching of what may be the lowest-mass self-quenched galaxies.

This work dovetails with a bevy of other studies focused on AGN in low mass galaxies. Penny et al. (2018) found a set of quiescent galaxies in group environments with both AGN-like BPT line ratios and disturbed gas kinematics, while Manzano-King et al. (2019) found outflowing gas with AGN-like line ratios, both suggesting AGN-driven outflows. Bradford et al. (2018) studied the HI gas masses of isolated low-mass galaxies with BPT-identified AGN and found two populations; composite galaxies with gas content in line with non-AGN galaxies and gas-depleted galaxies

with stronger AGN signatures. Taken altogether, these results suggest that AGN may be able to significantly affect the cold gas content of galaxies with low stellar masses. Finally, in Baldassare et al. (2020), we found that these isolate dwarf galaxies still lie on the $\mathrm{M_{BH}} - \sigma_*$ relation, which in more massive galaxies is considered strong evidence for the role AGN play in shaping galaxy evolution.

1.4.2 Galaxy simulations over-quench isolated, low mass galaxies

My findings in Chapter 2 and the many recent complementary studies present a challenge to the narrative about internal galaxy quenching, in which AGN are important in massive galaxies, but have little influence on the quenching of low mass galaxies (Martín-Navarro & Mezcua, 2018; Bower et al., 2017). This is the picture that many modern large scale hydrodynamic simulations have implemented via their sub-grid approximations of feedback processes (Somerville & Davé, 2015; Vogelsberger et al., 2020), in some cases explicitly preventing AGN feedback in low mass galaxies.

Whatever feedback processes quench low mass galaxies in isolation, they produce the characteristic quenching threshold observed in SDSS. Given the growing body of evidence for AGN exerting influence on the quenching of low mass galaxies in isolation, in Chapter 3 I ask: are simulations that do not include any AGN feedback at low masses able to reproduce this characteristic observation of isolated, quiescent galaxy population at low stellar mass?

In this work, I focused on three large volume ($\mathrm{L} \sim 100\ \mathrm{Mpc}$) comsological and hydrodynamical simulations (EAGLE, Illustris-TNG100, and SIMBA). The data from these simulations were collated by the Isolated & Quiescent Collaboratory[1] (Hahn et al., 2019). In that first paper from the Collaboratory, our goal was to make meaningful comparisons between simulations, and we focused on "direct from output"

[1] https://iqcollaboratory.github.io/

quantities, like star formation rates based on the cold gas particles bound to a galaxy, selected in ways that account for variable resolution between simulations. However, to make similarly meaningful comparisons between simulations and observations requires the creation of full mock surveys from the simulations, a significantly more involved process.

To that end, I developed Orchard[2], a self-consistent framework for making apples-to-apples comparisons between simulations and observations. Through the IQ Collaboratory we have created synthetic spectra for all galaxies in our suite of simulations. What makes the IQ spectral database unique is that it was generated for the three simulations with an identical methodology, which accounts for variations in mass and time resolution. Orchard builds on this to create realistic observations, based on the SDSS noise function and resolution, and then realistic SDSS-like surveys "observed" through each simulation volume, designed to match SDSS incompleteness.

The quiescent fraction shown in Figure 1.3 rely on three key definitions: isolated, low mass, and quiescent. I replicated the measurement of the relevant quantities ($\mathrm{D_{host}}$, $\mathrm{M_*}$, $\mathrm{H}\alpha$ EW, and $\mathrm{D_n4000}$) and used identical definitions for each. From there, I was able to measure the quiescent fraction of isolated galaxies at low mass and compare directly to the quiescent fraction measured in SDSS.

All three simulations showed a decrease in the number of quiescent, isolated galaxies in the mass range $\mathrm{M_*} = 10^{9-10}\ \mathrm{M_\odot}$, in broad agreement with the trend seen in the observations. However, even after accounting for observational and selection biases, none of the simulations could reproduce the observed absence of quiescent field galaxies below $\mathrm{M_*} = 10^{9}\ \mathrm{M_\odot}$.

Examining the underlying star formation histories of the quiescent galaxies below the observed quenching threshold, I found significant variation in the late

[2]https://github.com/IQcollaboratory/orchard

time star formation histories, but relatively consistent quenching timescales (as measured from t_{90}).

I considered several physical processes that may be contributing to the over-quenching of isolated, low mass galaxies seen in the simulations. High resolution zoom-in simulations of extremely low mass galaxies have demonstrated that feedback from star formation can reduce gas density and temporarily expel large quantities of gas from dwarf galaxies. It remains uncertain just how permanent this gas depletion can be, particularly in galaxies with $M_* \sim 10^{8-9}\ M_\odot$, where the gas should be more tightly bound.

1.4.3 Galaxy simulations may be over-tuned to reproduce Local group satellites

In Chapter 3 I found that three major large volume galaxy simulations have an "over-quenching" problem for low mass galaxies in isolation. I discussed some of the physical processes that could be producing this quiescent population but did not tackle the sub-grid tuning processes that could also contribute to the tension between the simulations and observations.

Simulations must be tuned to successfully reproduce observations of the universe. A common benchmark for the success of a particular "recipe" for feedback processes is the presence of a Milky Way or Local Group-like system in the simulation volume. The Milky Way and its satellites are the most well-studied central-satellite system in the universe. Intriguingly, dark-matter-only simulations struggle to produce configurations of subhalos that would match the Milky Way and Local Group systems. More complex treatments of baryonic processes (e.g., feedback) is often cited as a potential solution to this disagreement. As such, simulations point to the

presence of Milky Way-like central-satellite systems as validation of the particular suite of sub-grid approximations in use.

In Chapter 4, I compared three major large-scale hydrodynamical galaxy simulations (EAGLE, Illustris-TNG, and SIMBA) by forward modeling simulated galaxies into observational space and computing the fraction of satellites of Milky Way analogs that are quiescent as a function of stellar mass. Using the SAGA survey as our observational template, I created mock surveys and synthetic spectroscopic and photometric observations of each simulation, adding realistic noise and observational limits.

All three simulations showed an increase in the number of quiescent satellite galaxies, in good agreement with observations of the Local Group satellites. However, the SAGA survey showed significantly lower quiescent fractions for satellites of Milky Way analogs. I found that the simulations also produce a population of faint, red satellites that have not been detected by the SAGA survey. These galaxies have extremely old ages and represent either a population that has thus far been missed by observations or artifacts of unphysical processes in the simulations.

I identified analogs of this population in a wide variety of environments, from isolation to dense groups. I also used the mock surveys to demonstrate the sensitivity of definitions of quiescence to observational noise.

1.5 Looking Forward

In this thesis, I have argued that existing models of galaxy feedback fail to reproduce and explain observations of low mass galaxies, including both characteristics of the populations at large and detailed studies of individual galaxies. I found that the majority of the isolated, quiescent galaxies just above the low mass self-quenching

threshold show signatures of on-going AGN activity and found that three large-volume hydrodynamical simulations which do not prioritize AGN feedback at low mass fail to reproduce the characteristic quenching threshold seen in SDSS. Additionally, while these simulations consistently produce central-satellite systems that are very similar to the Milky Way and its satellites, they also fail to match the broader distribution of satellites of Milky Way analogs as measured in the SAGA survey.

My work has been particularly focused on the necessity of "apples to apples" comparisons as the basis of any meaningful measurement. By acknowledging and actively folding in observational biases to analyses of galaxy simulations, I have demonstrated that these simulations have an "over-quenching" problem.

Critical to this work has been Orchard, the methodology I developed to create mock surveys from simulations. Looking forward, there are many clear directions in which Orchard can continue to grow, which I have loosely grouped into three categories: new inputs, new outputs, and new constraints.

Orchard currently uses three large-volume hydrodynamical simulations as input from which synthetic observations and surveys are derived. The spectra created by the IQ Collaboratory from these simulations were intentionally generated in a manner that would also be compatible with extremely high-resolution zoom-in simulations as well as massive-volume semi-analytic models with unresolved galaxies. Suites of zoom-in galaxies will offer a much more detailed picture of current feedback models in action. Of particular interest are the Romulus simulations, which offer improved resolution but retain enough volume for statistically significant measurements ($\mathrm{L} \sim 25\ \mathrm{Mpc}$) and most notably, prioritize realistic black hole feeding and feedback even in low mass galaxies. Additionally, semi-analytic models like the Santa Cruz SAM offer the chance for on-the-fly variation of feedback prescriptions, which can be used to search for paradigms that successfully reproduce observed galaxy populations.

Thus far, I have focused on measuring just two observational indices from the synthetic spectroscopy outputted from Orchard: $\mathrm{H}\alpha$ EW and $\mathrm{D_n}4000$. However, galaxy spectra encode incredible amounts of information and it is becoming increasingly feasible to derive the complete star formation histories of galaxies from their spectra. In Chapters 3 and 4 we examined the "true" star formation histories of simulated galaxies. Going forward, it will be possible to measure star formation histories from spectra of observed and simulated galaxies via the same SED fitting techniques. Taking the additional step of driving "observed" star formation histories from the synthetic observations of the simulations is critical for preserving the apples to apples nature of future work. Robust limits on quenching timescales as derived from star formation histories will provide informative constraints for future studies of feedback in low mass galaxies. Additionally, a library of star formation histories derived from SED fitting of realistic synthetic observations and the corresponding "true" star formation histories with a diverse variety of characteristic shapes will help future survey designers understand what levels of wavelength coverage, wavelength and velocity resolution, and signal-to-noise are necessary for meaningful observations of low mass galaxies.

Finally, we are rapidly entering a new era of observational astronomy which is rapidly unveiling the low surface brightness universe. Upcoming and on-going surveys from the Dark Energy Spectroscopic Instrument, the Vera Rubin Observatory, Hyper Suprime-Cam, and Dragonfly have the potential to reveal previously unseen populations of low surface brightness galaxies in the local universe. This may lead to significant revisions of plots like Figure 1.3 and in turn resolve the tensions between the simulations and current observations (assuming that at least some of the low mass quenched galaxies in simulations are also low surface brightness). Taken altogether, these new and upcoming inputs, outputs, and constraints offer a robust path forward for both Orchard and studies of feedback and quenching in low mass galaxies.

2

AGN all the way down? AGN-like line ratios are common in the lowest mass, quiescent galaxies in isolation

"Your theory that the sun is the centre of the solar system, and the earth is a ball which rotates around it has a very convincing ring to it, Mr. James, but it's wrong. I've got a better theory," said a little old lady.
"And what is that, madam?" inquired James politely.
"That we live on a crust of earth which is on the back of a giant turtle."
"If your theory is correct, madam," he asked, "what does this turtle stand on?"
"You're a very clever man, Mr. James, and that's a very good question," replied the little old lady, "but I have an answer to it. And it's this: The first turtle stands on the back of a second, far larger, turtle, who stands directly under him."
"But what does this second turtle stand on?" persisted James patiently.
To this, the little old lady crowed triumphantly,
"It's no use, Mr. James—it's turtles all the way down." – *J. R. Ross, 1967*

Claire Dickey, Marla Geha, Andrew Wetzel, and Kareem El-Badry, *The Astrophysical Journal*, **884**, 180 (2019)

ABSTRACT

We investigate the lowest-mass quiescent galaxies known to exist in isolated environments ($M^* = 10^{9.0-9.5}$ $M_\odot$; 1.5 Mpc from a more massive galaxy). This population may represent the lowest stellar mass galaxies in which internal feedback quenches galaxy-wide star formation. We present Keck/ESI long-slit spectroscopy for 27 isolated galaxies in this regime: 20 quiescent galaxies and 7 star-forming galaxies. We measure emission line strengths as a function of radius and place galaxies on the Baldwin Phillips Terlevich (BPT) diagram. Remarkably, 16 of 20 quiescent galaxies in our sample host central AGN-like line ratios. Only 5 of these quiescent galaxies were identified as AGN-like in SDSS due to lower spatial resolution and signal-to-noise. We find that many of the quiescent galaxies in our sample have spatially-extended emission across the non-SF regions of BPT-space. Despite their overall passive appearances, nearly all low-mass quiescent galaxies host AGN, in contrast to denser environments, where we observe significant numbers of quiescent galaxies lacking AGN signatures. Our results suggest that the presence of hard ionizing radiation (AGN-like line ratios) is tied to the quenching of what may be the lowest-mass self-quenched galaxies.

2.1 Introduction

Understanding the processes that regulate star formation and quench galaxies remains a major goal for studies of galaxy evolution. Since the advent of the hierarchical CDM paradigm, a feedback mechanism or mechanisms have often been invoked to explain the discrepancies between the observed stellar mass function and the halo mass function. (White & Rees, 1978; Dekel & Silk, 1986; White & Frenk, 1991). Feedback mechanisms fall into two categories: processes that arise in high-density environments and those that are internal to galaxies (Peng et al., 2010). A diverse set of external phenomena (ram-pressure stripping, tidal forces, major and minor mergers, etc.) are able to remove or heat gas in group and cluster environments and are particularly effective in low-mass galaxies (e.g., Pasquali et al., 2010; Smith et al., 2012). Within individual galaxies, active galactic nuclei (AGN) appear necessary to produce the observed population of massive quenched galaxies (e.g., Croton et al., 2006; Somerville et al., 2008; Choi et al., 2015; Su et al., 2018), heating gas via high-velocity winds and radio jets. The efficiency of internal versus external quenching mechanisms is a strong function of galaxy mass; with high-mass galaxies dominated by processes internal to themselves and low-mass galaxies exclusively quenched by environmental effects (Somerville & Davé, 2015).

While environmental processes can effectively quench galaxies across almost all mass regimes (the most massive galaxies being an exception; Peng et al., 2010; Wetzel et al., 2013), the efficiency of self-quenching is thought to be tightly correlated with mass. Geha et al. (2012) found that there is a stellar mass threshold below which isolated galaxies at $z < 0.055$ in the Sloan Digital Sky Survey (SDSS; Aihara et al., 2011) cannot quench themselves. They found that all of the several thousand galaxies with $\mathrm{M}_* = 10^{7.0-9.0}\ \mathrm{M}_\odot$ identified in SDSS as isolated (defined as 1.5 Mpc from a more massive companion), were star-forming (despite the existence of

quiescent galaxies in non-isolated environments in the same mass regime). Whatever process(es) act within low-mass galaxies to disrupt star formation either become inefficient or cannot occur below $\mathrm{M}_* = 10^{9.0}\ \mathrm{M}_\odot$. This quenching threshold is also observed to be consistent across redshift (Papovich et al., 2018). Supernovae, stellar winds, and AGN are all possible sources for driving feedback in galaxies just above this quenching threshold, but their relative impact on the evolution of low-mass galaxies remains uncertain. While it is widely agreed that AGN are both ubiquitous and influential in massive (L^*) galaxies, a key question is whether AGN play a role in quenching all the way down to the lowest-mass isolated quiescent galaxies.

Constraining the mechanisms responsible for quenching low-mass galaxies is challenging for a variety of reasons. The physics underlying AGN feedback remains poorly understood, such that simulations must be tuned to reproduce observed galaxy scaling relations (e.g., Bower et al., 2006; Somerville et al., 2008; Gabor et al., 2011; Genel et al., 2014; Schaye et al., 2015). Cosmological simulations are thus limited in their ability to constrain the influence of AGN, particularly in low-mass galaxies which often lie at the limits of resolution. While some zoom-in simulation studies are beginning to include isolated galaxies with $\mathrm{M}_* = 10^7 - 10^9\ \mathrm{M}_\odot$ (e.g., Graus et al., 2019), there has been minimal focus on AGN and robust observational data to test against remains sparse.

Additionally, identifying AGN in low-mass galaxies remains difficult. Stellar or gas dynamics are the most secure method for discovering supermassive black holes (for a review see Kormendy & Kennicutt, 2004), but resolution limits largely prohibit the use of this technique beyond the confines of the Local Group. In more distant systems, it is possible to identify actively accreting systems using broad Hα which traces gas orbiting in a deep potential well (e.g., Greene & Ho, 2007), and narrow emission line ratios which can distinguish between different sources of ionizing radiation (e.g., Barth et al., 2008; Reines et al., 2013). However, broad lines alone are not a conclusive indicator of AGN activity (Baldassare et al., 2016), and narrow

lines are subject to a variety of systematics and biases, discussed in more detail below.

Systematic searches rely on large spectroscopic surveys like SDSS, which are limited by the brightness of host galaxies for targeting, the strength of emission lines for identification, and contamination from the host galaxy which obscures AGN signals (e.g., Trump et al., 2015). Moreover, while BPT line ratios can be used to identify AGN candidates, without additional follow-up (e.g., X-ray emission, IR colors, etc.) emission cannot be conclusively identified as originating from an AGN (e.g., Yan & Blanton, 2012; Belfiore et al., 2017). The BPT diagram has also been found to be less effective at identifying intermediate black holes, creating further challenges (Cann et al., 2019) for the identification of AGN in low-mass galaxies.

Despite these challenges, the number of central black holes discovered in host galaxies with $\mathrm{M}_* < 10^{10}\ \mathrm{M}_\odot$ continues to grow. The discovery of individual galaxies with notably low-mass central black holes (e.g., Filippenko & Ho, 2003; Barth et al., 2004; Satyapal et al., 2007; Baldassare et al., 2015, etc.) has led to more thorough searches and dedicated surveys (e.g., Greene & Ho, 2007; Reines et al., 2013; Sartori et al., 2015; Baldassare et al., 2018, etc.). These studies rely on a variety of techniques, all of which suffer from observational biases (e.g., Trump et al., 2015; Agostino & Salim, 2019; Cann et al., 2019). Thus, the known population of AGN in low-mass galaxies is far from complete.

Recent studies suggest that central black holes may exert significant influence on their low-mass host galaxies. Penny et al. (2018) found a set of quiescent galaxies in group environments with both AGN-like BPT line ratios and disturbed gas kinematics, suggesting AGN-driven outflows. Bradford et al. (2018) studied the HI gas masses of isolated low-mass galaxies with BPT-identified AGN and found two populations; composite galaxies with gas content in line with non-AGN galaxies and gas-depleted

galaxies with stronger AGN signatures. They suggest that AGN may be able to affect the cold gas content of some galaxies with low stellar masses.

These studies exist in some tension with other work which suggests that stellar and supernovae feedback, rather than black hole accretion, are the dominant forces which moderate star formation in low-mass galaxies (e.g., Martín-Navarro & Mezcua, 2018; Bower et al., 2017).

In this work, we investigate the processes required to quench isolated galaxies, focusing on the lowest-mass galaxies that are isolated and lack recent star formation. We define galaxies as star-forming or quiescent based on observational properties as measured by the SDSS fiber spectroscopy. We consider galaxies to be quiescent if they have both old stellar populations and sufficiently low levels of star formation. We intentionally differentiate between *quenched* galaxies in which star formation has been fully and permanently disrupted and *quiescent* galaxies which are not currently forming stars but are not necessarily "dead".

We discuss the observational proxies and exact definitions used in section 2.2 and build a catalog of isolated low-mass galaxies. We present new Keck/ESI long-slit spectroscopy for a subset of these galaxies. In section 2.3 we measure emission line fluxes for galaxies as a function of radius and place them on the BPT diagram, categorizing individual galaxy spaxels as quiescent, star-forming, AGN-like, or composite. We identify central AGN candidates and classify the radial trends of galaxies on the BPT diagram. In section 2.4, we measure the perpendicular distance from the star-forming region in [O III]/Hβ vs. [N II]/Hα space, and connect this indicator of the relative strength of non-SF ionizing radiation to host galaxy properties. We summarize our work and its implications in section 2.5. We assume $\mathrm{H}_0 = 70\ \mathrm{km\ s^{-1}\ Mpc^{-1}}$ throughout this work.

2.2 Data

2.2.1 Galaxy catalog and isolation criterion

The parent sample for this work is the NASA/Sloan Atlas[1] (NSA; Blanton et al., 2011), a reanalysis of SDSS DR8, optimized for nearby low-luminosity objects. The NSA galaxy catalog includes fluxes, optical line strengths and equivalent widths, and associated errors for all objects derived using the methods of Yan & Blanton (2012) and the SDSS spectrophotometric recalibration of Yan (2011). The catalog also includes stellar masses, estimated with the `kcorrect` software (Blanton & Roweis, 2007), based on SDSS optical fluxes as well as GALEX fluxes where available, and assuming a Chabrier (2003) initial mass function.

Following Geha et al. (2012), we define galaxies as isolated based on the quantity $D_{\rm host}$, the projected distance to the nearest "luminous" neighbor, where luminous is defined to be $M_{K_s} < -23$ (corresponding to $\rm M_* = 2.5 \times 10^{10}\ M_\odot$). Luminous galaxies are considered to be potential host galaxies if they are within 1000 km $\rm s^{-1}$ in redshift and within a projected comoving distance of 7 Mpc. $D_{\rm host}$ is given as the shortest distance to a luminous neighbor within the search parameters. For the small number of galaxies where no luminous neighbor was identified, $D_{\rm host}$ was set to 7 Mpc. We consider a galaxy to be isolated if $D_{\rm host} > 1.5$ Mpc.

We focus on galaxies $\pm$ 0.5 dex around the isolated quenching threshold for a mass range of $\rm M_* = 10^{8.5} - 10^{9.5}\ M_\odot$ (Geha et al., 2012). The NSA catalog contains $\rm N = 6850$ isolated galaxies within this mass range.

Our definition of isolated selects for galaxies that are centrals rather than satellites, but does not discriminate based on large scale environment, unlike other measures (e.g., $3^{\rm rd}$ or $7^{\rm th}$ nearest neighbor, aperture counts, etc). Our galaxies all

[1] http://www.nsatlas.org

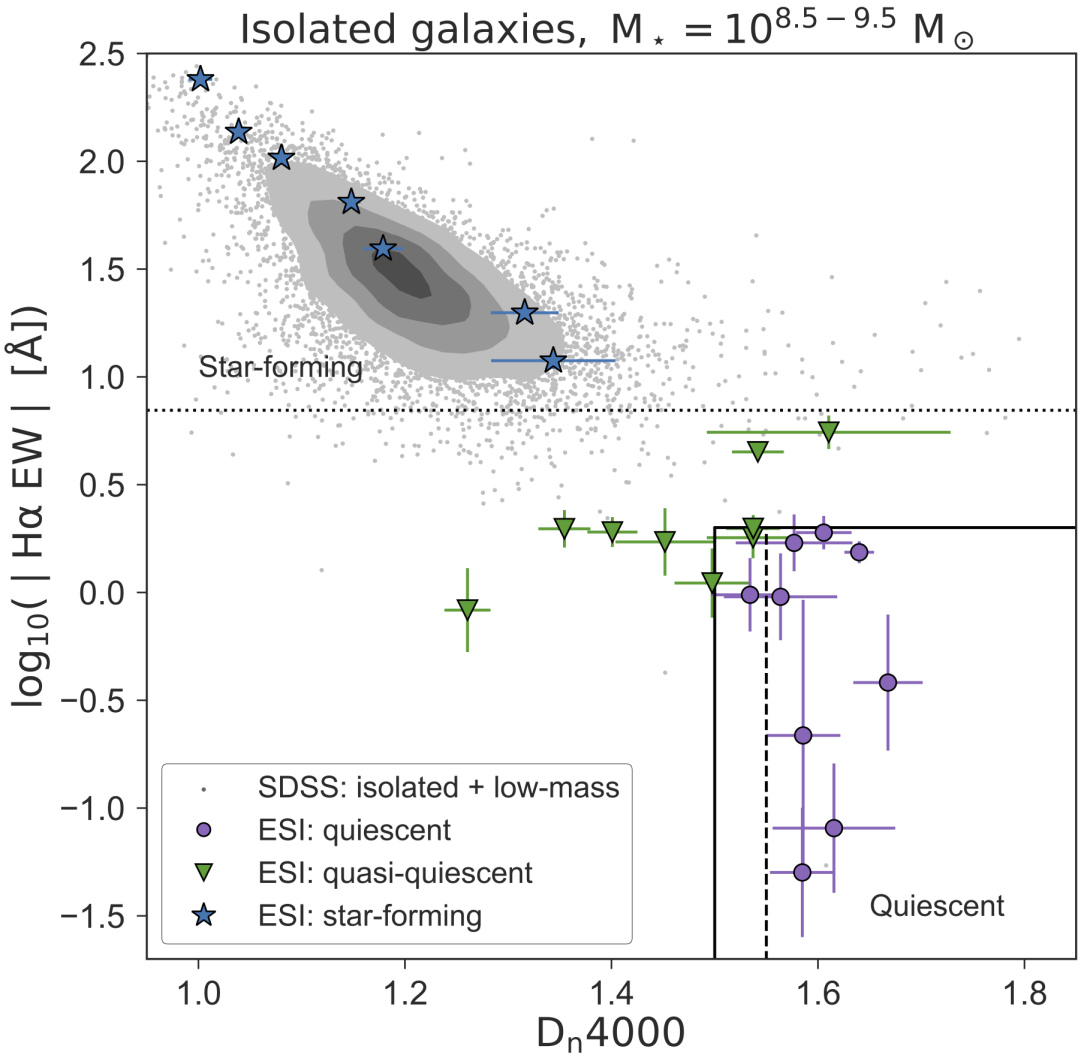

Fig. 2.1: D_n4000 vs Hα equivalent width for isolated ($D_{host} > 1.5$ Mpc), low-mass ($M_* = 10^{8.5} - 10^{9.5}\ M_\odot$) galaxy sample (gray points, contours), measured with SDSS. Galaxies for which we have obtained Keck/ESI spectroscopy are shown as colored points and divided into three types based on the strength of their 4000 Å breaks and Hα EWs: star-forming (blue stars), quasi-quiescent (green triangles), and quiescent (purple circles). Solid lines indicate the criteria for quiescence (D_n4000 has a mass dependence, and we show the highest-mass limit with a dashed line). Galaxies are considered to be quasi-quiescent if they lie below the dotted line.

live well beyond the virial radius of their nearest neighbor, but are not necessarily living in true cosmic voids (van de Weygaert & Platen, 2011).

Within this sample, we further define galaxies as quiescent, quasi-quiescent, or star-forming. We consider a galaxy to be quiescent based on two criteria measured from the SDSS fiber spectra: the $\mathrm{H}\alpha$ equivalent width (EW), which traces the specific star formation rate over the last $\sim 10-20$ Myr, and the $\mathrm{D_n}4000$ index, which is a measure of the light-weighted age of the stellar population and is based on the strength of the 4000 Å break (Balogh et al., 1999). Quiescent galaxies are those with $\mathrm{H}\alpha$ EW < 2 Å and $\mathrm{D_n}4000 > 0.6 + 0.1 \cdot \log_{10}(\mathrm{M}_*)$. We base these definitions on the empirical delineations between star-forming and quiescent populations in Geha et al. (2012). We remove 192 galaxies from the sample with poorly measured $\mathrm{D_n}4000$ ($\mathrm{D_n}4000_{\mathrm{err}} > 0.1$). In the mass range $\mathrm{M}_* = 10^{8.5} - 10^{9.5}$ $\mathrm{M}_\odot$, the majority of galaxies (6470 / 6658) are defined as star-forming and just 11 are quiescent, consistent with Geha et al. (2012). There are an additional 177 galaxies which we define as "quasi-quiescent" because they fulfill only one of our criteria for quiescence (large $\mathrm{D_n}4000$ and intermediate $\mathrm{H}\alpha$ EW, or low $\mathrm{D_n}4000$ and low $\mathrm{H}\alpha$ EW) based on their SDSS fiber-based spectroscopy. These galaxies are potential analogues to the Green Valley observed at higher stellar masses.

2.2.2 Keck/ESI observations

From the above sample, 27 isolated galaxies were observed over four nights (2014 March 6, 2014 March 7, 2015 January 19, and 2016 February 14) with the Echelle Spectrograph and Imager (ESI; Sheinis et al., 2002) on the Keck II 10m telescope.

In building our sample, we focused primarily on maximizing the number of quiescent galaxies observed, acquiring ESI observations for 10 of 11 quiescent galaxies, and an additional 10 of 177 quasi-quiescent galaxies which may be in the

process of transitioning from star formation to quiescence. Finally, we also observed 7 galaxies which span the full range of $\mathrm{D_n}4000$ and Hα EWs observed in star-forming, low-mass galaxies in SDSS (Figure 2.1, blue stars). Stellar masses, redshifts, $\mathrm{D_n}4000$ and Hα EW for each observed galaxy are given in Table 2.1. The observed galaxies in each subsample all have similar redshift distributions to the parent sample.

The observations were taken in echellette mode, which provides wavelength coverage over the range 3900-11000 Å, across 10 echelle orders. The observations were made using the 1.0″ x 20″ slit, which gives an instrumental resolution of $32\ \mathrm{km\ s^{-1}}$ (Gaussian σ) over the full spectrum or $R \approx 10,000$. For each galaxy, the slit was aligned along the major-axis and a minimum of three consecutive 5-minute exposures were obtained. We achieve $\langle \mathrm{SNR} \rangle \sim 10 - 25\ \mathrm{pix^{-1}}$ in the continuum across the Ca III region.

The ESI data were processed using the `XIDL` package[2] (Prochaska et al., 2003), following the ESIRedux cookbook to process the darks, flats, and arc images. The flat field images were used to trace the edges of the slit across each curved order and to correct gain mismatch across the amplifiers. From the individual arc images taken on each night, a master CuAr+HgNe+Xe arc image was created. From this master arc image the wavelength solution was derived for each night of observations.

Once the individual science frames were dark-subtracted and flat-fielded, cosmic rays were identified and removed with the routine `LACosmic` (van Dokkum, 2001). The individual science frames were median-combined and then the initially curved individual orders rectified.

To model the contribution from sky lines and continuum, we performed a bspline fit to a 2″-wide region on the outer edges of the 2d spectrum. In some cases, emission lines from the galaxy extend across the full slit (e.g., NSA 112551 in Figure 2.2). For these galaxies, we use the internal rotation of the galaxy to

[2]https://www2.keck.hawaii.edu/inst/esi/ESIRedux/index.html

select uncontaminated regions of sky on the opposite side of the slit. For the few galaxies with negligible rotation, we assume a flat sky continuum and fit to the regions directly surrounding the emission lines in wavelength-space.

2.2.3 Emission line measurements

We are interested in measuring the strength of emission lines in low-mass isolated galaxies such that we can isolate AGN-like line ratios. However, the majority of galaxies in our sample are dominated by the stellar *absorption continuum*. For accurate measurements of Hα and Hβ *emission*, it is necessary to model and remove the effects of stellar absorption.

For each galaxy in the sample, we fit the stellar continuum from the spectrum extracted within the central 1″ (as determined from the median stellar continuum profile at $\lambda = 8400 - 8800$ Å). After masking the strong optical emission lines, we convolve a set of empirical stellar templates with a velocity profile using pPXF (Cappellari, 2017) and fit to the central galaxy spectrum.

We have tested pPXF's ability to accurately recover the shape of the Balmer absorption lines by modeling a set of quiescent galaxies with and without emission line region masking. In all cases, the model produced by fitting to the line-masked spectrum is in good agreement with the model fit to the unmasked spectrum.

We assume that the relative line strength of the absorption features do not vary significantly as a function of radius. Given the stellar continuum derived from the continuum normalized central 1″, we use the median galaxy light profile to produce a two-dimensional (2d) map of the galaxy continuum.

We subtract the galaxy continuum model from the 2d sky-subtracted spectra to correct for stellar absorption. This produces a 2d emission-line-only spectrum, from

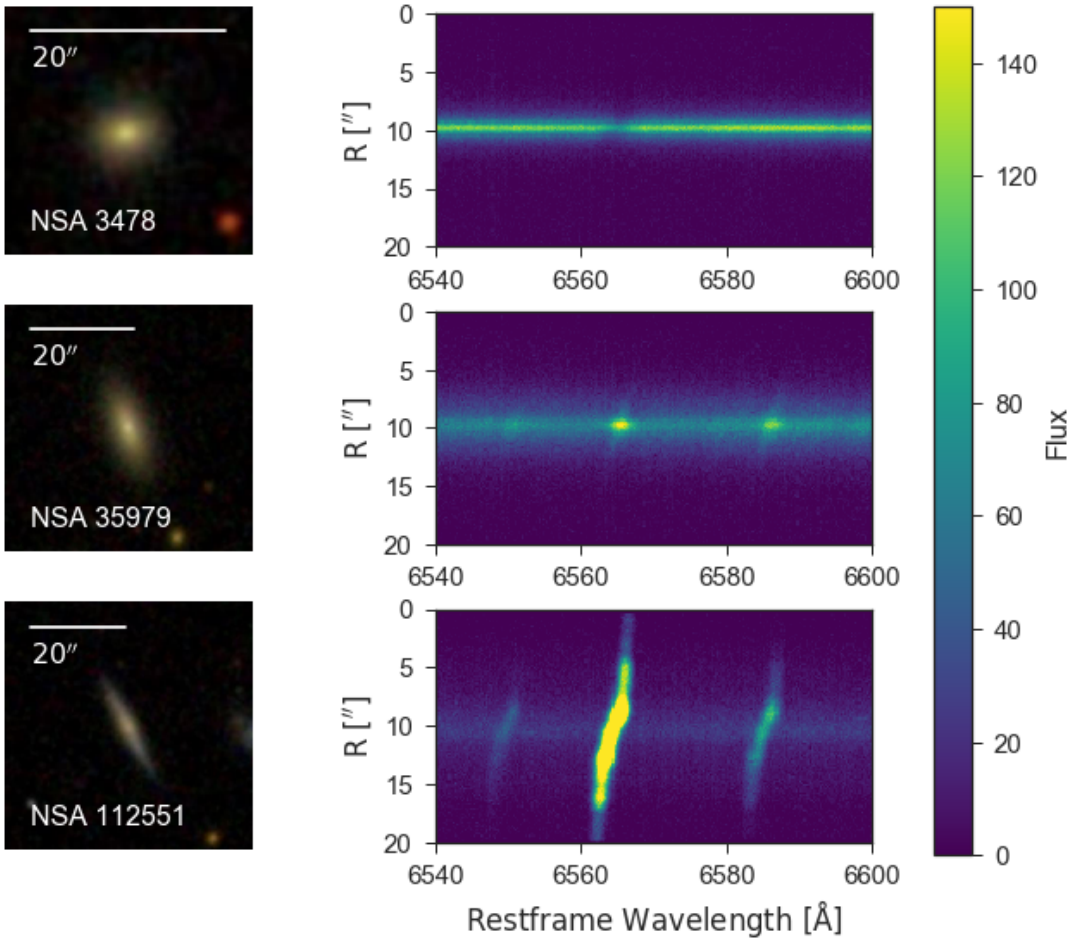

Fig. 2.2: SDSS gri images for 3 galaxies in our sample (left), and corresponding sky-subtracted 2d Keck/ESI spectra for each galaxy, centered on the Hα + [N II] region (right). Galaxies in our sample show a variety of emission line profile behaviors, with some dominated by stellar absorption (top), some showing only centrally-concentrated emission (middle), and some with emission line extending across the full slit (bottom). All galaxies shown here have similar stellar masses ($M_* \sim 10^{9.2-9.4}$ $M_\odot$).

which we can extract spatially resolved one-dimensional spectra for each galaxy. The central spectrum is centered on the peak of the galaxy brightness profile and extracted from a 1″-wide region (corresponding to the average seeing across our nights). Successive spectra are extracted at increasing radii with a width of 1″.

Given a set of spectra for each galaxy, we follow Reines et al. (2013) and model the emission lines of interest as Gaussians. We initially fit the Hα + [N II] region, keeping the relative separations fixed at their laboratory wavelengths and the flux ratio of [N II] λ6583 to [N II] λ6548 at the intrinsic ratio of 2.96. We then measure the [S II] $\lambda\lambda$6718,6732 doublet, Hβ and the [O III] $\lambda\lambda$4959,5007 doublet, while fixing the model to Hα + [N II] linewidth and velocity.

We also test for the presence of a broad Hα component by refitting the Hα + [N II] region, allowing for an additional broad Gaussian in the Hα line with a FWHM of at least 500 $\mathrm{km\ s^{-1}}$. We consider the fit to be improved if the χ^2 decreases by 25%, but do not find any evidence of broad Hα for any galaxies within our sample.

2.3 Placing galaxies on the BPT diagram

The BPT diagram (Baldwin et al., 1981) is a powerful diagnostic for differentiating between the sources of ionizing radiation in a galaxy spectrum (Veilleux & Osterbrock, 1987; Kewley et al., 2001, 2006; Kauffmann et al., 2003b). While there are many variations on the original optical line ratio diagram and many classification schemes therein, we focus on the "traditional" BPT, which uses the ratios [N II]/Hα vs [O III]/Hβ.

In this space, star-forming galaxies which are dominated by emission from H II regions create the sequence marked by a dotted line in each panel of Figure 2.3 (the star-forming sequence; Kewley et al., 2013). Lower metallicities produce higher

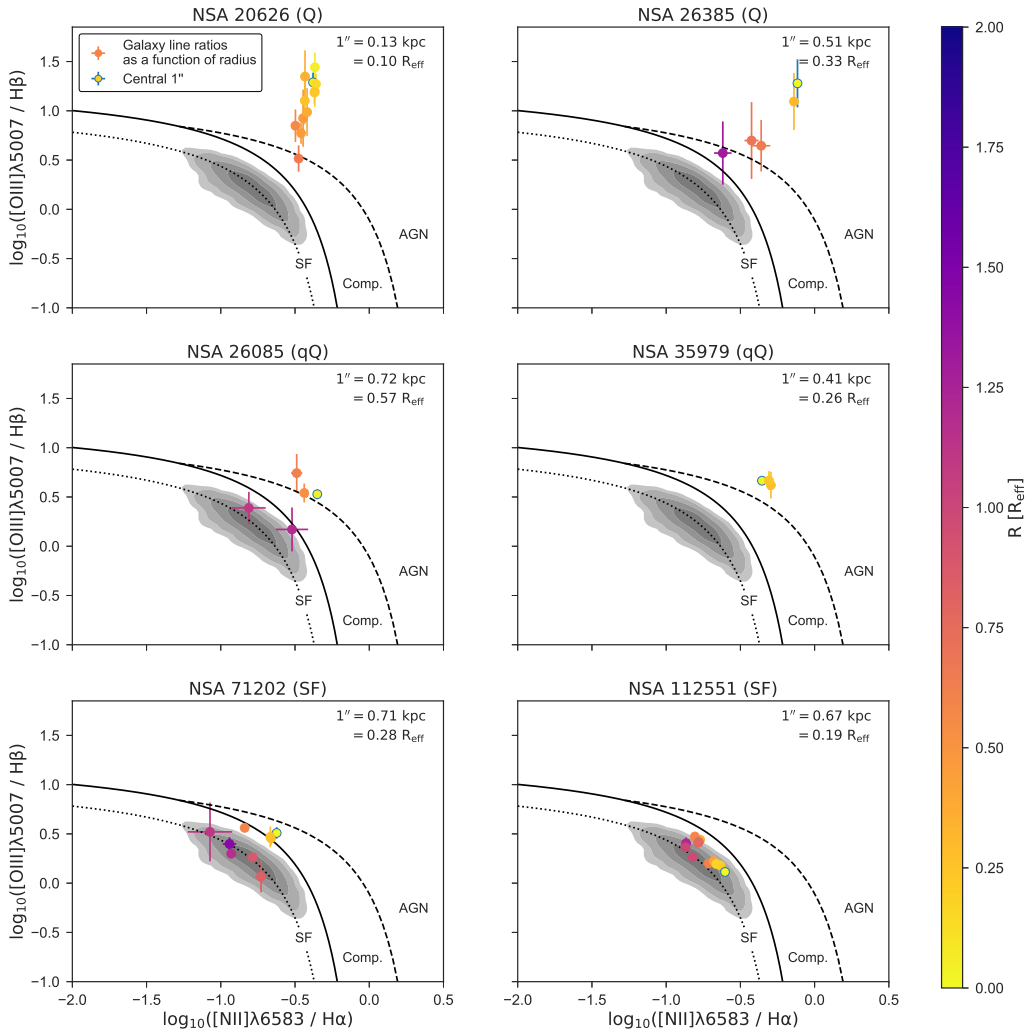

Fig. 2.3: A selection of BPT diagrams for 6 galaxies in our sample which highlight the observed spatial patterns within each galaxy subtype. Each panel shows the locus of low-mass isolated galaxies with well-measured BPT emission lines (Hα and Hβ SNR $>$ 3) from the NASA/Sloan Atlas (gray contours) as well as the demarcation lines between sources of ionizing radiation as given in Kewley et al. (2013), where the dotted line traces the median H II abundance sequence, the solid line is the empirical delineation between star formation and AGN (Kauffmann et al., 2003b), and the dashed line is the maximum starburst line (Kewley et al., 2001). We show BPT measurements derived from the ESI spectra as circles, color-coded by distance from the galaxy center. Points are outlined in blue when they lie within the central arcsec of the galaxy. Galaxies fall into three broad categories: dominated by star formation (bottom row), central AGN with extended SF (top right, middle right), and pure AGN (top left). 16 / 20 galaxies defined as quiescent based on their D_n4000 and Hα EWs show signatures of AGN, along with 2 of 7 star-forming galaxies.

[O III]/Hβ ratios and lower [N II]/Hα ratios (Kewley et al., 2006; Groves et al., 2006; Cann et al., 2019).

We follow the commonly-used classification scheme for distinguishing between sources of ionizing radiation (star formation vs. AGN, shocks, or pAGB stars; e.g., Kewley et al., 2006, 2013; Reines et al., 2013; Baldassare et al., 2018). The dashed line in Figure 2.3 from Kewley et al. (2001) represents the division between a theoretical maximum-starburst model vs. emission that requires a harder ionizing spectrum (e.g., AGN activity). The Kauffmann et al. (2003b) division (solid line in Figure 2.3) is an empirical separation between the star-forming sequence and the AGN plume, which extends to larger [N II]/Hα and [O III]/Hβ ratios. Galaxies below the Kauffmann et al. (2003b) demarcation are considered to be purely star-forming, while galaxies above the Kewley et al. (2001) are traditionally considered to be Seyfert AGN and LINERs. Galaxies lying between these two regions are considered to be composites, whose spectra suggest a mix of ionization from star formation and harder radiation.

The BPT diagram is primarily used for identifying AGN activity in galaxies, as the harder ionizing radiation from an actively accreting supermassive black hole produces line ratios distinct from those found in a star-forming galaxies. However, there are several other astrophysical process that can produce line ratios similar to those from AGN. In general, BPT line ratios alone are insufficient to rule out other ionization mechanisms, like SNe shocks or heating from pAGB stars (Yan & Blanton, 2012; Yan, 2018).

2.3.1 Comparison with SDSS

We first compare the SDSS 3″-fiber flux ratios to those measured from our ESI spectra. We only evaluate the SDSS BPT diagram for a galaxy where the flux measurements

have sufficient SNR in the four key lines (Hα, Hβ, [O III], and [N II] SNR > 3). Of the 27 galaxies in our sample, only 12 have reliably measured BPT flux ratios in SDSS.

For each of the 12 galaxies, we extract a 3″ diameter spectrum from across the ESI slit, centered on the peak of the stellar continuum. The ESI extraction is matched to SDSS in diameter but not area (due to the mismatch of fiber vs. long slit). Still, for all 12 galaxies, we confirm the SDSS BPT classifications within R = 3″ centered on the peak of the stellar continuum in our ESI data, although we show in subsection 2.3.2 that this varies with smaller apertures.

2.3.2 Spatially-resolved BPT diagrams

The Keck/ESI spectrograph provides up to 20″ of spatial information on each galaxy in our sample, with $\sim 1''$ resolution. In Figure 2.3, we present spatially-resolved BPT diagrams for a subset of galaxies in our sample (BPT diagrams for the full sample are shown in Figures 2.7, 2.8, and 2.9).

The galaxies in our sample were originally classified as star-forming (7/27), quiescent (10/27), or quasi-quiescent (10/27) based on the SDSS-fiber measurements of their stellar populations (Hα EW and D_n4000, as shown in Figure 2.1).

In the 7 galaxies defined as star-forming, the emission lines extend across the full 20″ slit (e.g., NSA 112551, bottom row in Figure 2.2). All seven galaxies are classified as BPT-SF (emission originating from H II regions) from the 3″ spectra, but two of seven galaxies have composite line ratios within the central 1″, suggesting contribution to the emission from a non-SF-driven source of hard ionizing radiation. For the remaining five galaxies, the line ratios at all radii are consistent with ionizing radiation originating exclusively from star formation .

Though all seven star-forming galaxies are broadly classified as BPT-SF at (almost) all radii, the distribution of the emission line ratios within BPT-SF space as a function of radius varies from galaxy to galaxy. For three of the seven galaxies the line ratios at all radii are loosely clustered, with no clear radial trends.

In contrast, three galaxies show large radial variations in [N II]/Hα (e.g., NSA 112551 in Figure 2.3). In two cases, the [N II]/Hα ratio is greater at the center of the galaxy and decreases at larger radii, while the third galaxy (NSA 84573, see **??**) has [N II]/Hα ratios that increase with radius, while still remaining within the SF region. For all three galaxies, [O III]/Hβ is approximately constant as a function of radius. The galaxies not included in Figure 2.3 are shown in **??**.

Before examining the radial trends for quiescent and quasi-quiescent galaxies, we model the effects of key stellar population parameters on BPT-position, to better disentangle the behavior of underlying galaxy properties from any possible AGN contributions. The quiescent and quasi-quiescent galaxies will be discussed below in subsection 2.3.3.

2.3.3 Modelling BPT-behavior with simple stellar populations

To better understand how galaxies move through BPT-space, we investigate the effects of varying the stellar age, metallicity, and contribution from AGN to the emission line spectra for a set of simple stellar populations. We use FSPS (Conroy et al., 2009; Conroy & Gunn, 2010) to generate spectra for simple stellar populations, varying both stellar age and metallicity (solid lines in Figure 2.4, upper panel). We assume a Kroupa (2001) IMF and set the gas-phase metallicity to match the stellar, with a fixed gas ionization parameter of $\log(\mathrm{U}) = -2.0$. Nebular emission lines are generated for a given SSP as described in Byler et al. (2017).

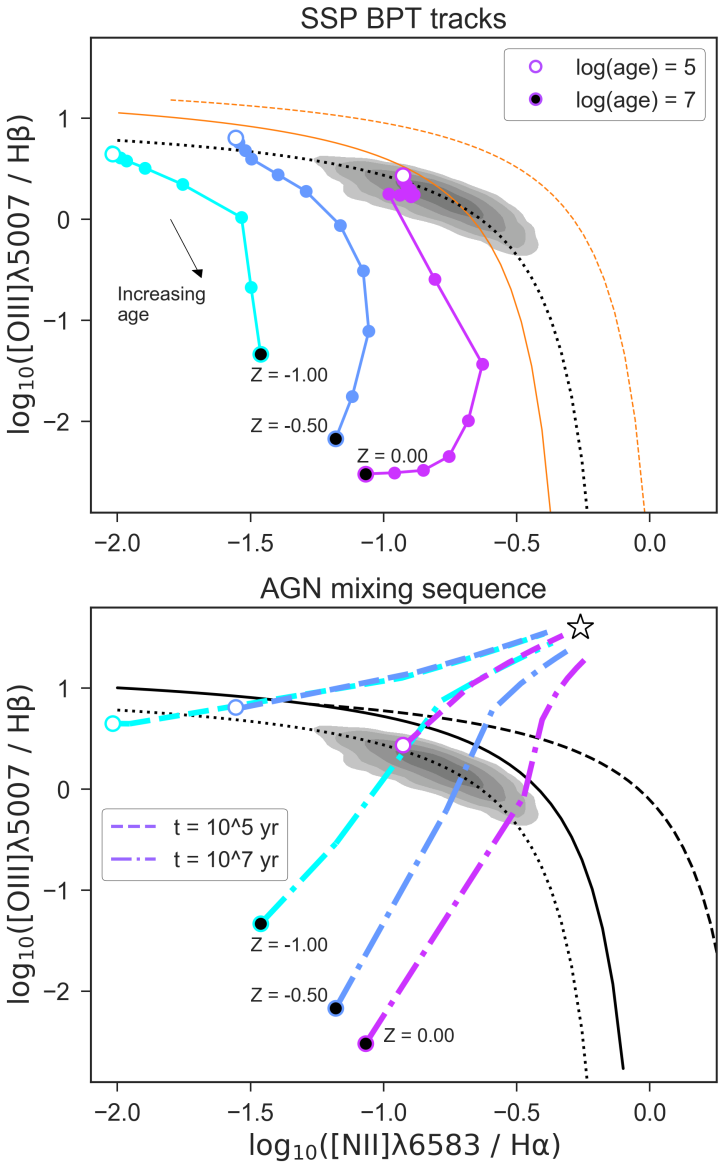

Fig. 2.4: *Upper panel:* The evolution of simple stellar populations in BPT-space as a function of stellar age (solid lines) and metallicity (blue-purple). Increasing metallicity moves galaxies to larger [N II]/Hα, while older stellar populations have lower [O III]/Hβ. The orange lines show the effect of increasing the ionization parameter (solid) and electron density (dashed) on the star-forming locus (adapted from Kewley et al., 2013)
Lower panel: The effect of adding Seyfert AGN-like emission to a simple stellar population. Dot-dashed lines show the effect of increasing AGN contribution at fixed age and metallicity for the underlying stellar population. The AGN fraction increases from 0 to 90% towards the upper right. The white star marks our fiducial AGN ratios.

Actively star-forming galaxies (those with the youngest stellar ages, white-faced circles in Figure 2.4) lie along the median H II abundance sequence. Increasing metallicity moves the spectrum to larger [N II]/Hα at nearly constant [O III]/Hβ.

The distribution of our simple stellar populations through BPT-space suggest that metallicity gradients as a function of radius can explain the horizontal sequences observed in some of the star-forming galaxies. Some cosmological zoom-in simulations predict that potential fluctuations from stellar feedback in low-mass galaxies can drive negative metallicity gradients ($\Delta \log \mathrm{Z/Z_{M_\odot}} \sim -0.25$, El-Badry et al., 2016), which are echoed by MaNGA observations that have found flat to slightly negative metallicity gradients in low-mass galaxies (Belfiore et al., 2017).

We also model the AGN narrow line spectrum as a set of Gaussian emission lines. Metallicity, gas density, and ionization parameter can all influence the narrow line region and the resulting BPT diagram position. We select our underlying AGN line ratios such that the "AGN" lies in the Seyfert region of the BPT diagram, while the Hα and Hβ fluxes are scaled to 10-100% of the SF fluxes. The location of an AGN on the BPT diagram also depends on the black hole mass and Eddington ratio, which can lead to AGN lying in the star-forming region of BPT space in some extreme cases (Cann et al., 2019). Given our observations of Seyfert-like line ratios in many of our galaxies, we use Seyfert-like ratios in our model.

Increasing the flux contribution from the AGN relative to the star formation produces the curved diagonal tracks shown in Figure 2.4 (lower panel, dashed and dot-dashed lines). The curvature of these tracks varies with both the metallicity and time elapsed since star formation , as well as the fundamental line ratios of the AGN. We show how the emission line ratios evolve with increasing AGN fraction for a Seyfert AGN (Figure 2.4, bottom panel). While this is a toy model, it suggests that variation in the contribution from an AGN produces diagonal sequences which are distinct from the horizontal sequences driven by metallicity gradients.

In the upper panel of Figure 2.4 we also show the effect of increasing the ionization parameter (solid orange line) or the electron density (dashed orange line) on the star-forming abundance sequence (dotted black line), adapted from Figure 2 of Kewley et al. (2013). Increasing the electron density can move star-forming galaxies into the composite region, while a larger ionization parameter can variously decrease [N II]/Hα or increase [O III]/Hβ depending on location along the star-forming sequence.

Of the 10 quasi-quiescent galaxies (green triangles, Figure 2.1), 6/10 have evidence for some on-going star formation within the slit. However, only one of these 6 galaxies is purely star-forming in BPT-space; the 5 other galaxies show evidence of emission originating from a non-SF-ing source within ~ 0.5 $R_{\rm eff}$ (e.g., NSA 26085, center-left in Figure 2.3). In all 4 of the remaining quasi-quiescent galaxies, we only observe emission which is consistent with a non-SF source of ionizing radiation (e.g., NSA 35979, center-right in Figure 2.3).

Finally, our sample includes 10 quiescent galaxies (purple circles in Figure 2.1). Of those 10, we find two galaxies (NSA 3478 and 18953) to be fully quiescent systems, with no detected emission at any radii. Of the 8 remaining galaxies for which we can measure the BPT line ratios, only one galaxy (NSA 119887) shows emission consistent with star formation . Visual inspection of the galaxy in SDSS gri shows a possible off-center H II region. Given the small spatial extent and weakness of the Hα flux from the star-forming region relative to central non-SF source, we still consider this galaxy to be pre-dominantly quiescent.

The 7 other quiescent galaxies exclusively inhabit the composite and AGN-like regions of the BPT diagram, with no evidence of purely star-forming line ratios at any radii.

In 12 of 15 quiescent and quasi-quiescent galaxies with non-SF line ratios, the AGN-like emission extends beyond the central 1″. In most cases, AGN-like or composite line ratios are observed out to $R \sim 0.5\ \mathrm{R_{eff}}$.

Of the galaxies which appear to host non-SF-like ionizing radiation, 8 / 18 show strong variation in their line ratios as a function of radius. In each of these cases, the galaxy moves diagonally through BPT-space, with both [N II]/Hα and [O III]/Hβ increasing towards the galaxy center (e.g., NSA 26385, top-right in Figure 2.3).

In the case of NSA 20626 (top-left, Figure 2.3), the emission line ratios create a nearly vertical sequence in BPT-space. Increasing the AGN contribution to the spectrum always changes both the [O III]/Hβ and [N II]/Hα, suggesting that the near-vertical sequence observed in NSA 20626 cannot be explained exclusively by variation in the ratio of star formation to AGN present in the galaxy. We note that NSA 20626 is an extreme case, being more nearby ($z = 0.006$) and larger in size ($\mathrm{R_{eff}} = 9.71''$) than other galaxies in the sample, allowing us to probe a much smaller region of the galaxy center at improved resolution. However, the remaining quiescent galaxies in our sample all lie within the same redshift range as the star-forming galaxies, confirming that the observed differences between the populations are not an effect of resolution.

To summarize, we have examined the radial behavior of galaxies on the BPT diagram and found that **the majority of quiescent and quasi-quiescent galaxies have extended AGN-like line ratios which form characteristic diagonal tracks across BPT-space**, which are distinct from the metallicity gradients observed in star-forming galaxies.

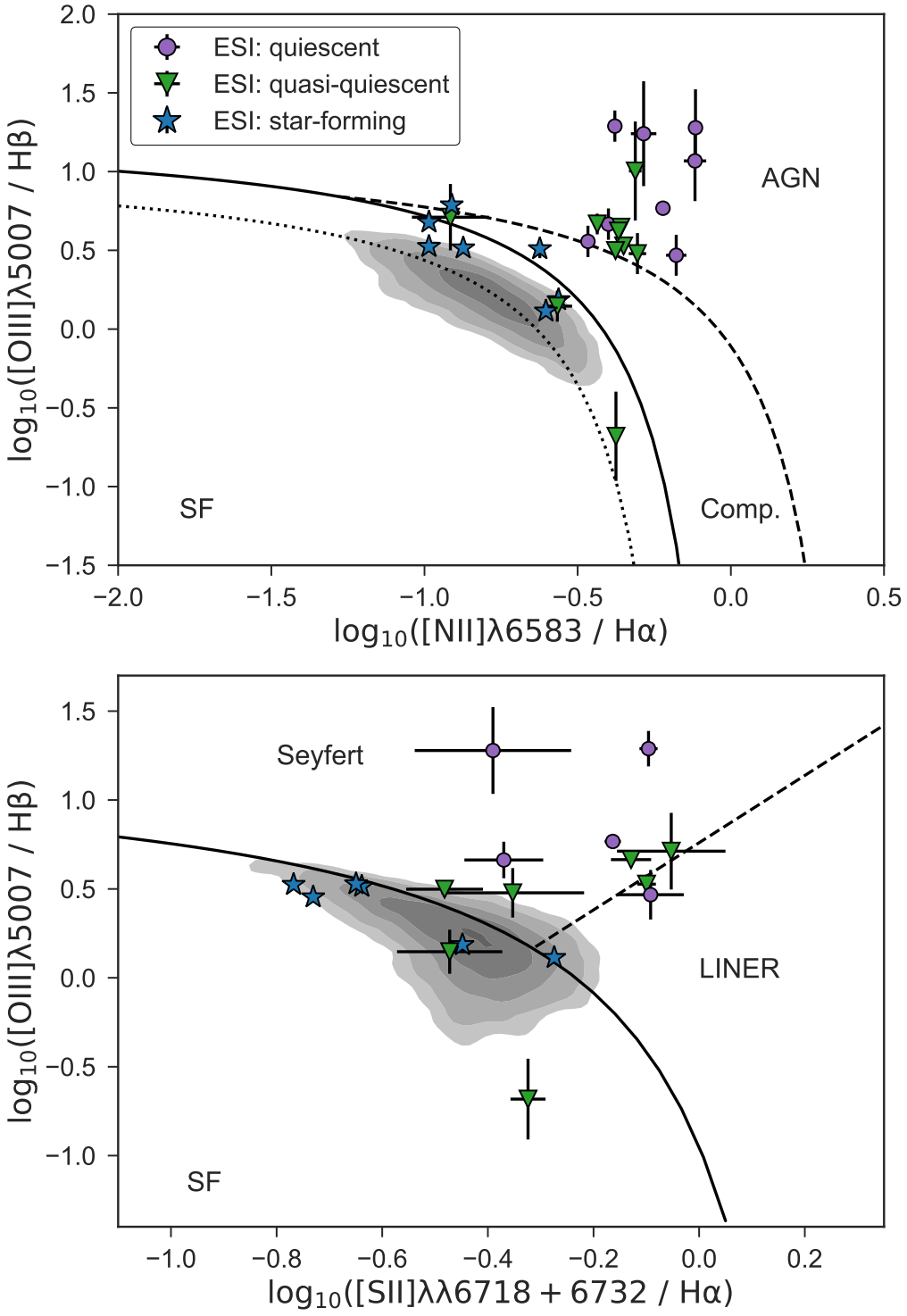

Fig. 2.5: *Upper panel:* The [N II]-BPT diagram for all galaxies in the sample, measured within the central 1″ of the Keck/ESI spectra. Galaxies classified as star-forming from their stellar populations in SDSS (blue stars) lie in the star-forming or composite regions of the BPT diagram. Quiescent and quasi-quiescent galaxies (circles and triangles) lie primarily in the AGN region of the diagram.
Lower panel: The [S II]-BPT diagram for a subset of galaxies within the sample, once again measured within the central 1″ of the Keck/ESI spectra. The [S II]-BPT diagram can be used to distinguish between Seyfert AGN and Low-Ionization Nuclear Emission Regions (LINERs), which may have more ambiguous origins.

2.3.4 The central 1″

Our investigation of the spatially-resolved BPT diagram for low-mass galaxies shows that the excitation contribution from non-SF sources can vary significantly as a function of radius, but always peaks within the central arcsecond of each galaxy. A possible explanation for this behavior is that we are observing the increasing influence of AGN activity within each galaxy's narrow line region (NLR).

To better quantify the influence of the harder ionizing radiation present within our sample of galaxies, we focus on only the central 1″ of each galaxy, where emission from an AGN, if present, should dominate. Based on the BPT classifications of Kewley et al. (2006), we classify the central 1″ as quiescent, AGN-like, or star-forming (Table 1, BPT type). The BPT diagram traditionally distinguishes between the "AGN" and "composite" regions, where composite refers to a mix of star formation and AGN-driven ionization, but this is a empirical divide, calibrated to high-mass galaxies.

BPT line ratios are not an un-biased tracer of AGN activity, as the presence of even small amounts of star formation can "dilute" AGN-like line ratios (Trump et al., 2015). Recent work suggests that the underlying ionizing spectrum for of intermediate mass black holes may never produce line ratios in the composite or AGN regions (Cann et al., 2019). We note that the star-forming galaxy sample extends to lower stellar masses than the quiescent one, potentially heightening this effect. Therefore, we cannot rule out the presence of hidden AGN in the star-forming galaxies.

Figure 2.5 shows the position of each galaxy's central 1″ on the [N II] and [S II] BPT diagrams (upper and lower panels, respectively). Star-forming galaxies lie near the H II sequence (dotted line, upper panel). The small number of star-forming galaxies with AGN-like line ratios all lie very close to or within the composite region,

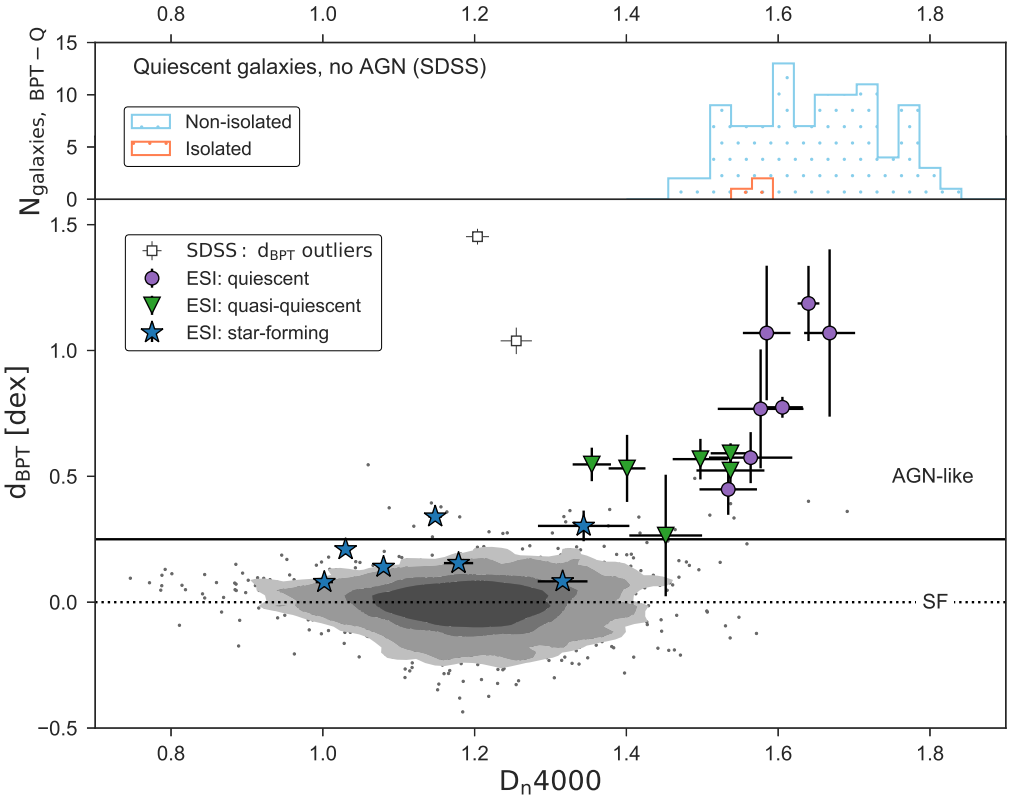

Fig. 2.6: *Lower panel*: $\mathrm{d_{BPT}}$ as a function of $\mathrm{D_n4000}$ for isolated, low-mass galaxies in SDSS (gray) and galaxies observed with ESI (colors). The $\mathrm{D_n4000}$ index measures the strength of the Balmer break and is a good proxy for stellar age, with large values of $\mathrm{D_n4000}$ indicating an evolved stellar population. Large BPT distances indicate stronger ionizing radiation signatures, while $\mathrm{d_{BPT}} = 0$ indicates a galaxy is on the median star-forming sequence. We find that the BPT-position of the central 1″ in a galaxy is tightly correlated with the age of the galaxy. White squares mark two outliers from SDSS with large $\mathrm{d_{BPT}}$ measurements but low $\mathrm{D_n4000}$. The lack of low-$\mathrm{d_{BPT}}$ objects at high $\mathrm{D_n4000}$ suggests that the quiescent galaxies lack even the low level star-formation seen in the quasi-quiescent galaxies.
Upper panel: The number of BPT-quiescent galaxies as a function of $\mathrm{D_n4000}$ in isolated (orange) and non-isolated (blue) environments. The presence of BPT-Q satellite galaxies in the same mass range indicates that we are not missing a hidden population of BPT-Q isolated galaxies.

suggesting low-metallicity gas (Groves et al., 2006), a significant contribution from star formation in the central 1″, or both.

In SDSS, galaxies not classified as star-forming are primarily found in the composite region, where we expect to see galaxies with a mix of star formation and AGN emission. Within the ESI central 1″, almost none of the quiescent and quasi-quiescent galaxies lie in this composite region, suggesting that either there is no underlying star formation at the smallest radii or that we are probing the region where the harder ionizing radiation is strong enough to dominate over any residual star formation .

Additionally, we find that the majority of our AGN-like galaxies lie in the Seyfert region of the [N II] BPT diagram, making it less likely that the emission in these galaxies originates from pAGB stars, which are predominately LINER-like. Placement on the [O I] BPT diagram could further distinguish between shocks and AGN, but we are unable to recover [O III]-6300λ in our spectra.

The majority of the quiescent and quasi-quiescent galaxies in our sample lacked sufficient SNR for placement on the BPT diagram with SDSS. In 13 of the 15 galaxies which did not have SDSS BPT measurements, the increased spectral and spatial resolution of the Keck/ESI spectra reveals the presence of faint central emission consistent with AGN-like line ratios.

Of the 20 galaxies defined as quiescent or quasi-quiescent based on their stellar populations, we find that 16 show evidence of potentially hosting an actively accreting central black hole.

2.4 BPT distance and quiescence

Thus far, we have examined how our galaxies would be defined within the traditional BPT diagram. However, this classification scheme has been calibrated for galaxies more massive than our sample. Low-mass galaxies have weaker AGN emission relative to their high-mass counterparts, and their metal-poor nature can significantly influence their position on the BPT diagram, as metallicity is a significant driver of BPT-position for both star formation and AGN-dominated spectra, as we have shown in subsection 2.3.3. Due to these complicating factors, we find it useful to parameterize each galaxy's relative position on the BPT diagram. We use $\mathrm{d_{BPT}}$, the perpendicular distance from the Kewley et al. (2013) star-forming sequence (Figure 2.5, dotted line) as measured for the central 1″ ESI spectrum of each galaxy.

We compare $\mathrm{d_{BPT}}$ to $\mathrm{D_n4000}$, which measures the strength of the 4000 Å break and serves as a good proxy for the age of stellar populations. We use stellar age as traced by $\mathrm{D_n4000}$ rather than any proxy for star formation , as we cannot decouple Hα emission originating from H II regions vs. that from other sources. Our ESI spectra lack the required sensitivity in the bluest orders to measure $\mathrm{D_n4000}$, so we rely on the values derived from the 3″ SDSS fiber. Simulations predict moderate age gradients in low-mass galaxies ($\Delta \mathrm{t} \sim 1$ Gyr within 1 kpc; El-Badry et al., 2016). For quiescent galaxies, where we expect older overall ages, $\mathrm{D_n4000}$ does not vary significantly on Gyr timescales and should have similar values when measured within 1 vs 3″.

In Figure 2.6 we find a correlation between $\mathrm{d_{BPT}}$ and $\mathrm{D_n4000}$, with the oldest galaxies most removed from the BPT star-forming sequence. AGN found in star-forming galaxies are found significantly lower along the AGN mixing sequence relative to their quiescent galaxy counterparts.

For comparison, the gray contours in Figure 2.6 show the full sample of low-mass isolated galaxies, with $\mathrm{d_{BPT}}$ values calculated from the SDSS emission line fluxes. The majority of galaxies have $\mathrm{D_n4000} < 1.5$ and scatter about $\mathrm{d_{BPT}} = 0$. This is in direct contrast to quiescent and quasi-quiescent galaxies, where we see a clear relation between $\mathrm{d_{BPT}}$ and $\mathrm{D_n4000}$.

Though we attempted to randomly select galaxies from the star-forming population, all 7 galaxies lie above $\mathrm{d_{BPT}} = 0$ even within the 3″ fiber, an unfortunate byproduct of small sample size.

Two galaxies have SDSS-derived $\mathrm{D_n4000}$ values indicative of star formation , but significantly elevated $\mathrm{d_{BPT}}$ (white squares in Figure 2.6). Both galaxies have SDSS emission line ratios that place them in the LINER region of the BPT diagram. However, the galaxies lie well outside the range of typical BPT-LINER values. Given these un-physical values, we plan follow-up spectroscopic observations of these galaxies before further classifying.

Thus far, we have relied on the [N II] BPT diagram to disentangle emission from star formation vs non-H II-region sources. The most commonly invoked explanation for non-SF-driven emission is an actively accreting black hole, but this is not the only possible source for the observed line ratios. The AGN region of the BPT diagram is known to host two distinct populations: Seyfert AGNs and Low-Ionization Emission Regions (commonly referred to as LINERs when found in the nuclear regions of galaxies). The two populations cannot be distinguished in the composite or near-composite regions of the BPT diagram, though Seyfert galaxies tend to have lower [N II]/Hα and higher [O III]/Hβ than LINERs.

Shocked gas from outflows can produce AGN-like line ratios, but it is unclear if such low-mass galaxies are capable of producing sufficiently energetic episodes of star formation (Dashyan et al., 2018). Studies of ionization sources on the BPT diagram (e.g., Yan & Blanton, 2012; Belfiore et al., 2017) have found that

heating from pAGB stars can mimic a low-accretion-rate black hole and produce LINER-like emission. However, the majority of our AGN-candidates have central emission line ratios that are strongly characteristic of Seyfert AGN, rather than LINERs. Moreover, in the majority of cases, the Hα emission does not directly trace the stellar continuum, suggesting that an old stellar population is not the origin of the ionizing radiation.

2.5 Summary

In this work, we investigate the connection between AGN-like line ratios and quiescence in low-mass, isolated galaxies. We have acquired high-resolution, spatially-resolved spectroscopy for 27 isolated low-mass galaxies, and measured key optical emission lines as a function of radius. We are able to place 25 of 27 galaxies on the Baldwin Phillips Terlevich (BPT) diagram in a spatially-resolved manner. Within the central 1″ of each galaxy, we measure the galaxy's distance from the star-forming sequence in BPT-space ($\mathrm{d_{BPT}}$). We use this parameter as a measure of AGN activity within a galaxy. Our results are summarized as follows:

1. We qualitatively distinguish a variety of trends in the radial BPT diagram for galaxies in our sample. We find a significant number of quiescent galaxies have extended emission which forms distinct tracks in BPT-space, moving from the star-forming or composite regions at $\mathrm{R} \sim \mathrm{R_{eff}}$ to the AGN region in the galaxy center (Figure 2.3, as well as Appendix Figures **??**, **??**, and **??**).

2. We identify central non-SF ionizing radiation in 16 of 20 quiescent and quasi-quiescent galaxies (Figure 2.5).

3. We find that almost all isolated quiescent galaxies host AGN, in contrast to denser environments, where we find significant numbers of quiescent galaxies without AGN-like line ratios.

While we cannot confirm that AGN are actively quenching the galaxies in our sample, the ubiquity of AGN-like line ratios in low-mass quiescent galaxies adds to the growing body of evidence that AGN play a crucial role in self-quenching galaxies at all mass scales. Careful follow-up with both radio and X-ray facilities will be crucial for confirming the presence of AGN within these systems.

Additionally, constraining the ages of the quiescent and quasi-quiescent galaxies in our sample will help build up a coherent picture of the quenching process at play. In this work, we have used the 4000-Å break to trace the mean light-weighted age of stellar populations in galaxies. $\mathrm{D_n4000}$ is an effective method for identifying recent ($\sim 1-3$ Gyr) bursts of star formation, but becomes insensitive to older stellar ages (e.g., 7 vs 13 Gyr), particularly at low metallicities (Kauffmann et al., 2003a).

The measurement of spatially-resolved star formation histories for our sample of low-mass isolated galaxies will provide significant insight into the quenching process at work. Future work will explore the spatially-resolved SFHs as well as the kinematics of both the gas and stars as derived from our ESI observations in order to constrain the nature of AGN feedback within low-mass, isolated galaxies.

3

The quiescent fraction of isolated, low mass galaxies across simulations and observations

Claire Dickey, Tjitske Starkenburg, Marla Geha, Changhoon Hahn, Daniel Anglés-Alcázar, Ena Choi, Romeel Davé, Shy Genel, Karthiek Iyer, Ariyeh Maller, Nir Mandelker, Rachel Somerville, LY Aaron Yung, *The Astrophysical Journal*, **880**, 57 (2020)

ABSTRACT

We compare three major large-scale hydrodynamical galaxy simulations (EAGLE, Illustris-TNG, and SIMBA) by forward modeling simulated galaxies into observational space and computing the fraction of isolated and quiescent low mass galaxies as a function of stellar mass. Using SDSS as our observational template, we create mock surveys and synthetic spectroscopic and photometric observations of each simulation, adding realistic noise and observational limits. All three simulations show a decrease in the number of quiescent, isolated galaxies in the mass range $\mathrm{M}_* = 10^{9-10}\ \mathrm{M}_\odot$, in broad agreement with observations. However, even after accounting for observational and selection biases, none of the simulations reproduce the observed absence of quiescent field galaxies below $\mathrm{M}_* = 10^9\ \mathrm{M}_\odot$. We find that the low mass quiescent populations selected via synthetic observations have consistent quenching timescales, despite apparent variation in the late time star formation histories. The effect of increased numerical resolution is not uniform across simulations and cannot fully mitigate the differences between the simulations and the observations. The framework presented here demonstrates a path towards more robust and accurate comparisons between theoretical simulations and galaxy survey observations, while the quenching threshold serves as a sensitive probe of feedback implementations.

3.1 Introduction

The transition of galaxies from star-forming into quiescence provides key insights into the physical processes that drive galaxy evolution. Major extragalactic surveys like the Sloan Digital Sky Survey (SDSS, York et al., 2000) have been instrumental in quantifying the differing properties of galaxies in these two categories, including morphology, environment, and color (e.g., Blanton et al., 2003; Kauffmann et al., 2003b; Brinchmann et al., 2004; Blanton & Moustakas, 2009; Moustakas et al., 2013). The processes that drive a galaxy's transformation can be broadly divided into two categories: external processes which occur in high-density environments and processes internal to the galaxy which are often thought to be correlated to galaxy mass (e.g., Peng et al., 2010).

Understanding how and when feedback mechanisms operate within galaxies and in which regimes they are most effective remains a major focus of both observational and theoretical studies of galaxy evolution. Observational galaxy surveys have been used to characterize the populations of quiescent and star forming galaxies as a function of stellar mass (Kauffmann et al., 2004; Geha et al., 2012), environment (Wetzel et al., 2012), and redshift (Brammer et al., 2009); as well as key correlations between galaxy properties (e.g., the star forming sequence; Daddi et al., 2007; Noeske et al., 2007; Salim et al., 2007; Elbaz et al., 2007) which inform our understanding of the underlying forces that drive galaxy evolution.

Large-scale cosmological hydrodynamic galaxy formation simulations reproduce the observed universe in a qualitative manner (Genel et al., 2014; Vogelsberger et al., 2014; Schaye et al., 2015; Davé et al., 2017; Pillepich et al., 2018a; Davé et al., 2019). Each simulation uses a distinct set of approximations for the complex physics of underlying galaxy evolution, including star formation, heating and cooling of gas, black hole formation and growth, feedback from active galactic nuclei (AGN), and stellar feedback (for an overview see Somerville & Davé, 2015; Vogelsberger

et al., 2020). While it has been shown that many different subgrid models can produce relatively consistent pictures of galaxy evolution (Naab & Ostriker, 2017), the variations between simulations present a unique opportunity to explore how feedback mechanisms shape galaxy evolution.

Many studies have focused on comparing the simulated distributions of quantities such as galaxy masses, colors, or star-formation rates to observations (e.g., Genel et al., 2014; Torrey et al., 2014; Vogelsberger et al., 2014; Schaye et al., 2015; Somerville & Davé, 2015; Sparre et al., 2015; Davé et al., 2017; Pillepich et al., 2018a; Nelson et al., 2018; Trayford et al., 2017; Donnari et al., 2019, 2020a,b). These works primarily focus on comparing a singular simulation to a particular set of observations. Studies using multiple simulations require the careful construction of a consistent framework for inter-simulation comparison.

In the observed universe, the quiescent fraction for isolated galaxies is zero at $\mathrm{M}_* < 10^9\ \mathrm{M}_\odot$ (Geha et al., 2012) in the SDSS volume, suggesting that feedback in this mass regime is highly sensitive to stellar mass. Most studies of feedback in low mass galaxies have focused on environmental quenching, either in the context of high density environments such as clusters or interactions with a Milky Way-like host galaxy (e.g., Fillingham et al., 2018; Sales et al., 2015; Wetzel et al., 2013, 2015).

Internal feedback may influence galaxy evolution down to $\mathrm{M}_* \sim 10^9\ \mathrm{M}_\odot$, via either AGN (Dickey et al., 2019; Koudmani et al., 2019; Penny et al., 2018) or stellar feedback (El-Badry et al., 2016). However, the efficiency and interplay of different feedback mechanisms below this mass limit remains uncertain. Large-scale hydrodynamic simulations present a unique opportunity to create an "observed" magnitude limited galaxy survey and explore how different subgrid feedback implementations shape the distribution.

The IQ (Isolated & Quiescent) Collaboratory[1] aims to bridge the gap between simulations and observations of star-forming and quiescent galaxies to better characterize internal quenching processes. In Hahn et al. (2019, Paper I), we began the process of comparing the star forming sequence across a set of simulations.

Our initial analysis in Paper I highlighted the large variation in the apparent quiescent populations of each simulation, but we did not make a direct comparison between simulations and observations. In that work, the star formation rates from the simulations are obtained "directly" from the simulation output, as opposed to being derived from "observables" like Hα- or UV+IR-derived star formation rates, or indices such as the Hα equivalent width (EW) and $\mathrm{D_n}4000$, an index that measures the strength of the 4000Å break and loosely traces stellar age. Moreover, even within observational results, selecting different tracers for e.g., SFRs can give rise to significant variation (e.g., Salim et al., 2007; Kennicutt & Evans, 2012; Speagle et al., 2014; Flores Velázquez et al., 2020; Katsianis et al., 2020)

In addition to deriving galaxy observables from a simulation, fully transforming a simulated volume into a true observational analogue requires the careful creation of complete, volume-corrected samples. This is particularly challenging when we are trying to reproduce observations comparing star forming and quiescent populations, which often suffer from differing levels of incompleteness within the same survey.

Our goal in this work is to create an "apples-to-apples" comparison of the quiescent fraction of isolated low mass ($\mathrm{M_*} < 10^{10}\ \mathrm{M_\odot}$) galaxies as a function of stellar mass, using observations of the local universe and a set of simulations, all of which produce realistic cosmological volumes using distinct implementations of subgrid physics. We focus our study on a selection of three major cosmological hydrodynamic simulations (EAGLE, Illustris-TNG, and SIMBA) and compare them to the observed population of low mass quiescent galaxies in the Sloan Digital Sky Survey (SDSS).

[1] https://iqcollaboratory.github.io/

In section 3.2, we present the simulations used in this work and in section 3.3 we discuss the observations which serve as our point of comparison. In section 3.4, we create mock observations from each simulation, including synthetic spectra, realistic noise, and SDSS-like incompleteness. section 3.5 and section 3.6 compare the "observed" simulations to the distribution of low mass quiescent galaxies in SDSS. In section 3.7 we explore the star formation histories of quiescent galaxies in the simulations and we review our findings in section 3.8.

3.2 Galaxy Formation Simulations

In this work, we focus on three large-scale hydrodynamic cosmological simulations (EAGLE, Illustris-TNG, and SIMBA), which we will compare to observations. We provide brief descriptions of each simulation below.

3.2.1 EAGLE

The Virgo Consortium's Evolution and Assembly of GaLaxies and their Environment (EAGLE) project[2] (Schaye et al., 2015; Crain et al., 2015; McAlpine et al., 2016) has a volume of (100 Mpc)^3 (co-moving), with dark matter and baryonic particle masses of 9.6×10^6 $\mathrm{M}_\odot$ and 1.8×10^6 $\mathrm{M}_\odot$. The simulation uses ANARCHY (Dalla Vecchia, in prep.), a modified version of the Gadget3 N-body SPH code (Springel et al., 2001b; Springel, 2005; Schaller et al., 2015). The subgrid model for feedback from massive stars and AGN is based on thermal energy injection in the interstellar medium (Dalla Vecchia & Schaye, 2012). The subgrid parameters were calibrated to reproduce the $z = 0$ stellar mass function and galaxy sizes.

[2]https://icc.dur.ac.uk/Eagle/

Previous works that have reproduced observables and examined the quenched population of the EAGLE simulation include Schaye et al. (2015), Furlong et al. (2015), Trayford et al. (2015) and Trayford et al. (2017), and the galaxy–black hole relations are discussed in McAlpine et al. (2017, 2018); Bower et al. (2017); Habouzit et al. (2020). Trčka et al. (2020) show that mock spectral energy distributions (see Camps et al., 2018 for public release of the SEDs) based on EAGLE galaxies and radiative transfer calculations using `skirt` (Baes et al., 2011) are in overall agreement with observed galaxy spectra, and highlight the need for consistent comparisons between simulations and observations. Trayford et al. (2017) used the same results of the `skirt` radiative transfer code to determine quenched fractions based on mock UVJ colors, along with the distribution of Hα flux and $\mathrm{D_n}4000$. They found that the passive fraction varies significantly depending on the definition of quenched. We will compare our results to previous conclusions in §3.6.1.1.

3.2.2 Illustris-TNG

The Next Generation Illustris project (IllustrisTNG or TNG)[3] (Marinacci et al., 2018; Naiman et al., 2018; Nelson et al., 2018; Pillepich et al., 2018a; Springel et al., 2018) is the successor to the original Illustris project (Genel et al., 2014; Vogelsberger et al., 2014), with significant updates in the subgrid models and physics included in the simulation. We use the TNG100 simulation, which has a volume of (110.7 Mpc)^3, and dark matter and baryonic mass resolutions of 7.6×10^6 $\mathrm{M}_\odot$ and 1.4×10^6 $\mathrm{M}_\odot$. TNG is run using the AREPO moving-mesh code (Springel, 2010), which is based on the Gadget code (Springel et al., 2001b; Springel, 2005). Adjustments in the TNG model include the addition of magneto-hydrodynamics, updated stellar feedback prescriptions, and the transition from thermal "bubbles" in the IGM to a BH-driven

[3] https://www.tng-project.org/

kinetic wind for the low-accretion-rate black hole feedback mode (Pillepich et al., 2018b; Weinberger et al., 2017).

The color bimodality of low-redshift galaxies is shown to compare well to SDSS (Nelson et al., 2018). Other papers describe the size evolution of quiescent galaxies (Genel et al., 2018), and correlations between galaxy properties and super massive black holes and AGN feedback (Weinberger et al., 2018; Habouzit et al., 2019; Terrazas et al., 2020; Davies et al., 2020; Li et al., 2019; Habouzit et al., 2020). Donnari et al. (2019) show quenched fractions based on UVJ selection and the star forming sequence, and compare these to UVJ-selected observed quenched fractions from COSMOS/UltraVISTA (Muzzin et al., 2013). Donnari et al. (2020a) and Donnari et al. (2020b) explore the quenched fraction derived using star formation rates and distances from the galaxy star-forming sequence. Donnari et al. (2020a) in particular explores how systematic uncertainties effect a single set of observations, which we will further discuss in §3.6.1.2.

3.2.3 SIMBA

SIMBA (Davé et al., 2019) is a suite of cosmological simulations built on the `GIZMO` meshless finite mass hydrodynamics code (Hopkins, 2015, 2017), also based on the Gadget code (Springel et al., 2001b; Springel, 2005), and forms the next generation of the MUFASA (Davé et al., 2016) simulations with novel black hole growth and feedback sub-grid models. The fiducial run has a volume of $(143\ \mathrm{Mpc})^3$ and dark matter and baryonic mass resolutions of $9.6 \times 10^7\ \mathrm{M}_\odot$ and $1.8 \times 10^7\ \mathrm{M}_\odot$, respectively.

SIMBA includes a model for on-the-fly dust production and destruction (broadly following McKinnon et al., 2017), and star formation is regulated with two-phase kinetic outflows, which were tuned to predictions from the Feedback in Realistic

Environments (FIRE) simulations (Hopkins et al., 2014; Muratov et al., 2015; Anglés-Alcázar et al., 2017b; Hopkins et al., 2018). Black hole growth in SIMBA is based on the torque-limited accretion model (Hopkins & Quataert, 2011; Anglés-Alcázar et al., 2013, 2015, 2017a) linking the black hole accretion to properties of the galaxy's inner gas disk. The AGN feedback consists of kinetic bipolar outflows, modeled after observed outflows of AGN, and X-ray feedback input in the surrounding gas similar to Choi et al. (2012).

Previous work using SIMBA has already discussed the radial density profiles of quenched galaxies (Appleby et al., 2019), the weak correlation between galaxy mergers and quenching (Rodríguez Montero et al., 2019), and the connection between quenching and black hole growth (Davé et al., 2019; Thomas et al., 2019; Habouzit et al., 2020). We compare our results to relevant studies in §3.6.1.3.

3.3 Observations

Following Geha et al. (2012), we build our sample of observed galaxies from SDSS, using the NASA/Sloan Atlas (NSA; Blanton et al., 2011)[4], which includes all galaxies within $z < 0.055$ in the SDSS footprint. The NASA/Sloan Atlas is a re-reduction of SDSS DR8 (Aihara et al., 2011) optimized for nearby low-luminosity objects (Yan, 2011; Yan & Blanton, 2012), including an improved background subtraction technique (Blanton et al., 2011) and the addition of near and far UV photometry from *GALEX*. The catalog includes emission line fluxes and equivalent widths for all galaxies. We calculate stellar masses as in Mao et al. (2020), using the Bell et al. (2003) relation to determine mass-to-light ratio from the $g-r$ color. See subsection 3.5.3 for a more in-depth discussion on the effects of uncertainty in the stellar mass measurements on the resultant quiescent fraction.

[4]https://www.nsatlas.org

As in Geha et al. (2012), we consider a low mass galaxy to be quiescent if it has little-to-no star formation and is dominated by older stellar populations. For the first condition, we use the Hα equivalent width (EW), which traces recent (< 10 Myr) star formation, and require Hα EW < 2 Å. To probe galaxy age, we rely on $\mathrm{D_n4000}$ (Balogh et al., 1999), an index which quantifies the strength of the 4000Å break in the spectrum and traces the light-weighted age of the stellar population. The $\mathrm{D_n4000}$ index is an indirect measure of intermediate ($\sim$1 Gyr) star formation (Hamilton, 1985; Moustakas et al., 2006; Brinchmann et al., 2004). We use the empirical relation of Geha et al. (2012): $\mathrm{D_n4000} > 0.6 + 0.1 \log_{10}(\mathrm{M_*/M_\odot})$, to select galaxies with older stellar populations.

To quantify the environment of each low mass galaxy, we use $\mathrm{d_{host}}$, which is defined as the projected distance to the nearest massive neighbor ($\mathrm{M_*} > 2.5 \times 10^{10}$ $\mathrm{M_\odot}$; $\mathrm{M_{K_s}} < -23$; hereafter the host galaxy). We search for potential host galaxies within 7 Mpc and 1000 km/s of each low mass galaxy, using the Two Micron All Sky Survey (2MASS) Extended Source Catalog to ensure we do not miss any potential host galaxies that lie outside the SDSS imaging footprint. In the few cases where we do not identify a host within 7 Mpc, we use $\mathrm{d_{host}} =$ 7 Mpc.

We define galaxies as isolated when $\mathrm{d_{host}} > 1.5$ Mpc. This is an empirical choice based on the behavior of the quiescent fraction as a function of $\mathrm{d_{host}}$ (see Fig. 4 of Geha et al. (2012) or Figure 3.5 in this work). The quiescent fraction only shows a dependence on environment for $\mathrm{d_{host}} < 1.5$ Mpc, and so we consider low mass galaxies beyond this threshold to be isolated. Using a less strict definition (e.g., galaxies are isolated beyond $\mathrm{d_{host}} = 1$ Mpc) shifts the quenching threshold to a slightly lower mass, while a more conservative definition does not change the observed threshold. For galaxies with stellar masses above $\mathrm{M_*} = 10^{10}$ $\mathrm{M_\odot}$, we use the central – satellite designation from the group catalog of Tinker et al. (2011).

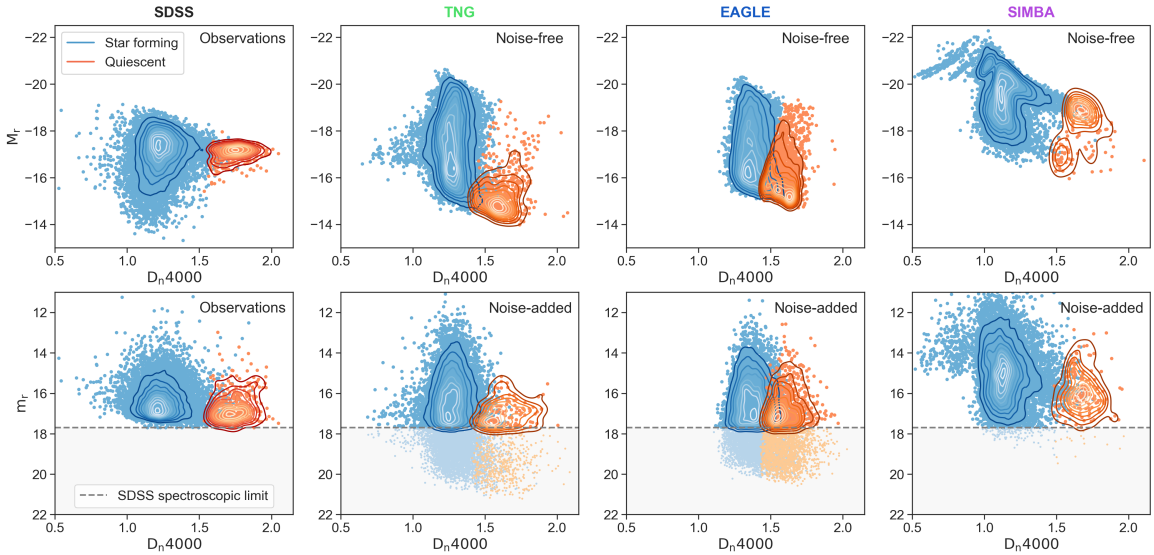

Fig. 3.1: ***Top row:*** The distribution of absolute r magnitude ($\mathrm{M_r}$) as a function of $\mathrm{D_n4000}$, from SDSS for observations and derived from the noise-less synthetic spectra from each simulation (from left to right: TNG, EAGLE, and SIMBA), for isolated galaxies (based on $\mathrm{d_{host}}$) in the stellar mass range $\mathrm{M_*} = 10^{8-10}\ \mathrm{M_\odot}$. Galaxies are color-coded as star forming (blue) or quiescent (orange) based on the noise-free Hα EW and $\mathrm{D_n4000}$. ***Bottom row:*** The distribution of apparent r magnitude ($\mathrm{m_r}$) as a function of $\mathrm{D_n4000}$, derived from the noise-added synthetic spectra along a single random sightline through each simulation box. Galaxies are color-coded as star forming (blue) or quiescent (orange) based on the noise-added Hα EW and $\mathrm{D_n4000}$. Galaxies below the gray dashed line fall below the SDSS spectroscopic limit and would not be selected for spectroscopic follow-up in SDSS. As such, they are not included in the calculation of f_q along a given sightline.

In the left column of Figure 3.1, we show the distribution of isolated galaxies observed in the local universe as a function of $\mathrm{D_n4000}$ and SDSS r magnitude in the mass range $\mathrm{M_*} = 10^{8-10}\ \mathrm{M_\odot}$. Galaxies in isolation are only observed to be quiescent above $\mathrm{M_*} = 10^{9}\ \mathrm{M_\odot}$, (Figure 3.2).

3.4 Mock Observations

To create a true apples-to-apples comparison between the observations and simulations, we must account for the effects of observational incompleteness, finite signal to noise, and a lack of precise distance information for individual galaxies in a wide-field survey.

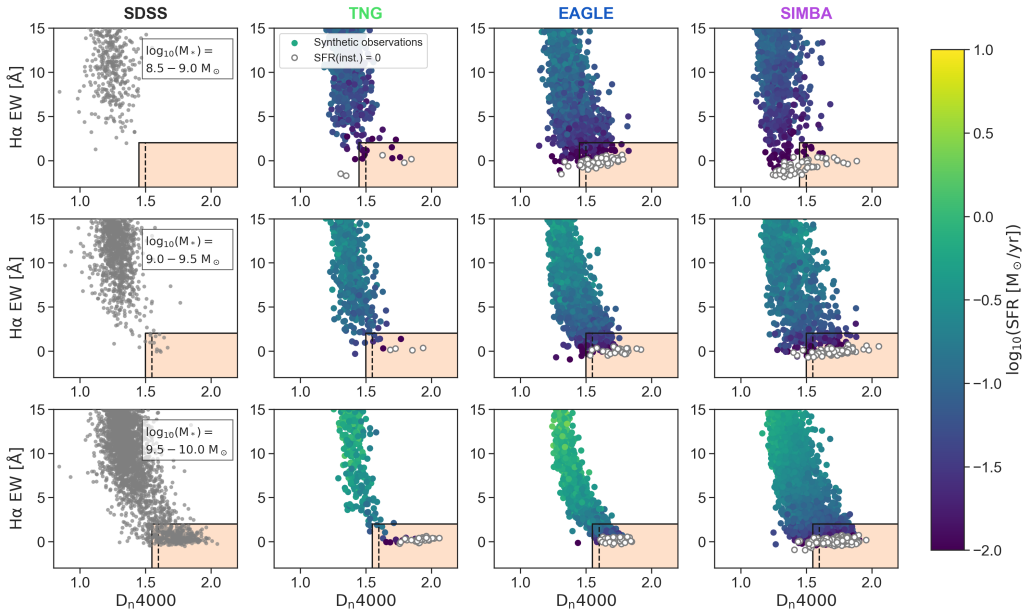

Fig. 3.2: D_n4000 vs. Hα EW, from SDSS for observations and derived from the noise-added synthetic spectra from each simulation (from left to right: TNG, EAGLE, and SIMBA), for isolated galaxies (based on d_{host}) in three stellar mass bins (from top to bottom: $M_* = 10^{8.5-9.0}$ $M_\odot$, $10^{9.0-9.5}$ $M_\odot$, and $10^{9.5-10.0}$ $M_\odot$). Galaxies are observed as quiescent if they fall into the orange region of D_n4000-Hα EW parameter space. The D_n4000 limit depends on stellar mass and is equal to the solid (dashed) vertical line at the low mass (high-mass) end of the bin for each row. For the simulations, galaxies are color-coded by their instantaneous star formation rates, and galaxies with SFR $= 0$ $M_\odot$/yr are shown in white.

To that end, we create mock surveys and synthetic observations of each simulation, adding realistic noise and observational limits. We use SDSS as our observational template. We select the mock observational limits and injected noise to match SDSS. We apply the same methodology to all the simulations, as described below for a single simulation box. However, this method can also be generalized and applied to semi-analytic models and zoom-in simulations, as well as adapted to match other surveys and observations.

3.4.1 Synthetic spectra

We begin by generating synthetic spectra for all galaxies in a given simulation using `FSPS` (Flexible Stellar Population Synthesis; Conroy et al., 2009; Conroy & Gunn, 2010, and the Python interface `python-fsps` Foreman-Mackey et al., 2014). Our method is described in full in Starkenburg et. al (in prep.), but in brief it is as follows.

For each galaxy, we bin the total stellar mass formed by formation age (t) and stellar metallicity (Z). We use a uniform t, Z grid across all the simulations to standardize the effects of otherwise variable time resolution and particle size. Age bin size increases linearly as a function of lookback time based on the minimum age steps of the underlying SSP models, from $t = 0$ to $t = 13.75$ Gyr. The metallicity grid spans $\log_{10}(\mathrm{Z}/\mathrm{Z}_{\odot}) = -2.2$ to 0.5 with $\Delta Z = 0.3$ at low metallicity, with bin resolution increasing to $\Delta Z = 0.1$ near $Z = 0$. We use a Chabrier (2003) IMF throughout, and include the AGB dust emission model of Villaume et al. (2015). To cover the most recent star formation and avoid resolution effects of stellar particles, we set the star formation rates younger than 15 Myr equal to the instantaneous star formation rate from the galaxy's gas particles with metallicity equal to the current mass-weighted metallicity of the star-forming gas.

We generate the spectrum of a simple stellar population at each point in the t, Z grid. The sum of the SPS spectra, weighted by the stellar mass formed, produces the galaxy spectrum. The nebular emission lines are calculated independently for each stellar metallicity bin using the FSPS nebular emission line prescription based on a CLOUDY lookup table (Byler et al., 2017), with the gas metallicity fixed to that of the metallicity bin.

Dust forms a crucial component to consider when building mock observables and when analyzing observational data, and different dust models can strongly affect results and conclusions. However, for lower-mass galaxies with relatively low gas masses and low metallicities, dust is expected to affect results less strongly. We therefore apply the well-known and often used two-component dust model from Charlot & Fall (2000), which consists of a dust screen with a power law dust attenuation curve with index $\Gamma = -0.7$ and a normalization of $\tau(5500\text{Å}) = 0.33$. Stars younger than 30 Myr are additionally attenuated following an identical power-law attenuation curve with $\tau(5500\text{Å}) = 1.0$. We discuss the effects of using different dust models in building mock spectra in Starkenburg et al. (in prep.).

Hahn et al. (in prep.) use approximate Bayesian computation to infer an empirical dust model using the same set of mock galaxy spectra by fitting SDSS r-band magnitudes, $g-r$ colors, and NUV-FUV colors. We have tested how results in the present work change when using the best-fit dust empirical model. While the Hα EW measurements can be significantly affected by changing the dust model, $\mathrm{D_n}4000$ is relatively unchanged, as the index is not strongly sensitive to dust attenuation.

Using the synthetic spectra, we generate SDSS *g* and *r* band magnitudes, as well as $\mathrm{D_n}4000$ and Hα EW for all galaxies (Figure 3.1, top row). These quantities are noise-free and derived from spectra which encompass the total stellar light of each galaxy.

3.4.2 Mock surveys

In generating synthetic photometric and spectroscopic quantities for each simulated galaxy, we are much closer to observational analogues for each simulation. However, the distribution of absolute magnitude and $\mathrm{D_n}4000$ shown in the top row of Figure 3.1 for each simulation are not directly comparable to the corresponding distribution in SDSS (upper left), as the simulations are unaffected by observational noise and each sample contains every galaxy in the simulation volume. To accurately match observations, we need to create mock surveys of each simulation box[5].

Our method for creating mock surveys is as follows:

1. Place an "observer" at a random location 10 Mpc outside the simulation volume. This distance is selected to match the lower distance limit on galaxies in the NSA catalog from SDSS.

2. Calculate apparent magnitudes, radial velocities, and projected distances for all galaxies as the observer would see them "on sky". For each galaxy, the radial velocity is the sum of the peculiar velocities along the observer's sightline and the recessional velocities given the distance between the galaxy and observer.

3. Convolve the synthetic spectra with the SDSS instrumental line spread profile (modeled as a Gaussian with $\sigma = 70$ km/s) and resample the spectra to match the SDSS wavelength resolution and coverage.

4. Add realistic spectral noise. The average signal to noise ratio (SNR) of SDSS spectra is dependent on galaxy color and apparent magnitude, and is also a function of wavelength. To reproduce the noise characteristics of SDSS, we bin galaxies from SDSS as a function of $g-r$ color and apparent r magnitude. In each bin, we randomly draw 50 spectra and calculate the average SNR at each

[5] `Orchard`, our package for creating mock surveys, can be accessed at https://github.com/IQcollaboratory/orchard

wavelength. In each mock observer's frame, noise is added to the synthetic spectra based on galaxy color, apparent magnitude and wavelength by drawing from a normal distribution $\sigma(\lambda,\ g-r,\ m_r)$ such that the SNR matches the SDSS model. For simulated galaxies which fall outside the populated regions of the SDSS color-magnitude diagram, we select the closest bin in color-magnitude space.

5. Calculate stellar masses from the $g-r$ colors, following the prescription of Mao et al. (2020). Notably, this can result in stellar mass estimates that appear lower than the resolution limits of the simulation.

6. Remeasure $\mathrm{D_n}4000$ and Hα EW from the noise-added and instrumentally-broadened spectra. Figure 3.2 shows the distribution of noise-added $\mathrm{D_n}4000$ and Hα EW for the simulations in three stellar mass bins, as compared to SDSS. We follow the definition of Balogh et al. (1999) for $\mathrm{D_n}4000$ measurements and Yan et al. (2006) for Hα EW measurements.

7. Remove "unobservable" galaxies from the sample. Spectroscopy was only acquired for galaxies in SDSS above the limiting magnitude $m_r = 17.7$. To accurately match SDSS, simulated galaxies which have apparent magnitudes fainter than 17.7 along a particular sightline must be removed from the sample.

In Figure 3.1, we show effects of adding realistic noise, velocity resolution, and completeness cuts to isolated, $\mathrm{M_*} < 10^{10}\ \mathrm{M_\odot}$ galaxies in each of the three simulations. The upper row shows absolute magnitude (M_r) and $\mathrm{D_n}4000$ calculated from the noise-free synthetic spectra, while the bottom row shows $\mathrm{D_n}4000$ measured from the noise-added spectra and the apparent magnitudes (m_r) as seen by the observer along a random sightline.

The gray region in each panel in the bottom row of Figure 3.1 represents the regime in which galaxies are too faint to be selected for spectroscopic follow up

with SDSS. Of the three simulations, SIMBA produces the fewest "unobservable" galaxies. This is likely driven by the fact the SIMBA does not resolve galaxies all the way down to $M_* = 10^8$ $M_\odot$, leading to fewer faint galaxies which are then preferentially removed from the observed sample (see subsection 3.5.2 for a more detailed discussion on the effects of resolution in each simulation). TNG has the faintest population of quiescent galaxies in absolute magnitude (at least in part because it extends to the lowest stellar masses) and correspondingly fewer quiescent galaxies from this simulation are observable with an SDSS-like survey.

In Figure 3.2, we show the distribution of D_n4000 and Hα EW in three stellar mass bins for the observations and for the simulations as measured from the noise-added spectra. We color-code the simulations by instantaneous SFR, highlighting the need for synthetic observations to select the analogous quiescent population from simulations. As shown in Geha et al. (2012), no quiescent galaxies are observed in the SDSS volume below $M_* = 10^9$ $M_\odot$.

3.4.3 Isolation criteria

As in the observations, we select galaxies as isolated based on d_{host}, the projected distance between each simulated galaxy and its most nearby massive neighbor. As in the observations, for each galaxy we identify potential hosts (galaxies with ($M_* > 2.5 \times 10^{10}$ $M_\odot$), within 7 Mpc in projected distance and 1000 km/s in radial velocity). For galaxies with $M_* > 2.5 \times 10^{10}$ $M_\odot$, we also require potential hosts to be more massive than the galaxy. Galaxies which have no potential hosts within 1.5 Mpc ($d_{host} > 1.5$ Mpc) are considered to be isolated.

In Figure 3.3 we compare our isolation criteria to the central/satellite classification from the simulations themselves. For all three simulation that classification is based on a halo finder algorithm that uses the underlying dark matter structure (not available in observations nor in our mock observations). The specific

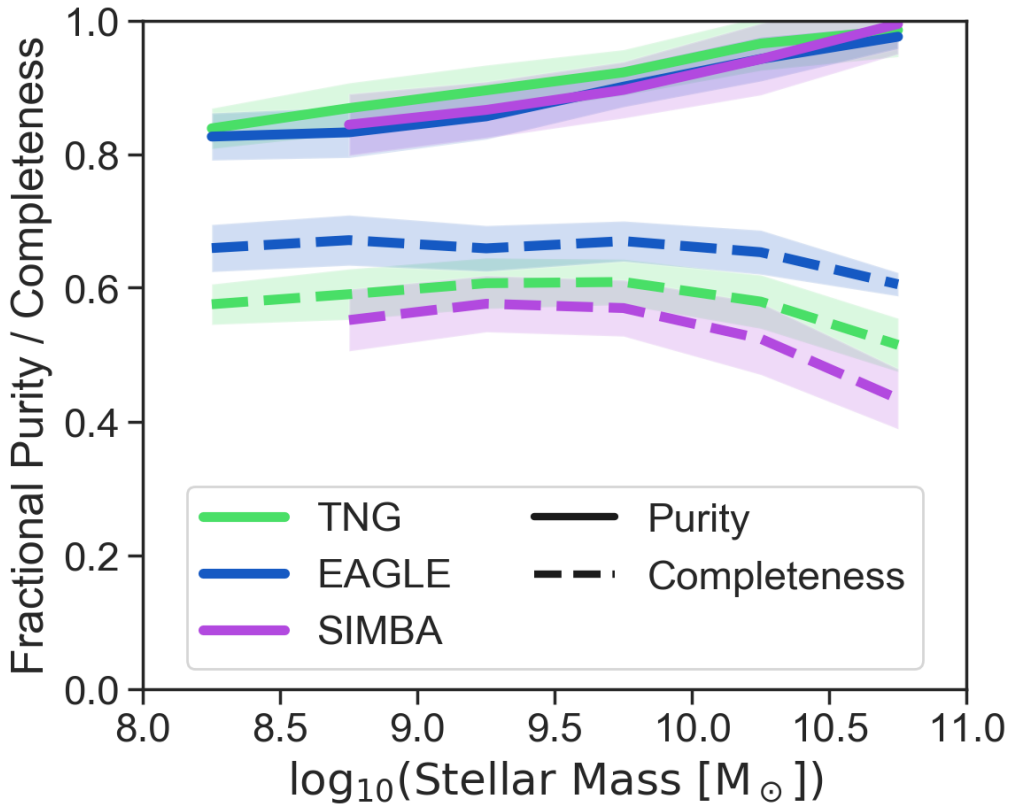

Fig. 3.3: The purity (the fraction of galaxies selected as isolated by the $\mathrm{d_{host}}$ criterion which are centrals, solid lines) and completeness (the fraction of the population of centrals which appear as isolated when using $\mathrm{d_{host}}$, dashed lines) of the $\mathrm{d_{host}}$ isolation criteria compared to the central/satellite classification from the simulations themselves. Shaded regions represent the one-sigma variation across 10 randomly oriented sightlines. Using the $\mathrm{d_{host}}$ criterion selects a sample of galaxies that is relatively pure (> 85 % of isolated galaxies are centrals) but somewhat incomplete (only $55 - 70$ % of centrals are selected as isolated). We use the true simulation-based stellar masses in this figure to provide maximum clarity on the purity and completeness of the $\mathrm{d_{host}}$ criterion.

algorithm varies between EAGLE/TNG, and SIMBA. To define halos, both EAGLE and TNG use `SUBFIND` (Springel et al., 2001a) to find overdense, gravitationally bound, (sub)structures within a larger connected structure that is found through a friends-of-friends (FOF; Davis et al., 1985) group-size halo finder. In SIMBA,galaxies are identified as FOF groups of stars and star forming gas with spatial linking length of 0.0056 times the mean interparticle spacing, while halos are identified as FOF groups with linking length of 0.2 times the mean interparticle spacing. Galaxies and haloes are cross-matched in post-processing using the `yt`-based package `CAESAR`.

For all three simulations the most massive subhalo (TNG and EAGLE) or galaxy (SIMBA) in a larger group halo is then classified as the central galaxy, while all other subhalos are classified as satellites.

For each simulation, we show the purity (the fraction of galaxies selected as isolated by the $\mathrm{d_{host}}$ criterion which are centrals, solid lines) and completeness (the fraction of the population of centrals which appear as isolated when using $\mathrm{d_{host}}$, dashed lines) as a function of mass. For all simulations, purity declines with decreasing stellar mass, though all samples remain relatively pure even at low stellar mass. At $\mathrm{M_*} = 10^9\ \mathrm{M_\odot}$, a sample of isolated galaxies selected with $\mathrm{d_{host}}$ will be ~ 85 % centrals (~ 15 % of the "observed" isolated sample of galaxies are actually satellites as defined by the halo finder).

Completeness is not strongly dependent on stellar mass below $\mathrm{M_*} = 10^{10}\ \mathrm{M_\odot}$, but decreases above this threshold. Completeness varies more between simulations, possibly due in part to the use of different halo finders. At $\mathrm{M_*} = 10^9\ \mathrm{M_\odot}$, $55 - 70$ % of the centrals selected by the halo finder will be observed as isolated, reflecting the more restrictive nature of the $\mathrm{d_{host}}$ criterion. Recreating the observational selection criteria for isolation is a critical step in comparing between the population of isolated, quiescent galaxies selected from observations and those generated in simulations (see also Figure 3.6 and the discussion at the end of subsection 3.5.1).

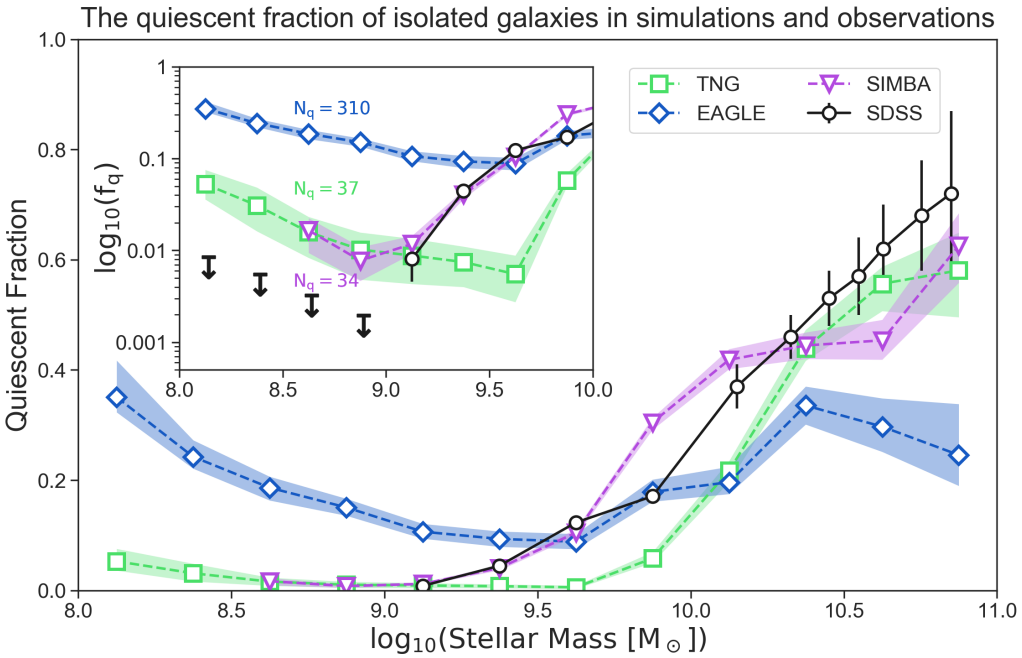

Fig. 3.4: The median quiescent fractions of isolated galaxies as a function of stellar mass for SDSS (black circles), Illustris-TNG (green squares), EAGLE (blue diamonds), and SIMBA (purple triangles). The quiescent fractions for the simulations are the medians of 25 randomly placed sightlines around each simulation box. Shaded regions represent the combination of binomial uncertainty on the quiescent fraction and the variance across sightlines for each simulation. Errorbars on the SDSS quiescent fraction are adapted from Geha et al. (2012). ***Inset:*** The same data shown in log-scale. Black arrows represent one-sigma upper limits for the SDSS data in bins where the number of isolated, quiescent galaxies is zero, and the number of isolated, quiescent galaxies (N_q) in the lowest mass bin is indicated for each simulation.

3.4.4 Quenching criteria

As in the observations, simulated galaxies are considered to be quiescent if $\mathrm{H}\alpha$ EW < 2 Å and $\mathrm{D_n}4000 > 0.6 + 0.1\log_{10}(\mathrm{M_*/M_\odot})$ (orange shaded region in Figure 3.2). Because $\mathrm{D_n}4000$ probes luminosity-weighted stellar age of a galaxy, it is difficult to make a corresponding selection in SFR space, as highlighted by the color-coding of galaxies in Figure 3.2.

The star forming and quiescent contours shown in Figure 3.1 can overlap because the $\mathrm{D_n}4000$ criterion is mass-dependent for each galaxy. Measuring $\mathrm{D_n}4000$ from the realistically-noisy synthetic spectra is crucial to accurately match the sample selection from observations.

3.4.5 Volume correction

To calculate the quiescent fraction f_q, we weight each galaxy by the inverse of the total survey volume over which it could be observed given the SDSS spectroscopic magnitude limit $(1/\mathrm{V_{max}})$.

The quiescent fraction of isolated galaxies is then

$$f_\mathrm{q} = \frac{\sum_{i=1}^{N_\mathrm{q}} 1/V_{\mathrm{max},i}}{\sum_{i=1}^{N_\mathrm{q}+N_\mathrm{SF}} 1/V_{\mathrm{max},i}}, \tag{3.1}$$

where $\mathrm{N_q}$ and $\mathrm{N_{SF}}$ are the number of quiescent and star forming galaxies in isolation in each mass bin, respectively.

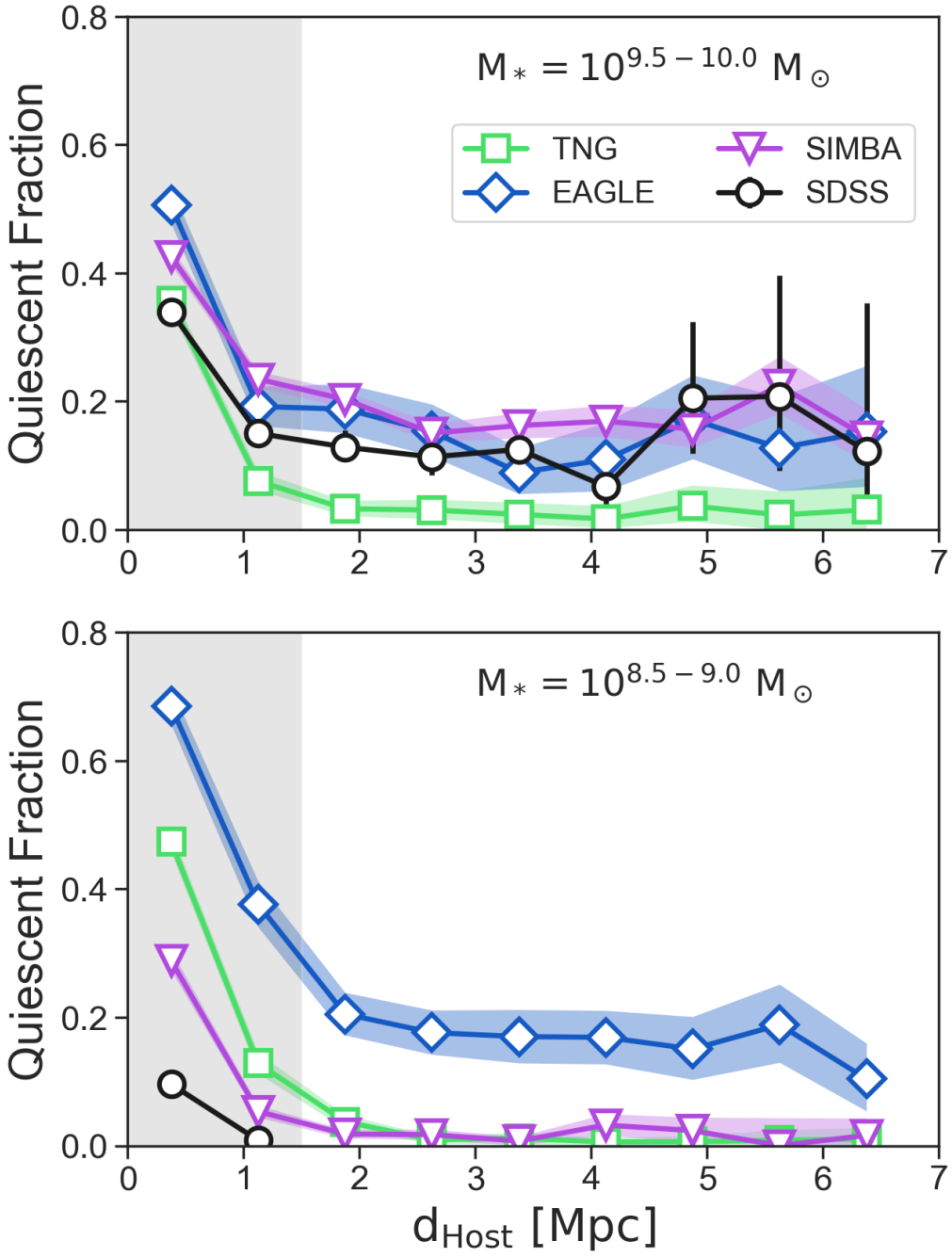

Fig. 3.5: The quiescent fraction of galaxies as function of d_{host} in two mass bins. The upper panel shows the observed distribution of galaxies with $M_* = 10^{9.5-10.0}\ M_\odot$, and the lower panel shows $M_* = 10^{8.5-9.0}\ M_\odot$. The gray region indicates $d_{host} < 1.5$ Mpc, corresponding to non-isolated galaxies.

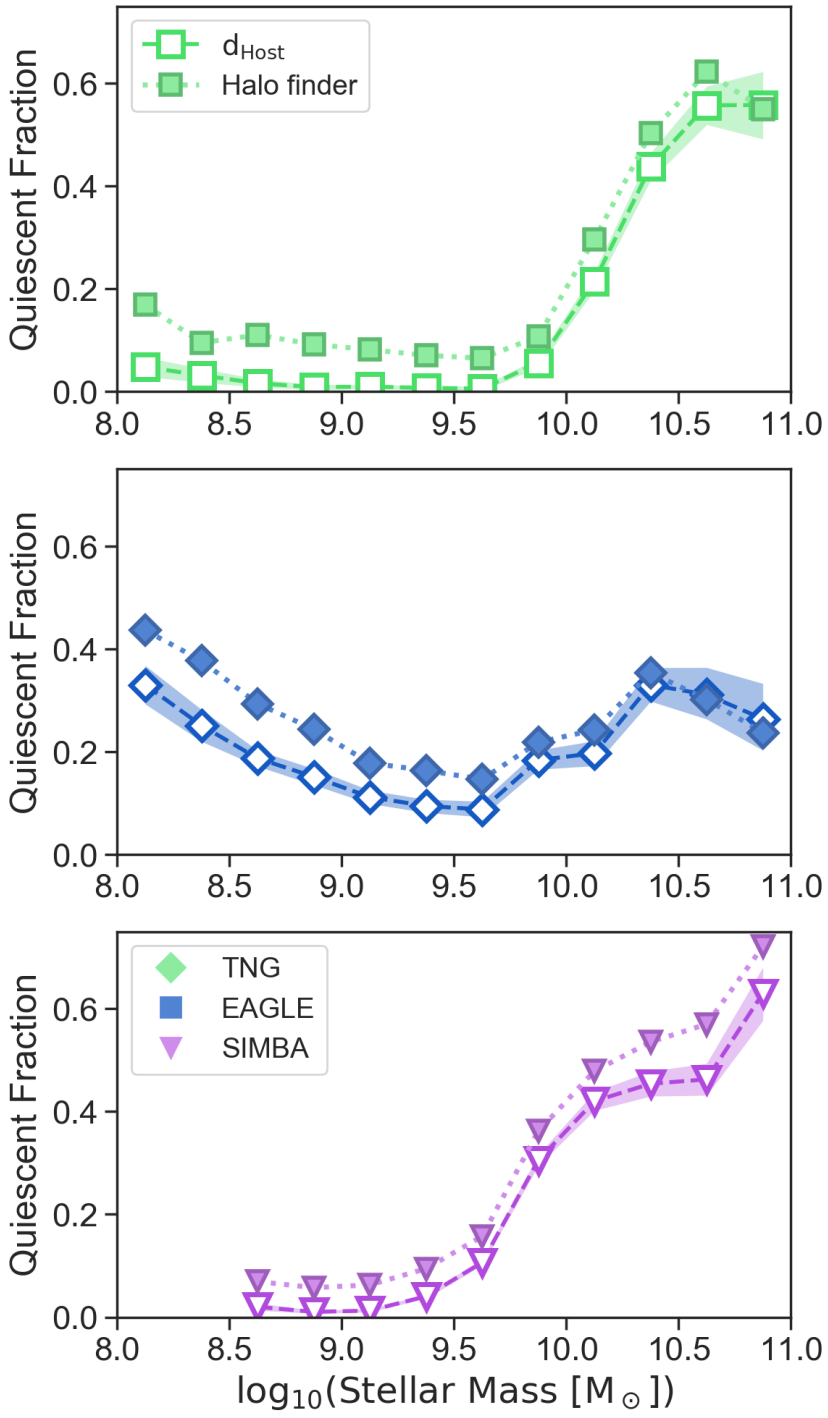

Fig. 3.6: The effects of using a halo finder (filled-color) vs $\mathrm{d_{host}}$ (open-face) to select isolated galaxies on the resultant quiescent fractions in TNG (top), EAGLE (middle), and SIMBA (lower panel). In all three simulations, using the halo finder leads to higher quiescent fractions when compared to $\mathrm{d_{host}}$, driven by the criterion's more restrictive nature.

3.5 The Quiescent Fraction of Isolated Galaxies

In subsection 3.5.1, we compare the quiescent fraction of isolated galaxies from each simulation to observations from SDSS. In subsection 3.5.2, subsection 3.5.3 and subsection 3.5.4 we discuss the effects of simulation resolution, observationally-biased stellar mass, and finite aperture on the quiescent fraction, respectively.

3.5.1 Comparing between simulations and observations

In Figure 3.4, we show the median isolated quiescent fractions for each simulation from 25 randomly placed sightlines (blue, green and purple points, dashed lines), as compared to SDSS (black circles, solid line).

At intermediate stellar masses ($\mathrm{M}_* = 10^{9.5-10.5}\ \mathrm{M}_\odot$), the simulations all show the quiescent fraction decreasing with decreasing stellar mass, qualitatively reproducing the isolated quenching threshold seen in SDSS (Geha et al., 2012). In observations, this is thought to be driven by the waning efficiency of internal feedback mechanisms. The threshold for TNG galaxies appears to be at a higher stellar mass than is seen in observations, while EAGLE's quiescent fraction appears to depend less strongly on stellar mass in this regime.

Unlike the observations, all three simulations have non-zero quiescent fractions below $\mathrm{M}_\odot = 10^9\ \mathrm{M}_*$ (Figure 3.4, inset). For both SIMBA and TNG the quiescent fraction, though non-zero, remains small, with $f_q \sim 0.01$ at $\mathrm{M}_\odot = 10^9\ \mathrm{M}_*$. Overproduction of quiescent galaxies in EAGLE is more pronounced.

We examine the distribution of quiescent galaxies as a function of environment in two mass bins just above and below the observed quenching threshold for isolated galaxies ($10^{8.5-9.0}$ and $10^{9.5-10.0}\ \mathrm{M}_*$) in Figure 3.5. At intermediate stellar masses (upper panel), EAGLE and SIMBA are a good qualitative match to observations,

with low quiescent fractions for isolated galaxies and no environmental dependence in the isolated regime. TNG lies below the SDSS observations, with an average $f_q \sim 0.05$ beyond $\mathrm{d_{host}} = 1.5$ Mpc. At lower stellar masses (lower panel), EAGLE's over-production of quiescent galaxies in all environments is more pronounced, while SIMBA and TNG are in better agreement, with a near absence of quiescent galaxies beyond $\mathrm{d_{host}} = 1.5$ Mpc.

In general, the rapid increase of f_q at $\mathrm{d_{host}} < 1.5$ Mpc is in qualitative agreement with observations. However, it is notable that all three simulations also overproduce low mass, *non-isolated* quiescent galaxies, at a many sigma tension given the derived errors. Feedback models for satellite galaxies are often tuned to reproduce galaxies in the Local Group. The SAGA Survey (Mao et al., 2020) recently showed that the Local Group satellites may be over-quenched relative to those around more typical MW-mass galaxies, which may be driving this tension.

In Figure 3.6, we show how the observed isolated quiescent fraction changes with different definitions of "isolation". For each simulation, we compare f_q derived using $\mathrm{d_{host}}$ and f_q from each simulation's halo finder. In each case, the halo finder produces a larger quiescent fraction (with the exception of $\mathrm{M_*} > 10^{10.5}\ \mathrm{M_\odot}$ in TNG and EAGLE). This effect varies as a function of stellar mass (as well as halo finder used), and highlights the differences between selecting a sample of central galaxies versus isolated galaxies.

3.5.2 Resolution effects

All three cosmological simulations used in this work have multiple runs at varying resolutions. SIMBA and EAGLE both have smaller boxes with higher resolution and we use these boxes to test our results specifically with respect to resolution. While we do not use the higher resolution version of TNG (TNG50) we note that the effect

of resolution on the colors and color bimodality of galaxies is described in Nelson et al. (2018). They argue that the main effect of resolution on galaxy colors is in using purely the stellar particles to derive a star formation history. While we avoid this effect by including instantaneous SFR in the SFHs used to generate our spectra (to reflect the most recent star formation), future work should address explicitly the resolution convergence properties of TNG for the quiescent fractions of low mass galaxies.

In Figure 3.7 we show the quiescent fraction as a function of stellar mass for the SIMBA and EAGLE higher resolution boxes (light colors, dot and dot-dashed lines) and compare those to the default box and resolution from Figure 3.4 (dark colors, dashed lines). Because the high-resolution boxes are much smaller in volume, we determine the effect from cosmic variance on the quiescent fraction. To do so, we recompute the quiescent fraction for subboxes of 30Mpc on a side from our default simulation boxes and show the full range of recovered quiescent fractions with the grey shaded regions in each panel. Due to the smaller total number of galaxies, we also use wider mass bins to calculate the quiescent fraction.

For the EAGLE simulations we specifically compare to two boxes of 25Mpc on a side, run using the "Reference" (REF) version of the code (identical to the 100Mpc box), and using the "Recal" version of the code which is re-calibrated at this higher resolution of $m_{\rm DM} = 1.21 \times 10^6$ M$_\odot$ and $m_{\rm gas} = 2.26 \times 10^5$ M$_\odot$ to counterbalance resolution effects on the subgrid physics (see Schaye et al., 2015; Schaller et al., 2015, for a complete argument and description of the re-calibration, and a comparison of the different versions).

The quiescent fraction of the REF high-resolution box is slightly suppressed compared to that for the large box, falling below what can be explained by cosmic variance alone (gray shading) for the lowest masses. The re-calibrated high-resolution box (RECAL) are further suppressed relative to both the fiducial and REF boxes, and

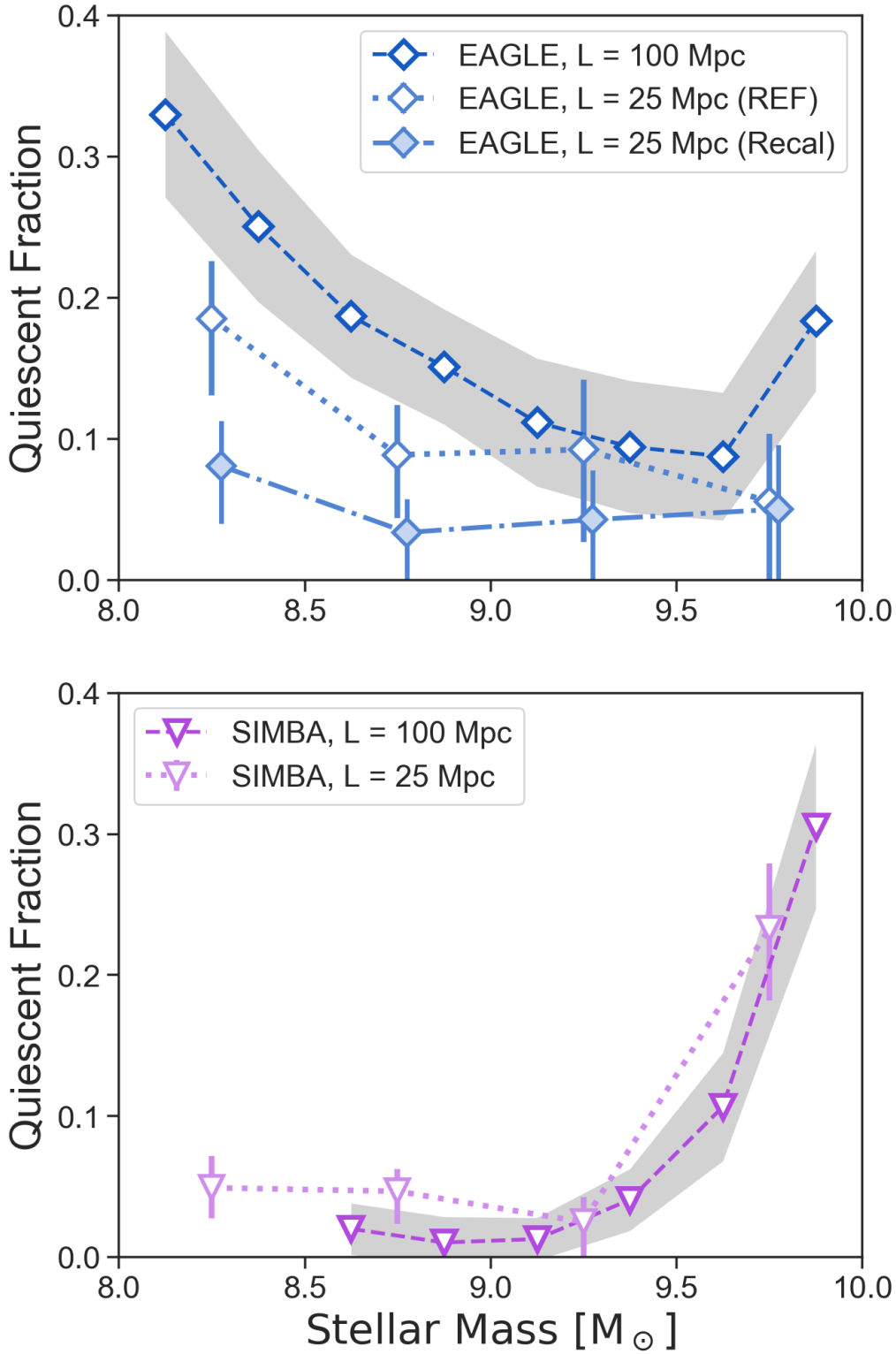

Fig. 3.7: The effects of resolution on the isolated quiescent fraction in EAGLE (upper panel) and SIMBA (lower panel). In both panels, dashed lines show the fiducial quiescent fractions from the large volume, while dotted or dot-dashed lines show the quiescent fractions measured from the higher resolution $(25\ \mathrm{Mpc})^3$ volumes. The gray shaded regions represent the maximum variation due to cosmic variance when considering $(30\ \mathrm{Mpc})^3$ sub-volumes from each large volume simulation. In the upper panel, data from the two high resolution simulations are offset horizontally so that the errorbars may be distinguished.

this effect is most extreme at the lowest stellar masses. Schaye et al. (2015) argue that re-calibrating at different resolutions is most appropriate, as (un)physical effects of resolution may be hard to trace. Of the three EAGLE runs examined here, the RECAL box produces the fewest number of quiescent galaxies below $\mathrm{M}_* = 10^9\ \mathrm{M}_\odot$, and even agrees with a quiescent fraction of $f_q = 0$ within the uncertainties for three of the four stellar mass bins. The recalibrated high-resolution EAGLE box is therefore in closest agreement with the observations, though f_q does not show the same strong dependence on stellar mass in the mass range $\mathrm{M}_* = 10^{9-10}\ \mathrm{M}_\odot$ that is observed in SDSS. Additionally, both high resolution boxes still show an overabundance of low mass quiescent galaxies in isolation.

For SIMBA the quiescent fraction of low mass galaxies increases slightly at higher resolution, which is run with identical physics to the larger-scale box. We find that the high-resolution box agrees with the fiducial run, with a quiescent fraction that is slightly elevated relative to the fiducial run at $\mathrm{M}_* = 10^{8.5-9.0}\ \mathrm{M}_\odot$. Improved resolution allows for the measurement of the quiescent fraction down to slightly lower stellar masses, which we find to be $f_q \sim 0.06$. This is still in tension with SDSS, where no quiescent galaxies are observed in isolation below $\mathrm{M}_* = 10^9\ \mathrm{M}_\odot$.

We highlight that the effects of resolution, as exemplified by these case studies, are not uniform across simulations and can increase or decrease the quiescent galaxy fraction.

3.5.3 Stellar mass

In earlier work, Munshi et al. (2013) found that the stellar masses measured for simulated galaxies with a combination of synthetic Petrosian magnitudes and Bell & de Jong (2001) mass to light (M/L) ratios underestimate the true stellar mass by about 50%. This underestimate varied only slightly as a function of mass. Similarly,

Leja et al. (2019) have shown that stellar masses inferred from SED modelling with non-parametric SFHs are roughly ~ 0.2 dex larger than those obtained under the assumption of an exponentially declining SFH.

We confirm the approximate magnitude of this effect using the $g-r$ color-based approximation for stellar mass from Mao et al. (2020), which produces stellar masses that underestimate the true stellar masses by ~ 0.3 dex. In addition to shifting the quenching threshold to lower stellar masses, accounting for systemic error in the measurement of stellar mass leads to a softening of the slope of the quiescent fraction.

3.5.4 Aperture effects

Our fiducial mock galaxy spectra are based on galaxy properties and star formation histories calculated using all the star and gas elements considered to be part of a simulated galaxy's subhalo. In comparison, observations of galaxies in SDSS are aperture-limited. There are two SDSS apertures that are important for our results: the photometric aperture and the spectroscopic fiber aperture. The first roughly correspond to with what is considered the size of a galaxy and is relevant for the stellar masses used in this work, and the second for the $\mathrm{D_n4000}$ and $\mathrm{H}\alpha$ EW measurements.

With respect to "galaxy size"-aperture effects: previous work using the EAGLE and TNG simulations have found that these aperture effects are significant for high-mass ($\mathrm{M_*} \gtrsim 10^{11}\ \mathrm{M_\odot}$) galaxies but negligible for lower mass galaxies (Schaye et al., 2015; Donnari et al., 2020a), and we reach similar conclusions when comparing stellar masses in the full subhalo and within a 30 kpc aperture for TNG. Therefore, we conclude that aperture effects are likely insignificant for stellar masses, in particular when compared to other uncertainties as discussed in the previous section.

The aperture of the SDSS spectroscopic fiber typically covers a few kpc in the central region of a galaxy. This means that aperture effects again, are crucial to take into account at higher masses, but can be small for low mass galaxies as there the SDSS fiber aperture may cover a significant fraction of the galaxy. We have checked the differences in $\mathrm{D_n}4000$ and Hα EW when only considering the central $r < 2$ kpc region of each galaxy. While Hα EW is more variable as a function of aperture (driven by changes in the amount of continuum contained within the aperture), galaxies do not significantly shift in or out of the quiescent region (which is based on both Hα EW and $\mathrm{D_n}4000$). In particular, we find only small differences in the quiescent fractions for low mass galaxies, which shift upwards by $\sim 10\%$.

For some observed galaxies the SDSS fiber may have been centered on an off-center bright (star-forming) region. With smaller (lower-mass) galaxies this possibility diminishes purely due to the fact that more of the total galaxy fits within the fiber aperture. Moreover, this is more likely to happen in actively star-forming galaxies, and as we purely use the spectral indices to classify galaxies as star-forming or quiescent, off-center fiber positioning is unlikely to affect our results.

3.6 Quenching mechanisms in simulations

3.6.1 Comparison to previous work

Our work is not the first to compare populations of quiescent galaxies from simulations to observations, though we are the first to compare three large volume simulations to observations in a fully consistent manner. Here, we review past studies evaluating the quiescent populations of each simulation.

EAGLE

The quiescent fraction of galaxies in the EAGLE simulations have been discussed in a multitude of papers, using a variety of galaxy subsamples, and of definitions and tracers of the quiescent fraction. Schaye et al. (2015) find that the passive fraction for all galaxies defined based on specific star formation rates (sSFR; SFR/$M_\star$) is in reasonably good agreement with results from GAMA (Bauer et al., 2013) and SDSS (Moustakas et al., 2013), although these observational results use slightly different criteria. The threshold where the galaxy population goes from predominantly blue and star-forming to predominantly red and quiescent is found to be at slightly higher stellar mass in EAGLE than for observed low-redshift datasets (Schaye et al., 2015; Trayford et al., 2015). Furlong et al. (2015); Trayford et al. (2015, 2017) show that the apparent larger quiescent fraction at the low mass end is largely due to resolution effects as low mass low-SFR galaxies have very few star-forming gas particles, and show that the recalibrated higher resolution box (Recal-25) agrees with observations.

We agree with their results that the recalibrated high-resolution box improves the quiescent fraction compared to the observations (see Figure 3.7 and subsection 3.5.2). Nevertheless, we still find that EAGLE produces a higher quiescent fraction for low mass galaxies than is observed in SDSS. It is noteworthy that EAGLE has a particularly high fraction of low mass galaxies that are classified as quiescent but do have current star formation at very low rates. This gives credence to the possibility that the SFR of these galaxies is poorly resolved and that these galaxies are misclassified as quiescent. However, our quiescent definition requires both low Hα and high $\mathrm{D_n}4000$. While the Hα can be affected by these resolution effects, the $\mathrm{D_n}4000$ is based on the stellar continuum, and probes a longer timescale. Our quiescent fraction may therefore be less dependent on resolution than for a purely Hα-based definition.

At higher masses the quiescent fraction we find for EAGLE seem particularly low compared to earlier work based on SFR or sSFR. However, Trayford et al. (2017) show the similar results for $\mathrm{D_n}4000$-defined quiescent fractions, and in addition show that dust can affect the discrepancy: when including dust the passive fraction in EAGLE based on a cut of $\mathrm{D_n}4000 > 1.8$ is 35% reduced compared to results from SDSS for galaxies in the mass range $10^{10}\ M_\odot < M_* < 10^{11}\ M_\odot$, while without including dust this discrepancy increases to 70% (Trayford et al., 2017). These discrepancies are larger than what we find in this work and may be because our stellar mass-dependent $\mathrm{D_n}4000$-based definition of quiescence, which is identical to the one used for the SDSS sample, reaches a lower value at similar masses.

Illustris-TNG

Donnari et al. (2020a) and Donnari et al. (2020b) provide an in-depth exploration of the quenched galaxy fraction in TNG, exploring the effects of aperture, quenching definition, SFR timescale, environmental mis-identification, and incompleteness on the quenched fraction. While they focus on galaxies with $\mathrm{M_*} > 10^9\ \mathrm{M_\odot}$ and use SFR or SFS-based definitions of quiescence, we nonetheless find their fiducial quiescent fraction to be in excellent qualitative agreement with our results, specifically the existence of a quenching threshold just above $\mathrm{M_*} = 10^{10}\ \mathrm{M_\odot}$, a small population of isolated (central) galaxies which are quiescent below $\mathrm{M_*} = 10^{9.5}\ \mathrm{M_\odot}$, and a rapid increase in the number of quiescent galaxies from $\mathrm{M_*} = 10^{10-11}\ \mathrm{M_\odot}$.

Donnari et al. (2019) describe the galaxy star forming sequence and the quenched fraction using different definitions and tracers for TNG100. They find that both a UVJ-selected quenched fraction and a distance from the star forming sequence-selected quenched fraction agrees reasonably well with observations, although they use a different UVJ selection for TNG than for the observations they compare to (from Muzzin et al., 2013).

In a by eye comparison, our TNG quiescent fractions (defined based on $\mathrm{D_n}4000$ and $\mathrm{H}\alpha$) are overall lower than the UVJ-and-SFS-based quenched fraction from Donnari et al. (2019), in particular at the lower-mass end. A similar difference can be found between the UVJ-selected (Muzzin et al., 2013) and $\mathrm{D_n}4000$ and $\mathrm{H}\alpha$-selected (Geha et al., 2012) observed quiescent fractions at $M_\star < 10^{10}\ M_\odot$. As it is unlikely that low mass star-forming galaxies move into the UVJ selection region due to dust, this suggests that the these low mass systems are predominantly red, but still exhibit some low (relatively recent) star formation which can be traced by their $\mathrm{D_n}4000$ and/or $\mathrm{H}\alpha$EW.

SIMBA

Davé et al. (2019) have compared the specific star formation rates of SIMBA galaxies to observations from the GALEX-SDSS-WISE Legacy Catalog (Salim et al., 2016, 2018) and found good agreement, which is also consistent with our findings of very good agreement between the quiescent fraction from SIMBA and that observed in SDSS.

Davé et al. (2019) also suggest that the few low mass quiescent galaxies are in fact satellites misclassified by the FOF-based halo finder. Additionally Christiansen et al. (2019); Borrow et al. (2020) show that jet feedback from AGN in SIMBA can influence large regions around the AGN host galaxy and can entrain gas and influence gas in nearby galaxies. The SIMBA 100 Mpc box contains a massive cluster ($\mathrm{M_*} \sim 10^{15}\ \mathrm{M_\odot}$) and the high-resolution 25 Mpc box also has an anomalously large central halo. However, we confirm that in both boxes, the majority of the quiescent galaxies we select are at least 2 Mpc away from the cluster or most massive halo center, and most are more than 5 Mpc away. Our results suggest that there may be additional effects driving the non-zero quiescent fraction at low mass (see Figure 3.5, lower panel).

Low mass, quiescent galaxies in SIMBA are also found to be over-sized compared to their star forming counterparts (Davé et al., 2019). However, this should lead to a higher fraction of quiescent galaxies removed from the survey due to the SDSS surface brightness limits. Fixing this issue would therefore only increase the population of low mass, quiescent galaxies in SIMBA.

3.6.2 Low mass, isolated and quiescent galaxies in simulations

Given the observed over-abundance of quiescent galaxies at low mass in the simulations, we consider what feedback mechanisms might drive quenching in these systems.

Black holes: some of the low mass galaxies in our sample will contain black holes (almost all galaxies above $\mathrm{M}_* = 10^9\ \mathrm{M}_\odot$ in TNG and EAGLE, and above $\mathrm{M}_* = 10^{9.5}\ \mathrm{M}_\odot$ in SIMBA). Feedback from central supermassive black holes is often thought to be able to quench galaxies, and possible important in keeping galaxies quiescent (e.g., Somerville & Davé, 2015, recent discussions include Chen et al., 2020; Terrazas et al., 2016, 2020). However, in the models the black hole feedback often becomes effective only at certain black hole masses (McAlpine et al., 2017; Bower et al., 2017; Weinberger et al., 2018; Thomas et al., 2019; Terrazas et al., 2020; Habouzit et al., 2020), which are not reached in low mass galaxies. Moreover, not all of the low mass galaxies in these simulations will host black holes (especially at $\mathrm{M}_* < 10^9\ \mathrm{M}_\odot$), so while black hole feedback could play some role, it is unlikely to the exclusive driver the quenching of the lowest mass galaxies in each simulation.

Star formation feedback: Feedback from star formation is generally thought to reduce the efficiency of galaxy formation at the lower mass end (Somerville & Davé, 2015; Schaller et al., 2015; Schaye et al., 2015; Pillepich et al., 2018b; Davé et al., 2019). Outflows from star formation feedback can temporarily expel large

amounts of gas and decrease the gas density of galaxies. This is commonly seen in higher resolution simulations of lower mass galaxies (halo masses $\lesssim 10^{10}\ M_{\odot}$ Wright et al., 2019; Wheeler et al., 2015, 2019; Rey et al., 2020). These effects may result in temporary quiescence, but it is unclear if supernovae are capable of removing enough gas to fully quench galaxies at $\mathrm{M}_{*} \sim 10^{9}\ \mathrm{M}_{\odot}$. Temporarily quiescent low mass galaxies may however, compose part of our quiescent low mass galaxy samples. In large-scale simulations used in this work, the effectiveness of stellar feedback is likely also affected by resolution at the lowest mass end, and the effects of feedback and resolution may be hard to disentangle.

Splashbacks: galaxies moving through larger halos can have their gas stripped away, reducing star formation. Splashback galaxies can be found up to $\sim 3\mathrm{R}_{\mathrm{vir}}$ (see e.g., Diemer, 2020) from their true host galaxy, making misidentification possible. However, our $\mathrm{d}_{\mathrm{host}}$ isolation criterion is more restrictive than the halo finders (see Figure 3.6), making it unlikely that more than a small fraction of the isolated quenched galaxies observed in each simulation are splashbacks.

Outflows from nearby massive galaxies: Borrow et al., 2020 and Wright et al., 2019 show that the gas of low mass galaxies (both satellites and low mass centrals) can be stripped or entrained by jets and AGN outflows from more massive halos. While many of the observed isolated galaxies lie many virial radii from any massive halos, this gas removal effect could contribute to the elevated quenched fractions seen in the simulations.

3.7 Star Formation Histories of Quiescent Galaxies

By forward modelling simulated galaxies into observational space, we gain the ability to look back at the "true" properties of observationally-selected galaxies. One of the most informative properties of a galaxy is its star formation history. For each

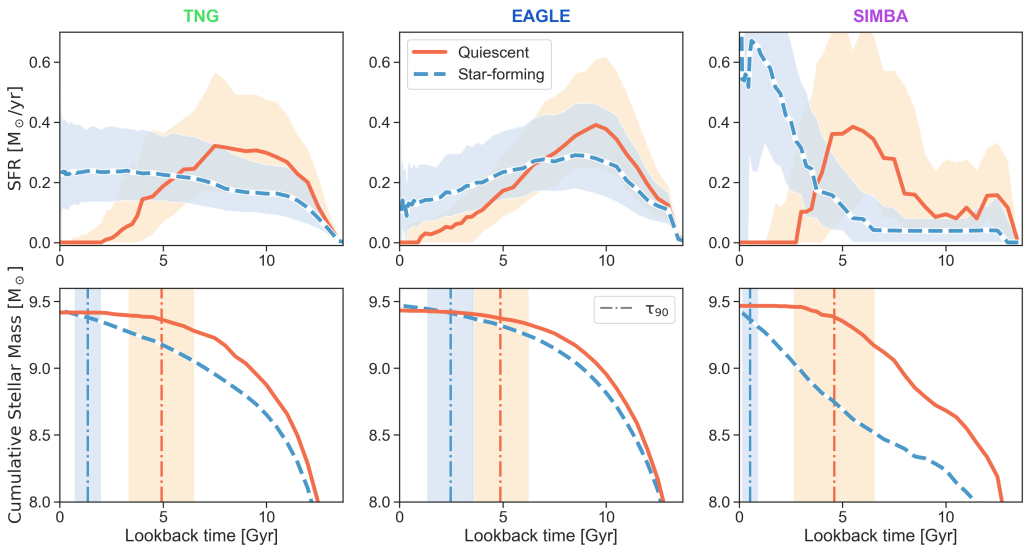

Fig. 3.8: *Top row:* The median star formation histories of low mass ($M_* = 10^{9.0-9.5}$ $M_\odot$), isolated galaxies in each simulation, split into star forming (blue, dashed) and quiescent (orange, solid), using the D_n4000-Hα EW criteria at $z = 0$. Shaded regions encompass the 20-80th percentile of each distribution.
Bottom row: The median cumulative stellar mass as a function of lookback time for the star forming and quiescent samples of isolated galaxies at low mass in each simulation. Vertical dot-dashed lines show the average time at which 90% of a galaxy's stellar mass had formed (τ_{90}). Though the star formation histories of quiescent galaxies vary across the three simulations, the average quenching timescales derived for the three populations are effectively identical ($\tau_{90} \sim 5$ Gyr).

simulated galaxy, we are able to compare the observed properties back to the biases inherent in the recovery of star formation histories from real data.

In Figure 3.8 (upper row), we show the median star formation histories of low mass ($\mathrm{M}_* = 10^{9.0-9.5}\ \mathrm{M}_\odot$) isolated galaxies observed as star-forming (blue dashed lines) and quiescent (orange solid lines) at $z = 0$ in each simulation. The shape of the median star formation histories in each simulation varies significantly. Low mass star forming galaxies in SIMBA show late-time rising star formation histories, while the same galaxies in TNG have approximately flat star formation histories, both in clear contrast with their quiescent counterparts.

In EAGLE, the star formation histories are declining at late times for both the star forming and quiescent populations, and in fact a significant fraction of the low mass quiescent galaxies appear to be forming stars at very low rates at late times. This may be connected to the relatively low scatter in the EAGLE galaxy star-forming sequence (see Hahn et al., 2019) and in the EAGLE star formation histories (Iyer et al., 2020). In particular, the declining and low star formation rates for EAGLE's low mass galaxies may be connected to the relatively high quiescent fraction that we find using the $\mathrm{D_n}4000$ and Hα EW selection. Figure 3.2 illustrates that of the three simulations in our sample, EAGLE has a notably large fraction of low mass, low-SFR galaxies that are borderline star-forming when considering their specific star formation rates, but have such low SFR that they are classified as quiescent when using the $\mathrm{D_n}4000$ and Hα EW measurements.

In the bottom row of Figure 3.8 we show the median cumulative stellar mass as a function of lookback time for the same star forming and quiescent samples. The vertical dot-dashed lines show the average time at which quiescent and star-forming galaxies formed 90% of their stellar mass (Skillman et al., 2017; Weisz et al., 2015). Despite the apparent variation in the late time star formation histories of the quiescent populations observed in each simulation, τ_{90} is nearly identical:

$\tau_{90,\mathrm{TNG}} = 4.9 \pm 1.6$ Gyr, $\tau_{90,\mathrm{EAGLE}} = 4.9 \pm 1.4$ Gyr, and $\tau_{90,\mathrm{SIMBA}} = 4.6 \pm 2.0$ Gyr. The measurement of $\tau_{90} \sim 5$ Gyr for low mass quiescent galaxies in isolation is a testable prediction for the observational sample and should provide insight into the timescale of feedback mechanisms which drive quenching in low mass galaxies.

Of the galaxies observed as quiescent, a subset in each simulation have non-zero instantaneous star formation rates at $z = 0$ (approximately 50% of low mass galaxies in TNG and EAGLE, and 20% in SIMBA). The empirical definition of quiescence used throughout this work (based on $\mathrm{D_n}4000$ and Hα EW) selects galaxies with a range of evolutionary histories and $z = 0$ properties. We find that the SFR=0 galaxies do not separate out cleanly in $\mathrm{D_n}4000$ - Hα EW space (highlighted in Figure 3.2). In order to select a totally quiescent sample of galaxies, additional probes of SFR would be required. Characterizing exactly how much ongoing star formation a galaxy can experience while still being selected by a given definition of quiescence will help inform the selection of appropriate quenching criteria (e.g., UVJ vs SFR vs $\mathrm{D_n}4000$) going forward.

In future work, we will constrain the average quenching time for observed quiescent galaxies in isolation via SED fitting, and apply the same process to the synthetic spectra. Applying the same SED fitting methods to the synthetic data is critical, as the observed differences in the late time star formation history may only be recoverable above a certain threshold of data quality (e.g., spectrum SNR, photometric wavelength coverage).

3.8 Conclusions

In this paper, we have produced mock SDSS-like surveys from three large volume hydrodynamic simulations (Illustris-TNG, EAGLE, and SIMBA) from which we

measured the quiescent fraction of isolated galaxies and compared back to extant constraints from the local universe (Geha et al., 2012). We find that:

1. The three simulations examined in this work, when transformed into observational space using an identical methodology, produce three different dependencies of the quiescent fraction on stellar mass. Above $\mathrm{M}_* = 10^{9.5}\ \mathrm{M}_\odot$, all three simulations qualitatively reproduce the declining quiescent fraction with decreasing stellar mass observed in SDSS.

2. All three simulations have non-zero quiescent fractions below $\mathrm{M}_* = 10^{9.0}\ \mathrm{M}_\odot$, in contrast to observations of the SDSS volume. This suggests that current models of feedback in the low stellar mass regime are too efficient.

3. Our empirical definition of quiescence selects low mass galaxies with a range of star formation histories when viewed over longer (many Gyr) timescales. However, these populations all show similar quenching timescales ($\tau_{90} \sim 5$ Gyr), which can be compared back to observations. Understanding how sensitive a particular definition of quenching is to formation history can inform future population studies.

4. Measuring the quiescent fraction in a higher resolution box does not fully resolve the overabundance of quiescent galaxies below $\mathrm{M}_* = 10^{9.0}\ \mathrm{M}_\odot$. In fact, improved resolution can lead to either a significant decrease or slight increase in the measured quiescent fraction, depending on the simulation. While the low mass quiescent fraction is not converged in the large-scale simulations, the discrepancy with observations persists at higher resolutions.

The low mass quenching threshold of isolated galaxies represents an observational boundary condition; a stellar mass regime where internal feedback mechanisms become ineffective. Observations of the isolated galaxy quiescent fraction provide a unique probe into the delicate balance of internal feedback mechanisms

in low mass galaxies. Understanding how well or poorly modern simulations of galaxy evolution can reproduce this feature is a novel test of feedback prescriptions, but requires the creation of mock observations and surveys to enable appropriate comparisons between the observed universe and simulations.

Our method for producing mock surveys from large volume hydrodynamic simulations can also be applied to zoom-in simulations and semi-analytic models, and adapted to match other surveys and observations. Future work will explore the star formation histories recovered from synthetic observations as compared to those derived from observations, as well as the observed gas properties of simulated galaxies.

The constraining power of the observations we compare to are set by the size of the SDSS volume and the limiting magnitude and surface brightness of the survey. Future wide-field surveys such as the Vera Rubin Observatory's Large Synoptic Survey Telescope (LSST; Ivezić et al., 2019) and the Dark Energy Survey Instrument (DESI; DESI Collaboration et al., 2016) have the potential to substantially improve our census of the local universe, providing new constraints on the population of low mass, quiescent galaxies in the field.

Making direct comparisons between observations and simulations requires the careful translation from the simulation to observational frame (or vice versa). In doing so, we gain novel insights into the ways that feedback shapes the evolution of galaxies.

4

The over-quenching of Milky Way satellites in simulations

> *Tell me of a complicated survey.*
> *Muse, tell me how it observed and was measured*
>
> — **The Odyssey, Homer**
> *(if he were an astronomer)*
> trans. Emily Wilson

Claire Dickey, Marla Geha, and the SAGA team, *manuscript in prep.*, **xx**, yy (2021)

ABSTRACT

We compare three major large-scale hydrodynamical galaxy simulations (EAGLE, Illustris-TNG, and SIMBA) by forward modeling simulated galaxies into observational space and computing the fraction of satellites of Milky Way analogs that are quiescent as a function of stellar mass. Using the SAGA survey as our observational template, we create mock surveys and synthetic spectroscopic and photometric observations of each simulation, adding realistic noise and observational limits. All three simulations show an increase in the number of quiescent satellite galaxies, in good agreement with observations of the Local Group satellites. However, the SAGA survey shows significantly lower quiescent fractions for satellites of Milky Way analogs. We find that the simulations also produce a population of faint, red satellites that have not been detected by the SAGA survey. These galaxies have extremely old ages and represent either a population that has thus far been missed by observations or artifacts of unphysical processes in the simulations. We identify analogs of this population in a wide variety of environments, from isolation to dense groups. We also use the mock surveys to demonstrate the sensitivity of definitions of quiescence to observational noise.

4.1 Introduction

The Milky Way is the most well-studied galaxy in the universe and its satellite galaxies have received similarly high degrees of scrutiny. In-depth studies of our home galaxy system have shaped and informed modern theories of galaxy formation and evolution. As such, reproducing the Milky Way satellites is a critical benchmark for cosmological simulations that contain models for galaxy evolution.

A major stumbling block in this realm has been the "Too Big to Fail" problem, in which dark matter-only (DMO) simulations using a Lambda Cold Dark Matter (ΛCDM) cosmology produce too many massive subhalos around central halos that should contain Milky Way-mass galaxies. Possible explanations for the mismatch between the predicted dark matter halos and the observed satellite population include: the mass of the Milky Way is lower than previously thought (putting the galaxy into a less massive dark matter halo with less massive corresponding subhalos), an alternate paradigm to CDM (leading to different expectations for dark matter substructure), or a need for more realistic treatments of baryonic physics in simulations (reducing either the stellar mass of galaxies residing in these halos or the density of the halos themselves through baryonic feedback processes).

The addition of more realistic treatments of baryons has shown significant promise for resolving the observed discrepancies (Brooks & Zolotov 2014; Wetzel et al. 2016; Brooks et al. 2017). High-resolution studies of individual galaxies have demonstrated that small-scale baryonic processes can shape not just galaxies but also the dark matter halos they reside in.

However, the wide range in relevant physical scales involved in galaxy formation and evolution demand that simulations make approximations of the underlying physics in order to keep computation times feasible. Hydrodynamical simulations of cosmological volumes large enough to have statistically significant numbers of

galaxies rely on complex "subgrid models" for the relevant physical processes. These models include approximations for the mechanics of star formation, the heating and cooling of gas, the formation and growth of black holes, and the ejecta from active galactic nuclei and evolving stars. The exact balance and interplay of these processes remain uncertain and an area of ongoing study.

By tuning the feedback models to a selection of observations of galaxy populations, simulations are able to qualitatively reproduce the observed universe. There are a large number of hydrodynamical simulations that produce qualitatively realistic volumes, all of which rely on unique subgrid approximations to model baryonic feedback processes.

The ability of simulations to produce Milky Way-like systems without deviating from ΛCDM is often presented as an indication that the subgrid models are realistically capturing the underlying physics of galaxy evolution. This assertion allows for the continuous study of a selected galaxy population or individual galaxy as it evolves across cosmic time, something that is impossible to do directly in the observed universe.

Based on the subgrid models that lead simulations to reliably produce analogs of the Milky Way and its satellites, we can potentially learn a great deal about the physical processes that drive the formation and evolution of satellite galaxies. However, the Milky Way is just a single data point and studies indicate that its satellites are something of an outlier when compared to satellites of similar-mass galaxies.

Though the tension between DMO simulations and observations of the Milky Way satellite population have potentially profound implications, the Milky Way and its satellites are just one system. Studies based on the Sloan Digital Survey (SDSS) show that the Milky Way hosting two bright satellites (the Large and Small Magellanic Clouds) is unusual but not wildly so. However, SDSS and other wide-field

surveys are not extremely deep and are unlikely to observe less massive satellites around even the most nearby Milky Way-like galaxies.

The Satellites Around Galactic Analogs (SAGA) Survey[1] is an ongoing spectroscopic survey working towards the characterization of the complete satellite populations around 100 Milky Way analogs down to a satellite stellar mass of $M_* \sim 10^6\ M_\odot$. Data Release 2 contains 36 Milky Ways with 127 satellite galaxies, which can serve as a point of comparison against the Local Group and its satellite population. Current results suggest that while the Milky Way satellite luminosity function is consistent with being drawn from the same distribution as the SAGA luminosity function, Milky Way satellites are more quiescent than those observed in SAGA's systems.

The IQ (Isolated & Quiescent) Collaboratory[2] is focused on understanding quenching through comparative studies, both simulation to simulation and simulation to observations. In Dickey et. al 2020 (hereafter IQ Paper 2) we presented Orchard, which creates mock surveys from large volume hydrodynamical simulations. In that work, we created an "apples-to-apples" comparison of the quiescent fraction of isolated low mass ($M_* < 10^{10}\ M_\odot$) galaxies as a function of stellar mass, using observations of the local universe from the Sloan Digital Sky Survey (SDSS) and a set of simulations, all of which produce realistic cosmological volumes using distinct implementations of subgrid physics (EAGLE, Illustris-TNG, and SIMBA). All three simulations showed a decrease in the number of quiescent, isolated galaxies in the mass range $M_* = 10^{9-10}\ M_\odot$, in broad agreement with observations. However, even after accounting for observational and selection biases, none of the simulations reproduced the observed absence of quiescent field galaxies below $M_* < 10^9\ M_\odot$.

In that work, we also noted that simulations' quiescent fractions as a function of distance to nearby massive galaxies were also significantly higher than what

[1] sagasurvey.org
[2] https://iqcollaboratory.github.io/

is observed in SDSS. To examine the low mass quiescent galaxy populations in non-isolated environments, we now update Orchard to create mock SAGA surveys and explore the satellites of Milky Way analogs in the same three simulations.

In section 4.2, we present the simulations used in this work and in section 4.3 we discuss the observations which serve as our point of comparison. In section 4.4, we create mock surveys from each simulation. section 4.5 presents the satellite quiescent fraction measured from the simulations and explores the satellite populations selected by the mock surveys in each simulation. In section 4.6 we discuss how Orchard can be used to inform definitions of "quiescence" and we review our findings in section 4.7.

4.2 Simulations

As in Dickey et al. (2020), we focus on three large-scale hydrodynamic cosmological simulations (EAGLE, Illustris-TNG, and SIMBA), from which we will create mock surveys to compare to observations.

The Virgo Consortium's Evolution and Assembly of GaLaxies and their Environment (EAGLE) project[3] (Schaye et al., 2015; Crain et al., 2015; McAlpine et al., 2016) has a volume of (100 Mpc)^3 (co-moving), with dark matter and baryonic particle masses of 9.6×10^6 $\mathrm{M}_\odot$ and 1.8×10^6 $\mathrm{M}_\odot$. The simulation uses ANARCHY (Dalla Vecchia, in prep.), a modified version of the Gadget3 N-body SPH code (Springel et al., 2001b; Springel, 2005; Schaller et al., 2015). The subgrid model for feedback from massive stars and AGN is based on thermal energy injection in the interstellar medium (Dalla Vecchia & Schaye, 2012). The subgrid parameters were calibrated to reproduce the $z = 0$ stellar mass function and galaxy sizes.

[3] https://icc.dur.ac.uk/Eagle/

The Next Generation Illustris project (IllustrisTNG or TNG)[4] (Marinacci et al., 2018; Naiman et al., 2018; Nelson et al., 2018; Pillepich et al., 2018a; Springel et al., 2018) is the successor to the original Illustris project (Genel et al., 2014; Vogelsberger et al., 2014), with significant updates in the subgrid models and physics included in the simulation. We use the TNG100 simulation, which has a volume of (110.7 Mpc)^3, and dark matter and baryonic mass resolutions of 7.6×10^6 $\mathrm{M}_\odot$ and 1.4×10^6 $\mathrm{M}_\odot$. TNG is run using the AREPO moving-mesh code (Springel, 2010), which is based on the Gadget code (Springel et al., 2001b; Springel, 2005). Adjustments in the TNG model include the addition of magneto-hydrodynamics, updated stellar feedback prescriptions, and the transition from thermal "bubbles" in the IGM to a BH-driven kinetic wind for the low-accretion-rate black hole feedback mode (Pillepich et al., 2018b; Weinberger et al., 2017).

SIMBA (Davé et al., 2019) is a suite of cosmological simulations built on the `GIZMO` meshless finite mass hydrodynamics code (Hopkins, 2015, 2017), also based on the Gadget code (Springel et al., 2001b; Springel, 2005), and forms the next generation of the MUFASA (Davé et al., 2016) simulations with novel black hole growth and feedback sub-grid models. The fiducial run has a volume of $(143\ \mathrm{Mpc})^3$ and dark matter and baryonic mass resolutions of 9.6×10^7 $\mathrm{M}_\odot$ and 1.8×10^7 $\mathrm{M}_\odot$, respectively. SIMBA includes a model for on-the-fly dust production and destruction (broadly following McKinnon et al., 2017), and star formation is regulated with two-phase kinetic outflows, which were tuned to predictions from the Feedback in Realistic Environments (FIRE) simulations (Hopkins et al., 2014; Muratov et al., 2015; Anglés-Alcázar et al., 2017b; Hopkins et al., 2018). Black hole growth in SIMBA is based on the torque-limited accretion model (Hopkins & Quataert, 2011; Anglés-Alcázar et al., 2013, 2015, 2017a) linking the black hole accretion to properties of the galaxy's inner gas disk. The AGN feedback consists of kinetic bipolar outflows, modeled after observed outflows of AGN, and X-ray feedback input in the surrounding gas similar to Choi et al. (2012).

[4] https://www.tng-project.org/

4.3 The SAGA Survey

Our goal is to compare the properties of satellites around Milky Way analogs as observed by SAGA to those produced in the simulations. Key to this process are three definitions from SAGA:

- Milky Way analog: galaxies with $\mathrm{M}_* = 10^{10} - 10^{11}\ \mathrm{M}_\odot$ and no similar-mass or more massive galaxies within its projected virial radius ($< 300\ \mathrm{kpc}$, $\pm 275\ \mathrm{km/s}$).
- Milky Way satellite: galaxies with $\mathrm{M}_* < 10^{9.5}\ \mathrm{M}_\odot$ within the projected virial radius of a Milky Way analog. SAGA DR2 contains 127 satellites around the 36 Milky Way analogs.
- Quiescence: satellite galaxies are considered quiescent if $\mathrm{H}\alpha\ \mathrm{EW} < 2\ \text{Å}$ as determined from the follow-up spectroscopy.

4.4 Mock SAGA-like surveys

Our goal is to make apples to apples comparisons between simulations and observations of the local universe. Here we focus on reproducing the characteristics of SAGA, rather than SDSS. We use the same set of synthetic spectra for simulated galaxies as in chapter 3 but update Orchard to produce SAGA-like surveys. Our updated methodology for generating mock surveys is detailed below.

1. Place an "observer" at a random location on the surface of the simulation volume. Calculate observational quantities (distance, apparent magnitude, radial velocity) for all galaxies within the volume.
2. Select Milky Way analogs. As in SAGA, we search for Milky Way-like galaxies at $\mathrm{d} = 25 - 40\ \mathrm{Mpc}$ from the observer (selected such that $300\ \mathrm{kpc} \sim 1^\circ$

on-sky for ease of spectroscopic followup). Milky Way analogs must have $M_* = 10^{10} - 10^{11}$ $M_\odot$ and no similarly massive or more massive galaxies within the projected virial radius from the observer's perspective.

3. Identify satellites around each Milky Way analog. Satellites are defined as galaxies with $M_* < 10^{9.5}$ $M_\odot$ within 300 kpc (projected distance) and 250 km/s (radial velocity) of the host galaxy.

4. Add realistic noise to the satellite spectra as a function of apparent magnitude and measure Hα equivalent widths. The noise model is derived from the SNR of the Hα region of AAT and MMT spectra of SAGA satellites.

5. Measure the quiescent fraction of satellite galaxies around Milky Way analogs.

4.5 The Quiescent Fraction of Milky Way Satellites

In Figure 4.1 we show the median quiescent fractions of satellites of Milky Way analogs in the simulations along 100 randomly placed sightlines (blue, green, and purples points with dashed lines) as compared to the SAGA survey (red circles) and the Local Group (orange crosses, from Wetzel+2015).

The three simulations show increasing quiescent fractions towards lower stellar mass, in qualitative agreement with both SAGA and the Local Group. However, all three simulations have higher quiescent fractions than is observed in SAGA at all stellar masses, a result that that mirrors our findings for isolated galaxies in SDSS in Chapter 3. At the highest satellite masses ($M_* > 10^9$) almost no quiescent galaxies are observed in the Local Group or SAGA, while the simulations harbor significant quiescent populations. Of the three simulations, SIMBA comes closest to matching the SAGA quiescent fraction, though it too is persistently over-quenched compared to SAGA.

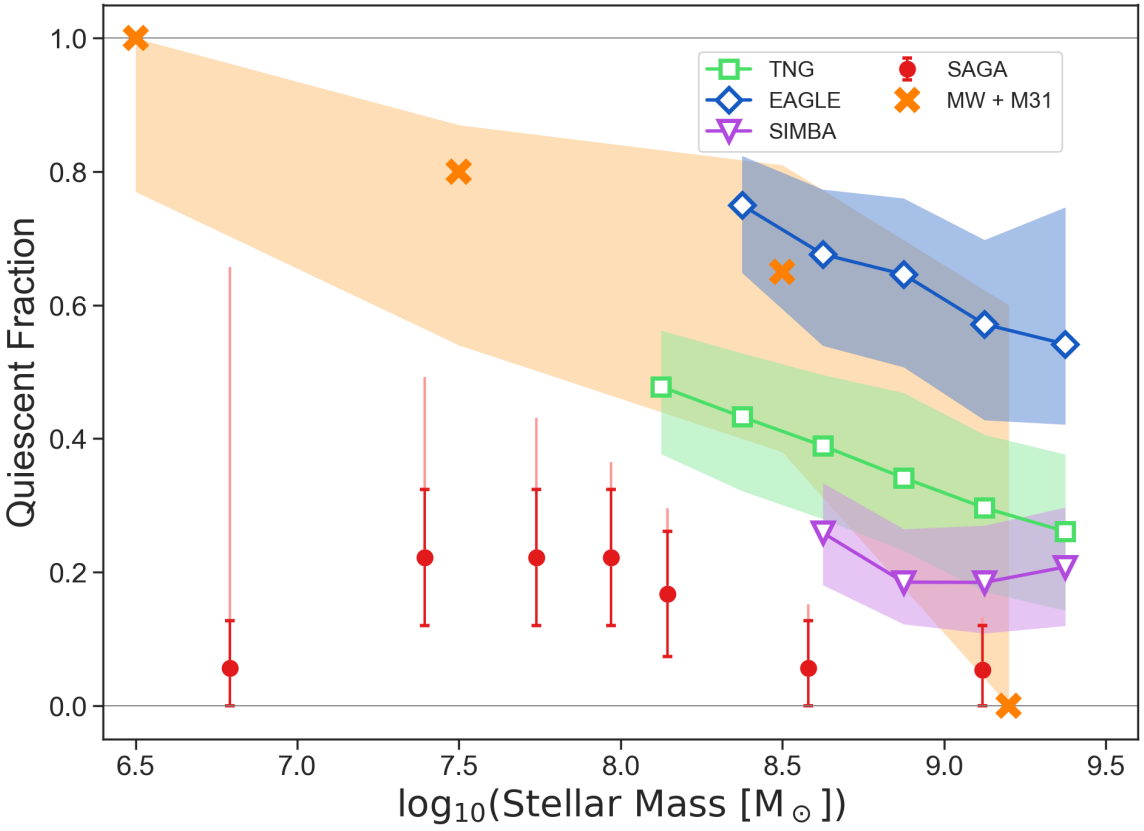

Fig. 4.1: The quiescent fraction of satellites of the Local Group (orange crosses), and Milky Way analogs in SAGA (red circles) and three large volume cosmological simulations (EAGLE, blue diamonds; TNG100, green squares; SIMBA, purple triangles).

4.5.1 Color outliers

A key aspect of the SAGA observational program is the use of color cuts to reduce the number of galaxies that require spectroscopic follow-up around each Milky Way analog. In DR1, only galaxies with $g-r<0.85$ were included in the main sample, though many observations of galaxies with $g-r\geq 0.85$ were taken, confirming the absence of satellites with extremely red colors in the local universe. All of the simulated satellites identified in the mock surveys also fall below this threshold.

However, SAGA DR2 introduced a stricter cut:

$$(g-r)-\sigma_{gr}+0.06\ (r-14)<0.9 \tag{4.1}$$

This cut was once again supported by an absence of any satellites identified via spectroscopic follow-up in this region of color-magnitude space. However, the distribution of satellite colors in the simulations are in tension with the observations from SAGA.

In Figure 4.2 we show $g-r$ color as a function of apparent r magnitude for all low mass galaxies (grey points) and for galaxies observed as satellites of Milky Way analogs (color-coded by $\mathrm{H}\alpha$ EW) in a random sightline. The black line in each panel represents the SAGA DR2 color cut and satellites that be excluded by it (lying in the upper-right region of the CMD) have white borders. On average, $6.8\pm4.5\%$, $8.2\pm4.2\%$, and $3.1\pm4.0\%$ of simulated satellites (in TNG, EAGLE, and SIMBA respectively) lie outside this color cut in a given sightline.

To understand the degree to which the observations and simulations are in tension, we investigate SAGA's completeness for satellite candidates as a function of color and apparent magnitude. Figure 4.3 shows the fraction of all potential satellites in the SAGA survey which received spectroscopic follow-up (binned by color and apparent r magnitude). The "color outlier" satellites from each simulation are

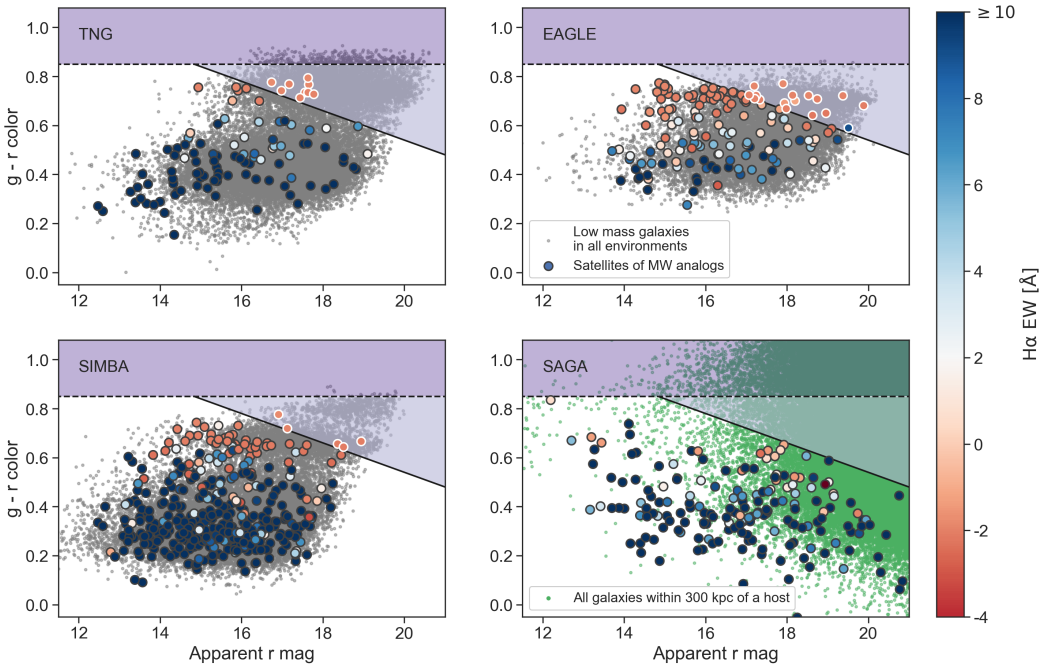

Fig. 4.2: Color - apparent magnitude diagrams for low mass satellites of Milky Way analogs in the three simulations and SAGA (bottom right). Grey points represent low mass galaxies in all environments in the simulations while green points show all SAGA targets within 300 kpc of a Milky Way analog. In all panels, large color-coded points represent confirmed satellite galaxies, with color indicating Hα EW and quiescence (the color-mapping is set such that quiescent galaxies are orange). The shaded regions indicate regions excluded for target follow-up in the SAGA survey (in DR1 this included only the top horizontal slice, $g-r>0.85$, but was extended to include the triangular region at top right in DR2). No satellites have been identified in these regions in SAGA, despite extensive blind targeting, but all three simulations consistently produce satellites that lie in the DR2 excluded region (indicated with white outlines).

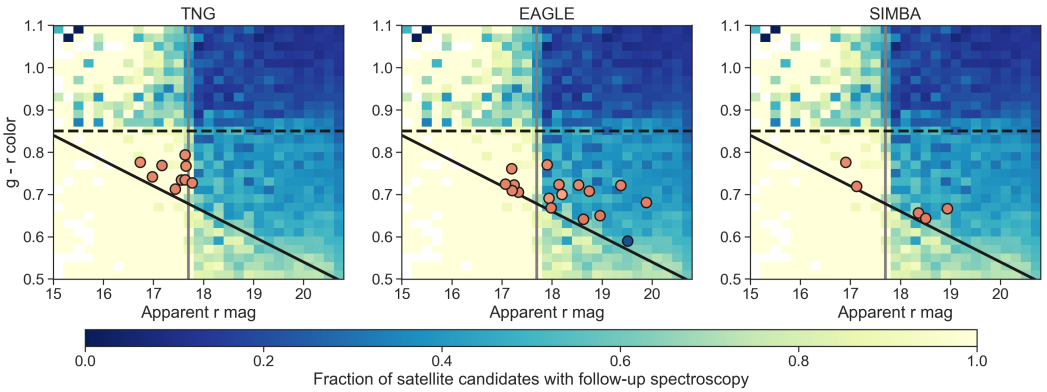

Fig. 4.3: The color - apparent r magnitude diagram showing only satellites with "outlier colors" in each simulation. The dashed and solid black lines show the SAGA DR1 and DR2 outlier cuts, and the grey line at $r = 17.7$ marks the brightness limit of SDSS. Underlying the simulated satellites is the fraction of potential SAGA targets within 300 kpc of a Milky Way analog that received spectroscopic follow-up. A color-magnitude bin that is pale yellow is effectively complete: all potential targets with that color and magnitude received spectroscopic follow-up. Many of the simulated satellites with outlier colors are found in complete bins and should have been identified by SAGA if they exist in the local universe.

over-plotted. All three simulations have satellites which lie in color-magnitude bins that are complete (all possible targets received spectroscopic follow-up) but where no satellites were found, in tension with the predictions from the simulations.

In Figure 4.4 we show the effects of including (solid lines) and excluding (dashed lines) the satellites with anomalous colors on the resultant satellite quiescent fraction. Unsurprisingly, as this is cut a that removes red galaxies, all the galaxies with "outlier colors" are also quiescent (orange colors in Figure 4.2). The change in the quiescent fractions is a tracer of the fraction of quiescent satellites with extremely red colors relative to the total quiescent satellite population in each simulation.

In the case of SIMBA, which has the smallest fraction of color-outliers despite a robust number of quiescent satellites, there is almost no change to the quiescent fraction with the implementation of the color cut. The small decrease at the lowest stellar masses remains within the expected variance due to random sightline orientation (shaded regions).

EAGLE has the highest numbers of "color outliers" of the three simulations, but as in SIMBA, the effects on the quiescent fraction are only seen at the lowest masses. This is likely not because lower mass satellites have redder colors but because the SAGA color cut is more strict at lower apparent r magnitudes.

Of the simulations in this study, the TNG quiescent fraction is most changed by the introduction of a color cut, which more than halves the number of quiescent satellites which would be identified along a sightline in many cases. The removal of a large fraction of the quiescent satellites is actually sufficient to put the TNG quiescent fraction in agreement with SAGA at the lowest stellar masses for which TNG has sufficient resolution. However, the TNG color-cut quiescent fraction shows the opposite trend to SAGA, with the fraction decreasing towards lower stellar masses rather increasing as in SAGA.

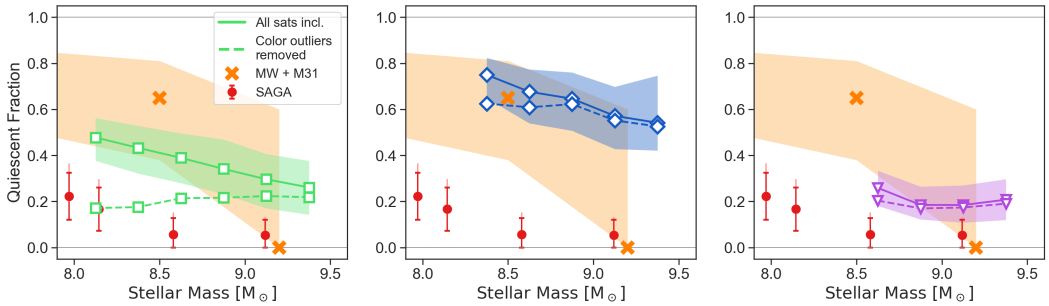

Fig. 4.4: The effect of including (solid lines) or excluding (dashed lines) the "color outlier" satellites in the quiescent fraction measured from mock SAGA surveys in each simulation, as compared to SAGA (red circles) and the Local Group (orange crosses, shading). Of the simulations, only TNG shows a change in the quiescent fraction that is greater than the errors from cosmic variation and Poisson noise.

Though the use the of the SAGA color cut ostensibly shifts the TNG quiescent fraction to be in much closer agreement with the SAGA measurements, the presence of the quiescent satellites with extremely red colors remains in tension with SAGA's blind spectroscopic searches of the region of color space excluded by the color cuts.

4.5.2 The effects of local environment

One of the major findings from SAGA has been that the satellites of the Milky Way and Andromeda are indeed unusual when compared to the broader population of satellites around similarly-massive hosts. It is possible that the interactions between the Milky Way and Andromeda systems are driving increased quenching, but it remains unclear just how extreme or unusual our local environment is relative to an average Milky Way-mass system. SAGA does not exclude Local Groups from the host selection (nearby Milky Way-mass centrals are allowed as long as they lie beyond 300 kpc in projected distance), so the 36 hosts also include Milky Way analogs in a range of environments, from Local Group-like to very isolated.

To quantify the effects of the Local Group environment in the simulations, we split up the Milky Way analogs in each simulation to select isolated Milky Ways (no nearby massive neighbor within 1 Mpc) and dense Local Groups (massive neighbor within 500 kpc) and measure the quiescent fraction of satellites that would be seen by SAGA, shown in Figure 4.5.

In all three simulations, the satellite quiescent fraction is elevated for dense Local Groups as compared to isolated Milky Ways. In all cases (with the exception of lowest mass bin for isolated Milky Ways in SIMBA), the quiescent fraction for simulated galaxies in both environments remains in agreement with observations of the Local Group, but not the SAGA measurements. Additionally, a fraction of the

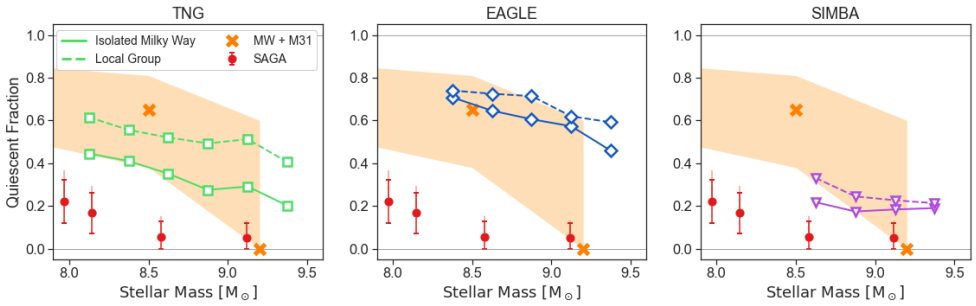

Fig. 4.5: The quiescent fraction as a function of stellar mass for satellites of Milky Way analogs, split into isolated Milky Ways (no other massive galaxy within 1 Mpc) and Local Groups (an additional massive galaxy within 500 kpc). Satellites of Local Groups are more quiescent than those around isolated Milky Ways.

satellites of isolated Milky Ways in simulations remain quiescent at $M_* \sim 10^{9.25}$, in contrast to SAGA *and* the Local Group.

4.5.3 Drivers of Milky Way satellite quenching

We consider three possible explanations for the over-quenching of Milky Way satellites and the presence of satellites lying outside the SAGA color cuts in the simulations.

1. *SAGA is missing a population of faint satellites with very red colors.* If the missing satellites have extremely low surface brightnesses, they would be more likely to missed by the photometric surveys from which the initial SAGA target catalogs were compiled. However, we note that no extremely low surface brightness satellites with $M_* > 10^{8.5}$ $M_\odot$ have been identified around the Milky Way either.

2. *The faint red satellites are simulation artifacts.* While our lower mass limits are selected to ensure each simulated galaxy has a sufficient number of stellar mass particles ($N > 100$), the finite resolution of the simulations requires that many dynamical interactions be approximated rather than derived from first principle physics. As such, the simulated satellites may be unphysically

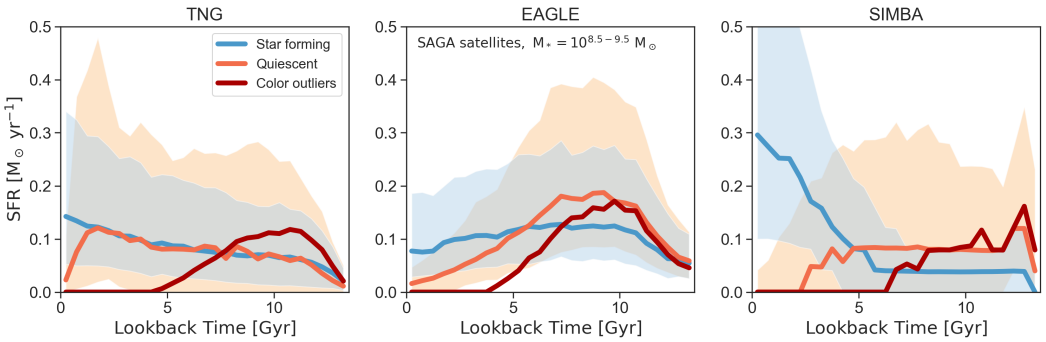

Fig. 4.6: Median star formation histories of SAGA satellites in each simulation, split into star forming (blue), quiescent (orange), and "color outliers" (red). Shaded regions are the $20^{\text{th}} - 80^{\text{th}}$ percentile of the distributions for star forming and quiescent galaxies.

resistant to disruption from interactions with their host halos, which would have destroyed any counterparts in the observed universe.

If the simulated quiescent galaxies are artificially disruption-resistant or if quiescent satellites in the real universe are more susceptible to environment effects, this could explain both the presence of the faint red satellites and the elevated quiescent fractions of the simulations.

3. *The satellite colors are unphysical.* The colors we measure from the synthetic spectra are in good agreement with other suites of spectra generated from the simulations. However, it may be that the underlying star formation histories which determine the observed satellites properties are unphysical and these galaxies should not be quiescent.

Figure 4.6 shows the star formation histories for satellite galaxies in each simulation, split into star forming, quiescent, or "color outliers". In all three simulations, the outlier satellites quench their star formation at much earlier times than quiescent galaxies with "normal" colors. It is unclear if low mass galaxies should be unable to form any stars for such prolonged periods of time, even while residing in Milky Way mass halos.

The tension between the SAGA observations and the simulations could be resolved if the satellites with outlier colors were either disrupted by their host halos, experienced some rejuvenation of star formation in the 4-6 Gyr since they initially quenched, or never quenched to begin with.

Also of note is the fact that a significant subset of the isolated quiescent galaxies we identified in Chapter 3 experienced similar early and permanent quenching. Host-halo-driven disruption should only effect satellite galaxies, while feedback processes can encompass both environmental quenching and internal quenching (e.g., stellar winds, AGN outflows). While increased satellite disruption could potentially remove the tension between the simulations and SAGA regarding both the presence of faint red satellites and the elevated quiescent fraction, less aggressive internal feedback could resolve the tensions between the simulations and SAGA as well as the isolated galaxies in SDSS.

4.6 Defining Quiescence

Thus far we have used the mock surveys created with Orchard to learn about the quenching of low mass galaxies as implemented in large-scale hydrodynamical simulations. But this type of forward modelling technique can also inform observational survey design.

In particular, the choice of quenching definition can vary widely within the field of galaxy evoltuion. This includes both the observational tracer used (e.g., $\mathrm{H}\alpha$ EW or UV SFR) and the actual definition of quiescence (e.g., $\mathrm{H}\alpha$ EW < 2 Å or $\mathrm{SFR} < 10^{-2}\ \mathrm{M}_{\odot}\,/\,\mathrm{yr}$). These choices can correspond to very different underlying star formation histories, as observables trace different timescales of star formation. Defining galaxies as quiescent when $\mathrm{H}\alpha$ EW ≤ 2 Å will select both galaxies with $\mathrm{H}\alpha$ absorption lines as well as galaxies with small amounts of $\mathrm{H}\alpha$ emission (indicative

of at least some recent star formation), while $\mathrm{H}\alpha$ EW ≤ 0 Å would only select the systems in absorption. The choice of observational threshold also ends up defining what "quiescence" is within the particular study.

However, the noise properties of the observables also inform which galaxies are selected by a particular definition of quiescence. For instance, an observationally-selected sample of galaxies where quiescence is defined as lacking $\mathrm{H}\alpha$ emission may also include galaxies with low level $\mathrm{H}\alpha$ emission that is obscured due to low signal-to-noise.

In Figure 4.7 we show the effects of noise on the distribution of galaxy observables and the resulting quiescent fraction for two seemingly similar definitions of $\mathrm{H}\alpha$ EW-based quiescence for satellite galaxies in TNG. In the upper row we show $\mathrm{H}\alpha$ EW measured from realistically noisy spectra, color-coded by the quiescent / star forming designation from the noise-free spectra. A blue-outlined point in the gray region represents a galaxy that would be classified as star forming based on its "true" spectrum but would be observed due to the finite SNR of the observations.

The bottom row of Figure 4.7 shows the quiescent fractions derived for the same galaxy sample with and without noise for the two definitions. The more generous definition of quiescence (including galaxies in absorption and those with very low EWs in emission) is effectively unchanged by the addition of noise to the observations, while the $\mathrm{H}\alpha$ EW < 0 Å definition that should select a higher-purity sample experiences significantly greater contamination than the looser definition with the addition of observational noise.

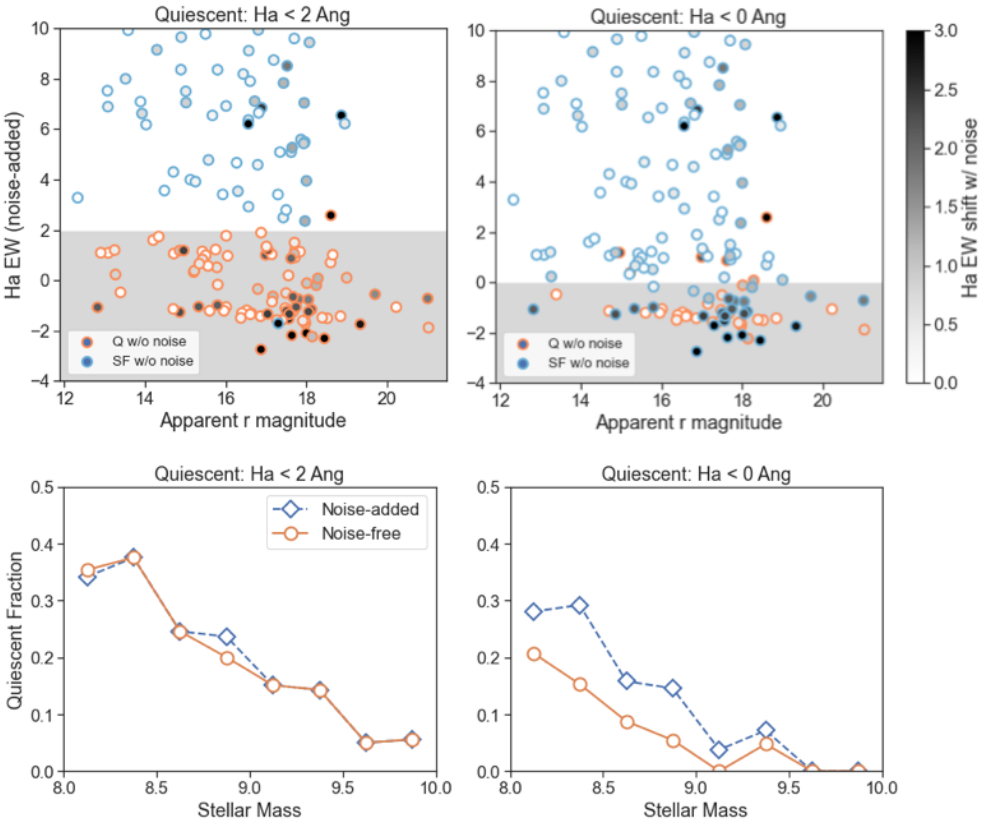

Fig. 4.7: *Top row:* Hα EW as function of apparent r magnitude for satellite galaxies in TNG, measured from the noise-added spectra. Galaxies in the gray region would be classified as quiescent based on the noise-added spectra (left column: ≤ 2 Å; right column: ≤ 0 Å), while the colored outlines delineate the classification based on the "true" spectra before the addition of realistic observational noise. The grayscale fill color corresponds to the magnitude of the shift in the measured Hα EW between the true and observed Hα EWs.
Bottom row: The quiescent fraction for satellite galaxies in TNG based on the noise-added (blue diamonds) or the noise-free (orange circles) spectra for the given definition of quiescence (left column: ≤ 2 Å; right column: ≤ 0 Å).

4.7 Conclusions

In this paper, we have produced mock SAGA-like surveys from three large volume hydrodynamic simulations (Illustris-TNG, EAGLE, and SIMBA) from which we measured the quiescent fraction of satellites of Milky Way-like galaxies and compared back to extant constraints from the local universe (Mao et al., 2020). We find that:

1. The three simulations examined in this work, when transformed into observational space using an identical methodology, show increasing satellite quiescent fractions towards lower stellar masses, in qualitative agreement with observations.

2. All three simulations have quiescent fractions in agreement with observations of the Local Group satellite population (within errors on the Local Group), but in disagreement with observations from the SAGA survey, which finds significantly lower numbers of quiescent satellites around Milky Way-like host galaxies.

3. A subset of satellite galaxies in the simulations fall outside of the color-cut used to select satellites in SAGA. These "color outliers" are not observed in SAGA's blind follow-up searches. This suggests that either SAGA has been extremely unlucky to have missed these galaxies, or that the simulations should not be producing satellites with such red colors. An increase in the efficacy of satellite disruption by the host halos or a decrease in the efficacy of low mass galaxy quenching could resolve this tension.

4. Noise properties of the observations from which properties like quiescence are determined can significantly effect the purity of the selection criterion. We show that when selecting quiescent galaxies based on $\mathrm{H}\alpha$ EW, a seemingly more relaxed criterion of $\mathrm{EW} < 2$ Å is extremely robust to contamination while a more strict criterion suffers from significantly reduced purity.

List of Figures

List of Tables

Bibliography

Abazajian, K., Adelman-McCarthy, J. K., Agüeros, M. A., et al. 2003, AJ, 126, 2081

Agostino, C. J., & Salim, S. 2019, ApJ, 876, 12

Aihara, H., Allende Prieto, C., An, D., et al. 2011, ApJS, 193, 29

Anglés-Alcázar, D., Davé, R., Faucher-Giguère, C.-A., Özel, F., & Hopkins, P. F. 2017a, MNRAS, 464, 2840

Anglés-Alcázar, D., Faucher-Giguère, C.-A., Kereš, D., et al. 2017b, MNRAS, 470, 4698

Anglés-Alcázar, D., Özel, F., & Davé, R. 2013, ApJ, 770, 5

Anglés-Alcázar, D., Özel, F., Davé, R., et al. 2015, ApJ, 800, 127

Appleby, S., Davé, R., Kraljic, K., Anglés-Alcázar, D., & Narayanan, D. 2019, arXiv e-prints, arXiv:1911.02041

Baes, M., Verstappen, J., De Looze, I., et al. 2011, ApJS, 196, 22

Baldassare, V. F., Geha, M., & Greene, J. 2018, ArXiv e-prints, arXiv:1808.09578

Baldassare, V. F., Reines, A. E., Gallo, E., & Greene, J. E. 2015, ApJ, 809, L14

Baldassare, V. F., Reines, A. E., Gallo, E., et al. 2016, ApJ, 829, 57

Baldry, I. K., Balogh, M. L., Bower, R. G., et al. 2006, MNRAS, 373, 469

Baldwin, J. A., Phillips, M. M., & Terlevich, R. 1981, Publications of the Astronomical Society of the Pacific, 93, 5

Balogh, M. L., Morris, S. L., Yee, H. K. C., Carlberg, R. G., & Ellingson, E. 1999, ApJ, 527, 54

Barth, A. J., Greene, J. E., & Ho, L. C. 2008, AJ, 136, 1179

Barth, A. J., Ho, L. C., Rutledge, R. E., & Sargent, W. L. W. 2004, ApJ, 607, 90

Bauer, A. E., Hopkins, A. M., Gunawardhana, M., et al. 2013, MNRAS, 434, 209

Belfiore, F., Maiolino, R., Tremonti, C., et al. 2017, MNRAS, 469, 151

Bell, E. F., & de Jong, R. S. 2001, ApJ, 550, 212

Bell, E. F., McIntosh, D. H., Katz, N., & Weinberg, M. D. 2003, ApJS, 149, 289

Blanton, M. R., Kazin, E., Muna, D., Weaver, B. A., & Price-Whelan, A. 2011, AJ, 142, 31

Blanton, M. R., & Moustakas, J. 2009, ARAA, 47, 159

Blanton, M. R., & Roweis, S. 2007, AJ, 133, 734

Blanton, M. R., Hogg, D. W., Bahcall, N. A., et al. 2003, ApJ, 594, 186

Borrow, J., Anglés-Alcázar, D., & Davé, R. 2020, MNRAS, 491, 6102

Bower, R. G., Benson, A. J., Malbon, R., et al. 2006, MNRAS, 370, 645

Bower, R. G., Schaye, J., Frenk, C. S., et al. 2017, MNRAS, 465, 32

Bradford, J. D., Geha, M. C., Greene, J. E., Reines, A. E., & Dickey, C. M. 2018, ApJ, 861, 50

Brammer, G. B., Whitaker, K. E., van Dokkum, P. G., et al. 2009, ApJL, 706, L173

Brinchmann, J., Charlot, S., White, S. D. M., et al. 2004, MNRAS, 351, 1151

Byler, N., Dalcanton, J. J., Conroy, C., & Johnson, B. D. 2017, ApJ, 840, 44

Camps, P., Trčka, A., Trayford, J., et al. 2018, ApJS, 234, 20

Cann, J. M., Satyapal, S., Abel, N. P., et al. 2019, ApJ, 870, L2

Cappellari, M. 2017, MNRAS, 466, 798

Chabrier, G. 2003, PASP, 115, 763

Charlot, S., & Fall, S. M. 2000, ApJ, 539, 718

Chen, Z., Faber, S. M., Koo, D. C., et al. 2020, ApJ, 897, 102

Choi, E., Ostriker, J. P., Naab, T., & Johansson, P. H. 2012, ApJ, 754, 125

Choi, E., Ostriker, J. P., Naab, T., Oser, L., & Moster, B. P. 2015, MNRAS, 449, 4105

Christiansen, J. F., Davé, R., Sorini, D., & Anglés-Alcázar, D. 2019, arXiv e-prints, arXiv:1911.01343

Colless, M., Dalton, G., Maddox, S., et al. 2001, MNRAS, 328, 1039

Conroy, C., & Gunn, J. E. 2010, ApJ, 712, 833

Conroy, C., Gunn, J. E., & White, M. 2009, ApJ, 699, 486

Crain, R. A., Schaye, J., Bower, R. G., et al. 2015, MNRAS, 450, 1937

Crook, A. C., Huchra, J. P., Martimbeau, N., et al. 2007, ApJ, 655, 790

Croton, D. J., Springel, V., White, S. D. M., et al. 2006, MNRAS, 365, 11

Daddi, E., Dickinson, M., Morrison, G., et al. 2007, ApJ, 670, 156

Dalla Vecchia, C., & Schaye, J. 2012, MNRAS, 426, 140

Dashyan, G., Silk, J., Mamon, G. A., Dubois, Y., & Hartwig, T. 2018, MNRAS, 473, 5698

Davé, R., Anglés-Alcázar, D., Narayanan, D., et al. 2019, MNRAS, 486, 2827

Davé, R., Rafieferantsoa, M. H., Thompson, R. J., & Hopkins, P. F. 2017, MNRAS, 467, 115

Davé, R., Thompson, R., & Hopkins, P. F. 2016, MNRAS, 462, 3265

Davies, J. J., Crain, R. A., Oppenheimer, B. D., & Schaye, J. 2020, MNRAS, 491, 4462

Davis, M., Efstathiou, G., Frenk, C. S., & White, S. D. M. 1985, ApJ, 292, 371

Dekel, A., & Silk, J. 1986, ApJ, 303, 39

DESI Collaboration, Aghamousa, A., Aguilar, J., et al. 2016, arXiv e-prints, arXiv:1611.00036

Dickey, C. M., Geha, M., Wetzel, A., & El-Badry, K. 2019, ApJ, 884, 180

Diemer, B. 2020, arXiv e-prints, arXiv:2007.10992

Donnari, M., Pillepich, A., Nelson, D., et al. 2020a, arXiv e-prints, arXiv:2008.00004

—. 2019, MNRAS, 485, 4817

Donnari, M., Pillepich, A., Joshi, G. D., et al. 2020b, arXiv e-prints, arXiv:2008.00005

El-Badry, K., Wetzel, A., Geha, M., et al. 2016, ApJ, 820, 131

Elbaz, D., Daddi, E., Le Borgne, D., et al. 2007, A&A, 468, 33

Filippenko, A. V., & Ho, L. C. 2003, ApJ, 588, L13

Fillingham, S. P., Cooper, M. C., Boylan-Kolchin, M., et al. 2018, MNRAS, 477, 4491

Flores Velázquez, J. A., Gurvich, A. B., Faucher-Giguère, C.-A., et al. 2020, arXiv e-prints, arXiv:2008.08582

Foreman-Mackey, D., Sick, J., & Johnson, B. 2014, Python-Fsps: Python Bindings to FSPS (v0.1.1), Zenodo

Furlong, M., Bower, R. G., Theuns, T., et al. 2015, MNRAS, 450, 4486

Gabor, J. M., Davé, R., Oppenheimer, B. D., & Finlator, K. 2011, MNRAS, 417, 2676

Geha, M., Blanton, M. R., Yan, R., & Tinker, J. L. 2012, ApJ, 757, 85

Genel, S., Vogelsberger, M., Springel, V., et al. 2014, MNRAS, 445, 175

Genel, S., Nelson, D., Pillepich, A., et al. 2018, MNRAS, 474, 3976

Giovanelli, R., Haynes, M. P., Kent, B. R., et al. 2005, AJ, 130, 2598

Graus, A. S., Bullock, J. S., Fitts, A., et al. 2019, arXiv e-prints, arXiv:1901.05487

Greene, J. E., & Ho, L. C. 2007, ApJ, 670, 92

Groves, B. A., Heckman, T. M., & Kauffmann, G. 2006, MNRAS, 371, 1559

Habouzit, M., Genel, S., Somerville, R. S., et al. 2019, MNRAS, 484, 4413

Habouzit, M., Li, Y., Somerville, R. S., et al. 2020, arXiv e-prints, arXiv:2006.10094

Hahn, C., Starkenburg, T. K., Choi, E., et al. 2019, ApJ, 872, 160

Hamilton, D. 1985, ApJ, 297, 371

Hopkins, P. F. 2015, MNRAS, 450, 53

—. 2017, arXiv e-prints, arXiv:1712.01294

Hopkins, P. F., Kereš, D., Oñorbe, J., et al. 2014, MNRAS, 445, 581

Hopkins, P. F., & Quataert, E. 2011, MNRAS, 415, 1027

Hopkins, P. F., Wetzel, A., Kereš, D., et al. 2018, MNRAS, 480, 800

Hubble, E. P. 1925, Popular Astronomy, 33, 252

—. 1926, ApJ, 64, 321

Ivezić, Ž., Kahn, S. M., Tyson, J. A., et al. 2019, ApJ, 873, 111

Iyer, K. G., Tacchella, S., Genel, S., et al. 2020, MNRAS, 498, 430

Jones, D. H., Saunders, W., Colless, M., et al. 2004, MNRAS, 355, 747

Jönsson, H., Holtzman, J. A., Allende Prieto, C., et al. 2020, AJ, 160, 120

Katsianis, A., Gonzalez, V., Barrientos, D., et al. 2020, MNRAS, 492, 5592

Kauffmann, G., White, S. D. M., Heckman, T. M., et al. 2004, MNRAS, 353, 713

Kauffmann, G., Heckman, T. M., White, S. D. M., et al. 2003a, MNRAS, 341, 33

—. 2003b, MNRAS, 341, 54

Kennicutt, R. C., & Evans, N. J. 2012, ARAA, 50, 531

Kewley, L. J., Dopita, M. A., Sutherland, R. S., Heisler, C. A., & Trevena, J. 2001, ApJ, 556, 121

Kewley, L. J., Groves, B., Kauffmann, G., & Heckman, T. 2006, MNRAS, 372, 961

Kewley, L. J., Maier, C., Yabe, K., et al. 2013, ApJ, 774, L10

Kormendy, J., & Kennicutt, Robert C., J. 2004, Annual Review of Astronomy and Astrophysics, 42, 603

Koudmani, S., Sijacki, D., Bourne, M. A., & Smith, M. C. 2019, MNRAS, 484, 2047

Kroupa, P. 2001, MNRAS, 322, 231

Leja, J., Johnson, B. D., Conroy, C., et al. 2019, ApJ, 877, 140

Li, Y., Habouzit, M., Genel, S., et al. 2019, arXiv e-prints, arXiv:1910.00017

Mao, Y.-Y., Geha, M., Wechsler, R. H., et al. 2020, arXiv e-prints, arXiv:2008.12783

Marinacci, F., Vogelsberger, M., Pakmor, R., et al. 2018, MNRAS, 480, 5113

Martin, D. C., Fanson, J., Schiminovich, D., et al. 2005, ApJL, 619, L1

Martín-Navarro, I., & Mezcua, M. 2018, ApJ, 855, L20

McAlpine, S., Bower, R. G., Harrison, C. M., et al. 2017, MNRAS, 468, 3395

McAlpine, S., Bower, R. G., Rosario, D. J., et al. 2018, MNRAS, 481, 3118

McAlpine, S., Helly, J. C., Schaller, M., et al. 2016, Astronomy and Computing, 15, 72

McK Mahille, J., Schild, R., Wendorf, F., & Brenmer, R. 2007, African Skies, 11, 2

McKinnon, R., Torrey, P., Vogelsberger, M., Hayward, C. C., & Marinacci, F. 2017, MNRAS, 468, 1505

Moustakas, J., Kennicutt, Robert C., J., & Tremonti, C. A. 2006, ApJ, 642, 775

Moustakas, J., Coil, A. L., Aird, J., et al. 2013, ApJ, 767, 50

Munshi, F., Governato, F., Brooks, A. M., et al. 2013, ApJ, 766, 56

Muratov, A. L., Kereš, D., Faucher-Giguère, C.-A., et al. 2015, MNRAS, 454, 2691

Muzzin, A., Marchesini, D., Stefanon, M., et al. 2013, ApJ, 777, 18

Naab, T., & Ostriker, J. P. 2017, ARAA, 55, 59

Naiman, J. P., Pillepich, A., Springel, V., et al. 2018, MNRAS, 477, 1206

Nelson, D., Pillepich, A., Springel, V., et al. 2018, MNRAS, 475, 624

Noeske, K. G., Weiner, B. J., Faber, S. M., et al. 2007, ApJL, 660, L43

Papovich, C., Kawinwanichakij, L., Quadri, R. F., et al. 2018, ApJ, 854, 30

Pasquali, A., Gallazzi, A., Fontanot, F., et al. 2010, MNRAS, 407, 937

Peng, Y.-j., Lilly, S. J., Kovač, K., et al. 2010, ApJ, 721, 193

Penny, S. J., Masters, K. L., Smethurst, R., et al. 2018, MNRAS, 476, 979

Pillepich, A., Nelson, D., Hernquist, L., et al. 2018a, MNRAS, 475, 648

Pillepich, A., Springel, V., Nelson, D., et al. 2018b, MNRAS, 473, 4077

Prochaska, J. X., Gawiser, E., Wolfe, A. M., Cooke, J., & Gelino, D. 2003, The Astrophysical Journal Supplement Series, 147, 227

Reines, A. E., Greene, J. E., & Geha, M. 2013, ApJ, 775, 116

Rey, M. P., Pontzen, A., Agertz, O., et al. 2020, MNRAS, 497, 1508

Rodríguez Montero, F., Davé, R., Wild, V., Anglés-Alcázar, D., & Narayanan, D. 2019, MNRAS, 490, 2139

Sales, L. V., Vogelsberger, M., Genel, S., et al. 2015, MNRAS, 447, L6

Salim, S., Boquien, M., & Lee, J. C. 2018, ApJ, 859, 11

Salim, S., Rich, R. M., Charlot, S., et al. 2007, ApJS, 173, 267

Salim, S., Lee, J. C., Janowiecki, S., et al. 2016, ApJS, 227, 2

Sartori, L. F., Schawinski, K., Treister, E., et al. 2015, MNRAS, 454, 3722

Satyapal, S., Vega, D., Heckman, T., O'Halloran, B., & Dudik, R. 2007, ApJ, 663, L9

Schaller, M., Dalla Vecchia, C., Schaye, J., et al. 2015, MNRAS, 454, 2277

Schaye, J., Crain, R. A., Bower, R. G., et al. 2015, MNRAS, 446, 521

Sheinis, A. I., Bolte, M., Epps, H. W., et al. 2002, PASP, 114, 851

Skillman, E. D., Monelli, M., Weisz, D. R., et al. 2017, ApJ, 837, 102

Skrutskie, M. F., Cutri, R. M., Stiening, R., et al. 2006, AJ, 131, 1163

Smith, R. J., Lucey, J. R., Price, J., Hudson, M. J., & Phillipps, S. 2012, MNRAS, 419, 3167

Somerville, R. S., & Davé, R. 2015, Annual Review of Astronomy and Astrophysics, 53, 51

Somerville, R. S., Hopkins, P. F., Cox, T. J., Robertson, B. E., & Hernquist, L. 2008, MNRAS, 391, 481

Sparre, M., Hayward, C. C., Springel, V., et al. 2015, MNRAS, 447, 3548

Speagle, J. S., Steinhardt, C. L., Capak, P. L., & Silverman, J. D. 2014, ApJS, 214, 15

Springel, V. 2005, MNRAS, 364, 1105

—. 2010, ARAA, 48, 391

Springel, V., White, S. D. M., Tormen, G., & Kauffmann, G. 2001a, MNRAS, 328, 726

Springel, V., Yoshida, N., & White, S. D. M. 2001b, Nature Astronomy, 6, 79

Springel, V., Pakmor, R., Pillepich, A., et al. 2018, MNRAS, 475, 676

Su, K.-Y., Hopkins, P. F., Hayward, C. C., et al. 2018, arXiv e-prints, arXiv:1809.09120

Terrazas, B. A., Bell, E. F., Henriques, B. M. B., et al. 2016, ApJL, 830, L12

Terrazas, B. A., Bell, E. F., Pillepich, A., et al. 2020, MNRAS, 493, 1888

Thomas, N., Davé, R., Anglés-Alcázar, D., & Jarvis, M. 2019, MNRAS, 487, 5764

Tinker, J., Wetzel, A., & Conroy, C. 2011, arXiv e-prints, arXiv:1107.5046

Torrey, P., Vogelsberger, M., Genel, S., et al. 2014, MNRAS, 438, 1985

Trayford, J. W., Theuns, T., Bower, R. G., et al. 2015, MNRAS, 452, 2879

Trayford, J. W., Camps, P., Theuns, T., et al. 2017, MNRAS, 470, 771

Trump, J. R., Sun, M., Zeimann, G. R., et al. 2015, ApJ, 811, 26

Trčka, A., Baes, M., Camps, P., et al. 2020, MNRAS, 494, 2823

van de Weygaert, R., & Platen, E. 2011, in International Journal of Modern Physics Conference Series, Vol. 1, 41

van Dokkum, P. G. 2001, Publications of the Astronomical Society of the Pacific, 113, 1420

Veilleux, S., & Osterbrock, D. E. 1987, The Astrophysical Journal Supplement Series, 63, 295

Villaume, A., Conroy, C., & Johnson, B. D. 2015, ApJ, 806, 82

Vogelsberger, M., Marinacci, F., Torrey, P., & Puchwein, E. 2020, Nature Reviews Physics, 2, 42

Vogelsberger, M., Genel, S., Springel, V., et al. 2014, MNRAS, 444, 1518

Weinberger, R., Ehlert, K., Pfrommer, C., Pakmor, R., & Springel, V. 2017, MNRAS, 470, 4530

Weinberger, R., Springel, V., Pakmor, R., et al. 2018, MNRAS, 479, 4056

Weisz, D. R., Dolphin, A. E., Skillman, E. D., et al. 2015, ApJ, 804, 136

Wetzel, A. R., Tinker, J. L., & Conroy, C. 2012, MNRAS, 424, 232

Wetzel, A. R., Tinker, J. L., Conroy, C., & van den Bosch, F. C. 2013, MNRAS, 432, 336

Wetzel, A. R., Tollerud, E. J., & Weisz, D. R. 2015, ApJL, 808, L27

Wheeler, C., Oñorbe, J., Bullock, J. S., et al. 2015, MNRAS, 453, 1305

Wheeler, C., Hopkins, P. F., Pace, A. B., et al. 2019, MNRAS, 490, 4447

White, S. D. M., & Frenk, C. S. 1991, ApJ, 379, 52

White, S. D. M., & Rees, M. J. 1978, MNRAS, 183, 341

Wright, A. C., Brooks, A. M., Weisz, D. R., & Christensen, C. R. 2019, MNRAS, 482, 1176

Yan, R. 2011, AJ, 142, 153

—. 2018, MNRAS, 481, 476

Yan, R., & Blanton, M. R. 2012, ApJ, 747, 61

Yan, R., Newman, J. A., Faber, S. M., et al. 2006, ApJ, 648, 281

York, D. G., Adelman, J., Anderson, John E., J., et al. 2000, AJ, 120, 1579